High-Resolution Electron Energy-Loss Spectroscopy of Beam-Sensitive Functional Materials

Dissertation

Presented in Partial Fulfillment of the Requirements for the Degree Doctor of Philosophy in the Graduate School of The Ohio State University

By

Jessica Anne Alexander

Graduate Program in Materials Science and Engineering

The Ohio State University

2018

Dissertation Committee

Dr. David W. McComb, Advisor

Dr. Tyler J. Grassman

Dr. Vicky Doan-Nguyen

Dr. Wendy Panero

Abstract

By making electron energy-loss spectroscopy (EELS) measurements in a scanning transmission electron microscope (STEM), the optoelectronic properties of a material can be determined with nanometer spatial resolution. Since these optoelectronic properties can be related to the electronic structure of a material, STEM-EELS can also probe the local bonding environment at the interface of two materials. Such measurements could be key in developing more efficient P3HT:PCBM bulk-heterojunction organic photovoltaics (P3HT = poly(3-hexylthiophene), PCBM = [6,6] phenyl C_{61} butyric acid methyl ester), as understanding the local electronic structure/local bonding environment at P3HT/PCBM interfaces should provide insight into charge generation/transport. However, organic materials, such as P3HT and PCBM, are extremely susceptible to beam-damage when placed under a high energy electron beam. Thus, it is difficult to use STEM-EELS to collect reliable data for these beam-sensitive materials without the electron beam causing changes to the local chemistry.

For the first time, it was demonstrated that, via a beam damage-minimization EELS acquisition method, reliable high-resolution low-loss STEM-EELS data could be collected for electron beam-sensitive materials. Using this method, low-loss EELS spectra were acquired (using an FEI Titan^3 60-300 Image-Corrected S/TEM) for thin films of four materials used in organic photovoltaics – P3HT, PCBM, CuPc (copper

phthalocyanine), and C_{60} (fullerene). From these low-loss spectra, the real (ε_1) and imaginary (ε_2) parts of the complex dielectric function were extracted. These ε_1 and ε_2 spectra were then compared to similar spectra obtained via a technique that should not damage these organic materials (variable-angle spectroscopic ellipsometry, VASE). As the STEM-EELS and VASE ε_1 and ε_2 spectra agreed well in both the number of peaks observed and their corresponding peak energies, the beam damage-minimization EELS acquisition method was proven to be suitable for collecting reliable low-loss EELS spectra of P3HT, PCBM, CuPc, and C_{60}.

This beam damage-minimization EELS acquisition method was then used to collect low-loss EELS spectra for P3HT, PCBM, CuPc, and C_{60} using a Nion UltraSTEM 100 MC 'HERMES' S/TEM. With this scanning transmission electron microscope, it was possible to collect low-loss spectra with higher energy resolutions (35 meV) than what was achievable using the FEI Titan^3 60-300 Image-Corrected S/TEM (175 meV). The ε_1 and ε_2 spectra obtained from measurements on these two instruments were compared, and it was determined that the improved energy resolution of the Nion UltraSTEM did not result in the acquisition of any new optoelectronic information for these four materials.

By utilizing the beam damage-minimization EELS acquisition method to collect EELS spectrum images, spatially-resolved high-resolution low-loss EELS spectra were collected across the interface of a CuPc/C_{60} bilayer structure. These measurements demonstrated that reliable and spatially-resolved EELS data could be collected for beam-sensitive materials. These methods were then used to conduct preliminary STEM-EELS measurements of an actual P3HT:PCBM bulk-heterojunction organic photovoltaic,

proving that, until the thickness of these samples can approach the size of the individual domains within the blended P3HT:PCBM layer, it will be difficult to acquire EELS data at the P3HT/PCBM interface.

Another organic-based material, vanadium tetracyanoethylene ($V[TCNE]_{x\sim2}$), was studied using the beam damage-minimization EELS acquisition methods developed. This organic-based ferrimagnetic semiconductor exhibits desirable magnetic properties, but, because of its air-sensitivity, the optoelectronic properties have not yet been determined. By using a sample preparation method in which the sample was minimally exposed to air, it was demonstrated, for the first time, how STEM-EELS can be used to obtain the complex dielectric function, from which many other optoelectronic properties can be extracted. Furthermore, via core-loss EELS measurements, the oxidation state of vanadium was confirmed to be $\sim V^{2+}$ and was shown, for the first time, to be homogenous throughout the $V[TCNE]_{x\sim2}$ sample.

Lastly, low-loss STEM-EELS was used to obtain spectra of ε_1, ε_2, and the absorption coefficient for two lead-free double halide perovskites – $Cs_2AgBiBr_6$ and $Cs_2AgBiCl_6$. The extracted ε_2 spectra were compared to density functional theory calculations, and the absorption coefficient spectra were compared to correlative VASE measurements, the comparisons of which suggest that higher (energy) resolution STEM-EELS measurements are required to ensure that all of the optoelectronic properties of these two materials are extracted.

Dedication

To my mom,

And in loving memory of PJ

Acknowledgments

First and foremost, I would like to acknowledge and give thanks to my mom. Without your support and constant encouragement, I know that there is no way that I would be where I am today. I am so grateful to you. I would also like to thank the rest of my family for always being there for me. Words cannot express how much it means to me to know that I have you all on my side.

There are also several people at The Ohio State University's (OSU's) Center for Electron Microscopy and Analysis (CEMAS) who have helped to make my doctoral degree a reality. To my advisor, Dr. David McComb, I thank you for your support and guidance in helping me pursue my doctorate and in completing this research project. I have learned so much, and I know that the experience in working under your direction has made me a better researcher. I am also thankful to both Frank Scheltens and Robert Williams for all of the help that the two of you gave me in developing the skills and techniques necessary for collecting the data that is presented in this document. Last, but certainly not least, I would like to thank my fellow group members – Julia Deitz, Felix Liu, and Amanda Trout – for your friendship and for ensuring that I had fun while pursuing this dream.

Lastly, I would like to thankfully acknowledge my funding sources: (1) The Ohio State University through their Distinguished University Fellowship and (2) the Air Force

Research Laboratory's Materials and Manufacturing Directorate through the AFRL/DAGSI Ohio Student-Faculty Research Fellowship.

Vita

2009 ……. Fairhope High School

2013 …… B.S. Physics, University of South Alabama

2016 ……...… M.S. Materials Science & Engineering, The Ohio State University

2018 ……..... Ph.D. Materials Science & Engineering, The Ohio State University

Publications

Alexander JA, Scheltens FJ, Drummy LF, Durstock MF, Gilchrist JB, Heutz S, et al. Measurement of optical properties in organic photovoltaic materials using monochromated electron energy-loss spectroscopy. J Mater Chem A. 2016;4:13636–45.

Alexander JA, Scheltens FJ, Drummy LF, Durstock MF, Hage FS, Ramasse QM, et al. High-resolution monochromated electron energy-loss spectroscopy of organic photovoltaic materials. Ultramicroscopy. 2017;180:125–32.

Fields of Study

Major Field: Materials Science and Engineering

Table of Contents

List of Tables

List of Figures

Chapter 1. Introduction and Background

In this chapter, the necessary background will be given for the materials systems studied and discussed in Chapters 3 - 6.

1.1. Organic Photovoltaics (OPVs)

Organic photovoltaics (OPVs), first successfully demonstrated in 1986 [1], show promise as an alternative solar technology for clean, renewable energy. The term OPV refers, in general, to photovoltaics in which the photoactive layer of the device is composed of some combination of polymer and/or small molecule materials. The ability to replace traditional inorganic materials, such as silicon, with organic materials makes it possible to (1) tune the electronic properties by slightly changing the polymer/molecular structure, (2) manufacture the solar cells using solution-processing techniques at room temperature, which is fairly easy and inexpensive, and (3) prepare lightweight solar cells on flexible substrates, and it is due to these unique properties that OPVs have garnered much interest in the solar community.

1.1.1. Physical Principles and Limitations of Organic Photovoltaics

When a solar cell is under the sun's illumination, photons from the sun can be absorbed by the solar cell and a charge can be generated [2]. When a photon is absorbed in an OPV, an excited electron-hole pair (known as an exciton) will be generated in the photoactive layer of the device [4,5]. The electron and hole of the exciton are bound to each other and must be separated in order to contribute to the photocurrent as free charge carriers [3,5,6]. This process is known as exciton dissociation and will occur at the interface between the donor (typically a polymer) and the acceptor (typically a fullerene-derivative) materials of the photoactive layer [4,5,7]. Essentially, an exciton within the donor material (but near the donor/acceptor interface) will dissociate because the electron of the electron-hole pairing will be attracted to the acceptor material due to the high electron affinity of fullerenes, especially as compared to other polymers and small molecules [4,7]. Thus, once the excitons reach the donor/acceptor interface and dissociate, the electron and hole are free charge carriers that can then travel through the corresponding domain (donor domain for holes, acceptor domain for electrons) in order to reach the appropriate electrode and generate the photocurrent [7].

In early OPV devices, the bilayer architecture was utilized, in which there was one continuous interface between the two organic semiconductor materials at which the excitons could dissociate (Figure 1.1a) [7]. However, the fact that both exciton lifetimes [8] and exciton diffusion lengths are short (on the order of ~10 nm [4–9]), the number of excitons that are able to reach the solitary donor/acceptor interface of the bilayer architecture prior to decaying is low, resulting in OPVs with low efficiencies [6,8,9]. This

is due in part because the donor and acceptor films must be thicker than 10 nm in order to absorb the incident photons from the sun, which is much longer than the diffusion length of the excitons [4–6]. This means that unless excitons are generated within 10 nm of the donor/acceptor interface, they will decay before they can reach the interface, and the electrons and holes comprising the excitons are lost as free charge carriers. Thus, in order to increase the probability that an exciton would be able to reach a donor/acceptor interface, a new device architecture was developed in 1995, as reported by references [10] and [11]. In this device architecture, known as the bulk-heterojunction (BHJ), instead of keeping the donor and materials separated with just one interface between, the donor and acceptor materials are instead blended together such that nanoscale domains of the donor and acceptor materials are formed (Figure 1.1b) [4,6–9,12]. By blending the donor and acceptor together in an interpenetrating network of domains, the ease with which an exciton can diffuse to a donor/acceptor interface increases since there are now many, many more donor/acceptor interfaces in close proximity to the excitons [4,6]. Thus, the number of free charge carriers increases, and, as expected, the overall device efficiency increases [8].

Although the BHJ architecture has helped improve the power conversion efficiency (PCE) of OPVs, the efficiencies of these devices are still too low to compete with inorganic solar cells. Currently (at the writing of this dissertation), the record efficiency for an OPV (as reported by the National Renewable Energy Laboratory in the USA) is 11.5% [13], which is much improved from the initial device efficiencies of 0.95% [1]. However, single crystal silicon (non-concentrated) photovoltaics have a record efficiency

of 25.8%, and multi-junction (four-junction, non-concentrated) inorganic photovoltaics have a record efficiency of 38.8% [13]. Thus, before OPVs are integrated into real-world applications, it is necessary to improve the device performance/efficiency.

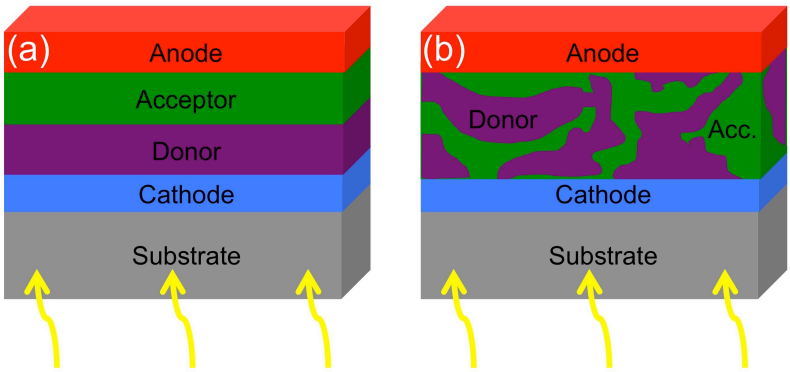

Figure 1.1: Schematics of (a) the bilayer OPV device architecture and (b) the bulk-heterojunction OPV device architecture.

1.1.2. P3HT:PCBM Organic Photovoltaics

Although many polymer/fullerene-derivative pairings have been studied for use in the photoactive layer of OPVs, one of the most popular and widely studied pairings is that of poly(3-hexylthiophene) (P3HT), a polymer, and [6,6]-phenyl-C_{61}-butyric acid methyl ester (PCBM), a fullerene-derivative (see Figure 1.2 for schematics). This is due, in part, to the many favorable properties of P3HT and PCBM. As mentioned previously, PCBM is a fullerene-derivative and therefore has a rather large electron affinity which makes exciton dissociation at the donor/acceptor interface possible [4]. It also exhibits good

solubility in organic solvents, which is important for solution processing [14]. P3HT, on the other hand, has a relatively high hole mobility, which helps the charge carrier reach its electrode, thus increasing photocurrent [14–16]. Additionally, P3HT is relatively inexpensive [17], is environmentally stable [16,17], and has an absorption edge correlating to the maximum of the solar flux [15]. On average, P3HT:PCBM bulk-heterojunction solar cells have an efficiency of ~3.5% [18].

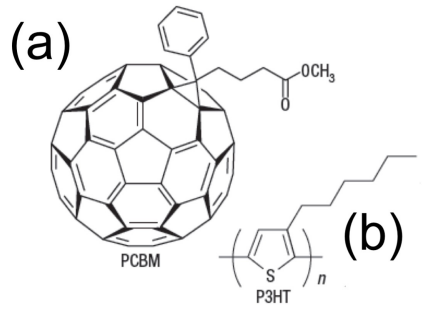

Figure 1.2: Diagrams of (a) [6,6]-phenyl-C_{61}-butyric acid methyl ester, PCBM, and (b) poly(3-hexylthiophene), P3HT. This figure was originally published in reference [19].

Figure 1.3 shows a schematic of an archetypal OPV device in which a P3HT:PCBM blend makes up the BHJ. In this device, sunlight enters through a transparent substrate (such as glass) that is coated with a transparent conducting oxide film (for example, indium tin oxide, or ITO), which serves as an electrode [4,7]. By using a transparent conducting oxide, none of the photons incident on the device from the sun are blocked before reaching the photoactive layer of the device. In P3HT:PCBM OPVs, a layer of

poly(3,4-ethylenedioxythiophene):poly(styrene sulfonate) (PEDOT:PSS) is spin-coated on the ITO to help in the collection of holes at the ITO electrode by increasing its work function [7]. Next, the P3HT:PCBM bulk-heterojunction layer is spin-coated onto the PEDOT:PSS, and finally a metal electrode (like aluminum) is then evaporated onto the bulk-heterojunction layer to complete the circuit of the device [7].

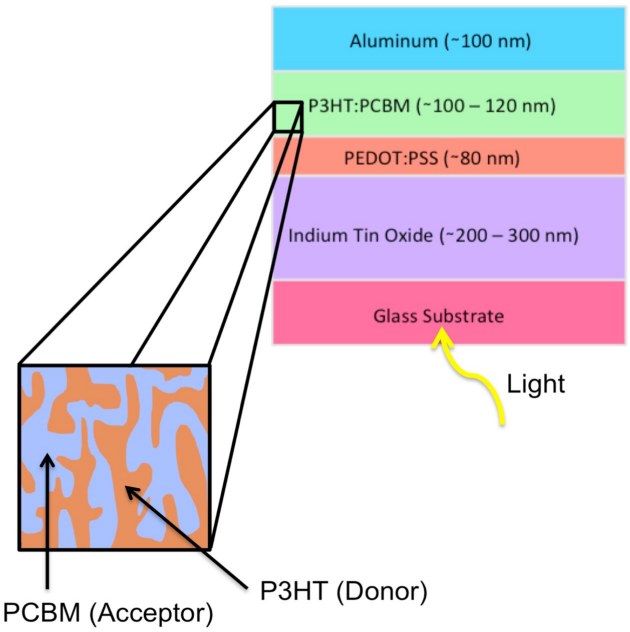

Figure 1.3: Schematic of a typical organic photovoltaic in which the photoactive layer is a bulk-heterojunction blend of P3HT and PCBM.

For P3HT:PCBM bulk-heterojunction organic photovoltaics, it has been shown that the device performance can be improved by using highly regioregular P3HT [14,17,20],

using P3HT with a high molecular weight [21], or by thermally annealing the bulk-heterojunction [16,22]. However, in order to understand why it is that researchers observe these correlations between device preparation and device performance, it is vital that the both the morphology and the local electronic structure throughout the bulk-heterojunction layer, including at the donor/acceptor interface, are understood [23–25], as changes in the morphology or electronic structure at this interface could affect charge generation and charge transport, and, therefore, the device efficiency.

1.1.2.1. Characterizing the Morphology of P3HT:PCBM BHJs

Most of the characterization studies performed on P3HT:PCBM bulk-heterojunctions (BHJs) have focused on correlating the morphology of the BHJ to both the processing and performance of P3HT:PCBM BHJ OPVs. Furthermore, because of the high spatial resolution available in transmission electron microscopes (TEMs) and scanning transmission electron microscopes (STEMs), many of the morphological studies discussed in the literature have utilized these two techniques. For instance, high-resolution transmission electron microscopy (HRTEM) was used to show how thermal annealing can cause the PCBM domains in a P3HT:PCBM BHJ to segregate to the metal electrode [26]. This could then affect the device performance since it may be more difficult for electrons generated closer to the PEDOT:PSS layer of the to find a path to the metal electrode through PCBM domains if the PCBM domains are not dispersed throughout the entire BHJ layer. Similarly, diffraction and bright-field TEM images

proved that thermal annealing increases the crystallinity of P3HT fibrils within a P3HT:PCBM BHJ [14], which improves hole transport through the P3HT fibrils since increased crystallinity corresponds to increased π-π stacking between the P3HT molecules [14,17,22,27,28]. Energy-filtered transmission electron microscopy (EFTEM) has also been utilized to study the differences in the sizes and dispersion of the P3HT domains in a P3HT:PCBM BHJ for as-cast and thermally annealed layers [29]. Since this study showed that thermal annealing increased the sizes and decreased the segregation of the P3HT domains [29], which should enhance hole transport and device efficiency. Also by using EFTEM, the sizes of these P3HT fibrils have been determined [30,31].

Additionally, multiple electron tomography (ET) studies by van Bavel et al. have been conducted to obtain three-dimensional reconstructions of the P3HT:PCBM bulk-heterojunction in order to understand the dispersion of the P3HT and PCBM domains throughout the P3HT:PCBM bulk-heterojunction. From these studies, relationships between the performance of P3HT:PCBM devices and their domain sizes [32] and their P3HT dispersions [27,33,34] have also been drawn, and it has been proven that, in addition to P3HT and PCBM domains, there is also a third, mixed P3HT:PCBM domain within these bulk-heterojunction layers [35,36].

Although this is not a comprehensive list of every morphological study of P3HT:PCBM bulk-heterojunctions, these examples do demonstrate how many structure-property relationships have already been determined relating the morphology of a P3HT:PCBM bulk-heterojunction to the overall organic photovoltaic device performance. However, what has not been studied as extensively are the optoelectronic

properties and the electronic structure of the P3HT:PCBM bulk-heterojunction, specifically at the P3HT/PCBM interface.

1.1.2.2. Characterizing the Electronic Structure of P3HT:PCBM BHJs

Very few studies have measured the optoelectronic properties of P3HT, PCBM, and P3HT:PCBM bulk-heterojunctions. The optoelectronic properties are typically described by either the energy-dependent complex dielectric function, where ε_1 is the real part of the complex dielectric function and ε_2 is the imaginary part of the complex dielectric function (Equation 1), or the energy-dependent complex index of refraction (Equation 2), where *n* is the index of refraction and *k* is the extinction coefficient [37].

$$\varepsilon(E) = \varepsilon_1(E) + i\varepsilon_e(E) \qquad \text{Equation 1}$$

$$\tilde{n}(E) = n(E) - ik(E) \qquad \text{Equation 2}$$

These two equations are related to each other via the following relationships [37]:

$$\varepsilon_1(E) = n^2(E) - k^2(E) \qquad \text{Equation 3}$$

$$\varepsilon_2(E) = 2 * n(E) * k(E) \qquad \text{Equation 4}$$

Thus, if either the complex dielectric function or the complex index of refraction is known, it is possible to extract the other. As will be discussed in Section 2.2.1.3, peaks in

ε_2 can be correlated to specific single electron transitions from the occupied states in the valence band to unoccupied states in the conduction band [38]. Thus, it should be possible to extract information about the electronic structure at a P3HT/PCBM interface within a P3HT:PCBM bulk-heterojunction by obtaining ε_2, analyzing which single electron transitions are observed, and correlating these transitions to specific molecular orbitals (which may or may not be changing at the interface).

There are some reports of the optoelectronic properties of P3HT, PCBM, and P3HT:PCBM blends in the literature. The refractive index, *n(E)*, and the extinction coefficient, *k(E)*, have been obtained for pure P3HT films, pure PCBM films, an P3HT:PCBM blended films via spectroscopic ellipsometry (which will be discussed in Section 2.3) [20,39–43]. However, from these reports, vastly different values of *n(E)* and *k(E)* were determined, which can be attributed to the different methods used to prepare the films. Furthermore, none of these papers use their results to identify the single electron transitions that have been measured by their data. This makes sense for the case of P3HT:PCBM blends as spectroscopic ellipsometry does not have the necessary spatial resolution to probe domains on the order of nanometers, but these single electron transitions could have been measured and identified for the bulk P3HT and bulk PCBM layers. However, even if these identifications are made for bulk P3HT and PCBM films, it is not possible to perform a similar analysis at the P3HT/PCBM interface of a P3HT:PCBM blended film as spectroscopic ellipsometry cannot probe the optoelectronic properties with the nanometer spatial resolution necessary to differentiate between P3HT and PCBM domains (domain size is ~10 nm).

Fortunately, there is an analytical electron microscopy technique that fulfills this need. Using electron energy-loss spectroscopy (EELS), which will be discussed in Section 2.2, within a scanning transmission electron microscope (STEM), the complex dielectric function (and, therefore, the complex refractive index) can be obtained with spatial resolutions on the order of nanometers, which makes EELS an ideal technique for measuring the electronic structure of *actual* P3HT/PCBM interfaces in P3HT:PCBM bulk-heterojunctions. However, very few EELS measurements have been made for pure P3HT, pure PCBM, or P3HT:PCBM blends. Figure 1.4 shows an overlay of the low-loss EELS spectra of pure P3HT [29–31,44,45], pure PCBM [29–31,44,45], and P3HT:PCBM blends [29,45,46] that had been reported in the literature prior to this work.

In examining the spectra shown in Figure 1.4, one obvious observation is that (similar to the spectroscopic ellipsometry measurements) there are numerous differences in all of the reported spectra. Most of these data were collected for the purposes of EFTEM imaging, and, as such, these data were collected with relatively low energy resolutions. This explains why many of the low-loss features are unresolvable in some of the data sets shown. However, it is extremely important that, for the accurate extraction of the optoelectronic properties from EELS data, that all of the peaks are resolvable; otherwise, the extracted complex dielectric functions could be inaccurate, leading to incorrect interpretations of the electronic structures of these materials. Furthermore, none of these groups actually extracted the optoelectronic properties (such as the complex dielectric function) from their collected EELS data, which means that the complex dielectric

functions have not yet been determined from EELS measurements of P3HT, PCBM, or at P3HT/PCBM interfaces.

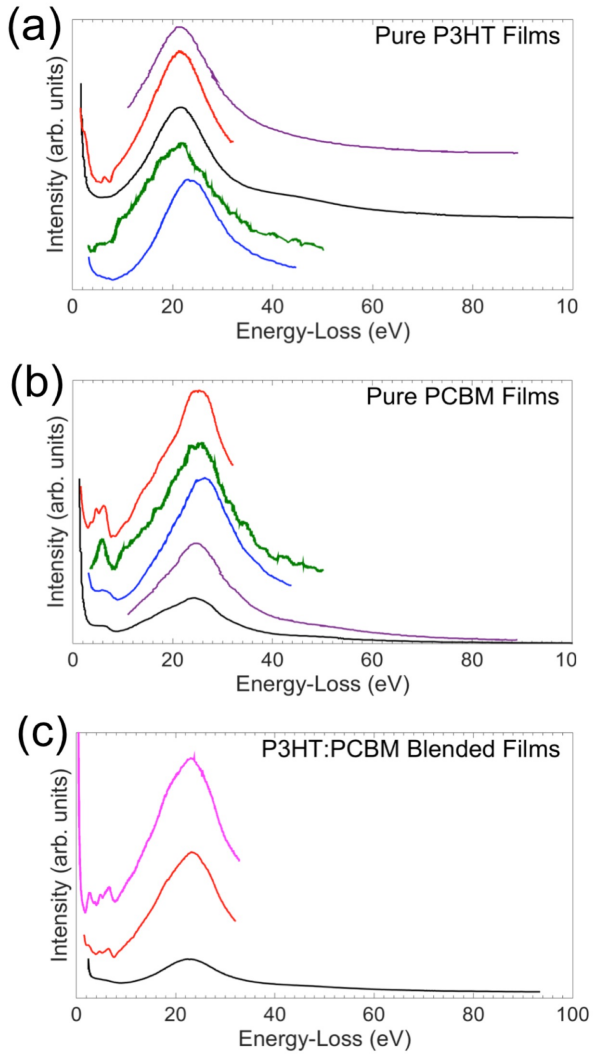

Figure 1.4: Previous EELS measurements reported in the literature (prior to this work) for (a) pure P3HT, (b) pure PCBM and (c) P3HT:PCBM blends, from references: [29] – red, [30] – green, [31] – purple, [44] – blue, [45] – black, and [46] – pink.

1.1.2.3. Research Motivation and Goals

While the morphology of the P3HT:PCBM bulk-heterojunction has been extensively studied, there is a major gap in the knowledge of the electronic structure at the donor/acceptor interface in P3HT:PCBM organic photovoltaics. It is vital that the electronic structure at the donor/acceptor interface is completely understood, as this could explain why certain structure-property relationships have been observed during various morphological characterization studies of the P3HT:PCBM bulk-heterojunction.

Given the size of the P3HT and PCBM domains in the bulk-heterojunction layer of these OPVs, a technique in which the optoelectronic properties can be obtained with nanometer spatial resolution is required. Fortunately, with electron energy-loss spectroscopy measurements conducted in a scanning transmission electron microscope, it is possible to measure the complex dielectric function at the donor/acceptor interface. Thus, the primary goals for the organic photovoltaics studies included in this dissertation are to:

1. Prove that reliable EELS data can be collected for electron beam-sensitive materials, such as P3HT and PCBM.
2. Use EELS to obtain standard spectra for P3HT and PCBM, from which the optoelectronic properties can be extracted.
3. Collect EELS data at donor/acceptor interfaces in actual P3HT:PCBM bulk-heterojunction OPVs.

4. Compare the standard EELS spectra for P3HT and PCBM to the signal collected at the donor/acceptor interface in an attempt to determine how the signal varies at this interface.

The culmination of this work will be discussed in Chapters 3 and 4.

1.2. Other Functional Electron Beam-Sensitive Materials

While the bulk of this dissertation does focus on organic photovoltaics, OPVs are just one example of new and exciting technologies based on electron beam-sensitive functional materials. In the following sections, two other examples of such functional materials will be described, and the research motivation/goals will be outlined.

1.2.1. Vanadium Tetracyanoethylene, $V[TCNE]_{x\sim2}$

Organic materials have garnered research interest as thin film magnets for many of the same reasons that they did in the field of organic photovoltaics. For instance, the properties of the thin film magnets can be tuned based on the chemical make-up of the organic thin films [47,48], the thin film magnets can be deposited onto various (including flexible) substrates [49,50], and the thin films can be processed using low-cost and low-temperature methods [47,49]. An example of such an organic thin film magnet is vanadium tetracyanoethylene. $V[TCNE]_x$, where x~2, is an organic-based ferrimagnetic semiconductor (see Figure 1.5 for a schematic) that is of considerable research interest due to its relatively high magnetic ordering temperature, which has been reported to be

greater than 600 K [50,51]. This high magnetic ordering temperature means that this material exhibits magnetic ordering at room temperature [49–54], which, along with the other typical properties of organic devices mentioned previously, make it an attractive material for a variety of applications, including magnetic shielding [47], magnonic circuits [50], and spintronic devices [51,54–56].

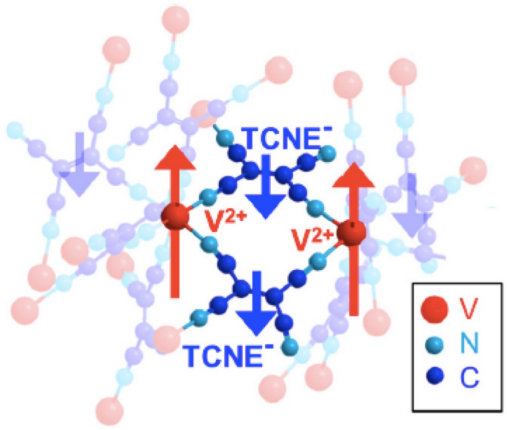

Figure 1.5: Schematic of $V[TCNE]_{x\sim2}$. This figure was originally published by reference [49].

1.2.1.1. Background and Previous Studies

The ferrimagnetic ordering of this thin film magnet arises due to the interaction of the magnetic moments between the V^{2+} electrons (shown in Figure 1.5 in red) and the $[TCNE]^-$ molecules (shown in Figure 1.5 in blue) [49]. As shown in this figure, although the magnetic moments (denoted by the arrows) are in opposite directions to one another,

they are of different magnitudes, preventing complete annihilation. Thus, a spontaneous magnetization remains, resulting in the ferrimagnetic properties observed for $V[TCNE]_{x\sim2}$ thin films [55]. Many studies have been conducted to determine the magnetic properties of $V[TCNE]_{x\sim2}$ thin films [48–50,53,55,56]. However, what have been less studied are the optoelectronic properties.

As mentioned previously, in addition to being an organic-based ferrimagnetic material, $V[TCNE]_{x\sim2}$ is also a semiconductor. Thus, energy diagrams have been proposed for this semiconductor [49,52], as summarized in Figure 1.6a. In this figure, various transitions have been labeled along with the corresponding energies of the transitions. For instance, shown in blue is the π to π^* transition of ~1.2 eV for the $[TCNE]^-$ molecule [52]. The green arrow denotes the splitting of the π^* orbital due to a Coulombic repulsion [53] with an energy of U_c = 1.9 eV (reference [52]) or U_c = 2.0 eV (reference [49]). In between this π^* orbital splitting of the $[TCNE]^-$ molecule is the t_{2g} orbital of the V^{2+} ions, as discussed in references [49] and [52], which is separated from the π^*+U_c state by 0.5 eV (shown in red). Thus, the proposed bandgap would be 0.5 eV since these t_{2g} electrons of the V^{2+} ions are the highest occupied states, and the π^*+U_c orbitals would be the lowest unoccupied states. Additionally, a transition could occur from the π orbital of the $[TCNE]^-$ molecules directly to the π^*+U_c orbital (shown in purple), which would result in a transitional energy of about 3.0 eV (reference [53]) or 3.1 eV (reference [52]). Some of these transitions have been measured using NIR-UV-Vis [52,53], an example of which is shown in Figure 1.6b.

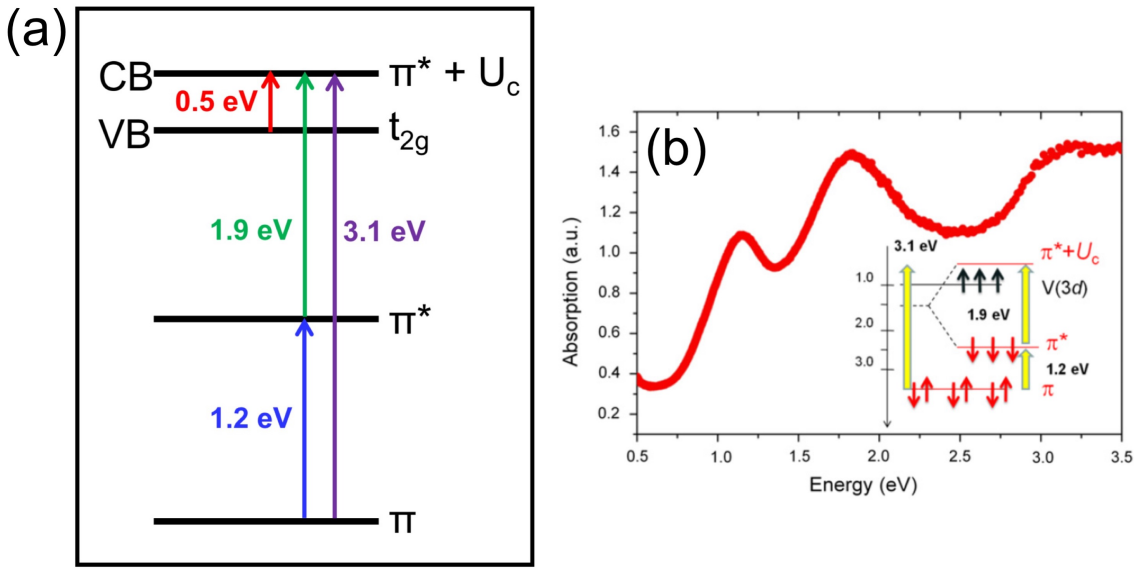

Figure 1.6: (a) Known electron transitions as identified in the literature [49,52]. The π and π* states are attributed to the $[TCNE]^-$ molecule, and the t_{2g} state is attributed to the V^{2+} ions. (b) NIR-UV-Vis measurements of a $V[TCNE]_{x\sim2}$ thin film on top of a sapphire substrate demonstrating how known electronic transitions (see inset) have been previously measured for $V[TCNE]_{x\sim2}$. Part (b) of this figure was originally published in reference [52].

However, from these NIR-UV-Vis measurements, it is not possible to extract the optoelectronic properties, and, to the best of the author's knowledge, no other measurements have been made to determine either the complex dielectric function or the complex refractive index. These properties are important because they reveal insight into the semiconductor behavior of the material, and, as such, should not be disregarded. The fact that these properties, thus far, have been overlooked is likely attributed to the air-sensitivity of $V[TCNE]_{x\sim2}$ thin films [52,54], as it would be simple to measure these

properties for a bulk $V[TCNE]_{x\sim2}$ film using a technique such as spectroscopic ellipsometry. Unfortunately, $V[TCNE]_{x\sim2}$ thin films degrade rapidly when exposed to air [47], which is why many experiments keep $V[TCNE]_{x\sim2}$ samples in controlled environments (i.e. argon-gas or vacuum) during the sample transport and data acquisitions [49,52–54,56]. Thus, in order to measure these optoelectronic properties, it is necessary that the thin films remain in a controlled environment, such as in a glovebox or vacuum; otherwise, whatever optoelectronic properties are measured will not be representative of the pure $V[TCNE]_{x\sim2}$ thin films but of an oxidized $V[TCNE]_{x\sim2}$ thin film.

1.2.1.2. Research Motivation and Goals

Because of the air-sensitivity of $V[TCNE]_{x\sim2}$ thin films, only bulk characterization techniques have been used to study these films. Although many important properties have been determined for $V[TCNE]_{x\sim2}$ as a result of these measurements (as discussed previously), there is still a large gap in the literature in terms of how certain properties vary throughout these thin films. For instance, while the oxidation state has been determined to be $\sim V^{2+}$ for bulk films of $V[TCNE]_{x\sim2}$ [47,48,54], it is currently unknown whether or not the oxidation state is consistent throughout the growth direction of the films. It could be that, depending on the growth parameters used, that the oxidation state differs at the bottom of the film as compared to the top of the film. Also, while there are models depicting the known single electron transitions available in $V[TNCE]_{x\sim2}$ films

[49,52], these transitions have never been measured with high spatial resolution. This information is critical, especially as knowing how the optoelectronic properties vary at interfaces could be crucial for the designing of future devices. Fortunately, these material's properties can be determined with high spatial resolution via electron energy-loss spectroscopy (EELS) measurements conducted in a scanning transmission electron microscope (as discussed in more detail in Section 2.2). However, the primary factor preventing using a scanning transmission electron microscope to measure such material's properties is that the sample must be exposed to air during the sample loading process. Thus, the first goal in the study of $V[TCNE]_{x\sim2}$ thin films will be to:

1. Develop a method to circumvent the air-sensitivity issue preventing the acquisition of data using a scanning transmission electron microscope.

Then, once such a method has been developed, the goals of this work will be to:

2. Use EELS to extract the optoelectronic properties of $V[TCNE]_{x\sim2}$ and determine how they vary spatially throughout the $V[TCNE]_{x\sim2}$ film.
3. Use EELS to extract determine the oxidation state of the vanadium ions in $V[TCNE]_{x\sim2}$ and determine how it varies spatially throughout the $V[TCNE]_{x\sim2}$ film.

The culmination of this work will be discussed in Chapter 5.

1.2.2. Lead-Free Halide Double Perovskites: Background & Motivation/Goals

Similar to organic photovoltaics, perovskite solar cells have recently emerged as a new and exciting alternative to traditional inorganic solar cells. As the name suggest, these solar cells use perovskites, which are a class of materials with the ABX_3 type structure (Figure 1.7), as the photoactive material [57]. In these types of solar cells, the perovskite is typically an organic-inorganic lead halide perovskite (also referred to as an organometal trihalide perovskite) in which the 'A' site is an organic material – methylammonium ($CH_3NH_3^+$, abbreviated MA), the 'B' site is lead (Pb), and the 'C' site is a halide (X = F, Cl, Br, I) [57,58]. The first major report discussing the use of organic-inorganic lead halide perovskites in solar cells was released in 2009 by reference [59]. In this report, a power conversion efficiency of 3.8% was obtained for a solar cell in which $CH_3NH_3PbI_3$ nanoparticles were deposited onto a TiO_2 surface in order to sensitize the TiO_2 (essentially creating a dye-sensitized solar cell) [59]. However, it was not until 2012 when reference [60] showed that thin films of perovskites could be spin-coated that many in the solar community turned their attention to the development of perovskite solar cells. In this work, a thin film of a mixed perovskite – $CH_3NH_3PbI_2Cl$ – was spin-coated onto a mesoporous Al_2O_3 layer, thereby creating an extremely thin absorber solar cell with an efficiency of 10.9% [60]. In the few years since that paper, the efficiency of perovskite solar cells has increased to 22.7% (not stabilized) [13]. This huge improvement in the power conversion efficiency is remarkable given the relatively short time in which the solar community has been utilizing perovskites in their devices.

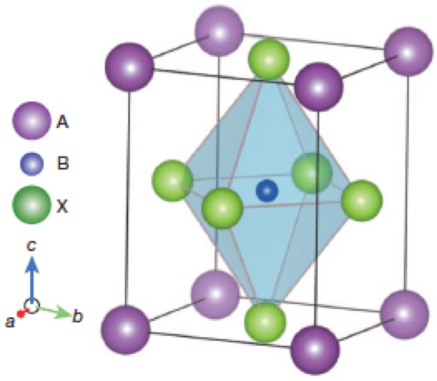

Figure 1.7: Perovskite crystal structure. In the organometal trihalide perovskites used in solar cells, the A site is methylammonium ($CH_3NH_3^+$), the B site is Pb, and the X site is a halide. This figure was originally published in reference [61].

However, although the efficiencies of perovskite solar cells have increased rapidly over the last few years, they are not yet a viable replacement for traditional inorganic solar cells. One of the major reasons preventing the implementation of perovskite solar cells is that these solar cells degrade when exposed to normal operating conditions (i.e. moisture, UV radiation, temperature) [57,58,62]. Nevertheless, even if the stability issues are resolved, the inclusion of Pb has raised toxicological concerns about the use of perovskites in solar cells [57,62,63]. However, if alternative lead-free halide perovskites could be developed, these concerns could be eliminated, and, assuming that the stability issues are also resolved, perovskite solar cells could emerge as one of the predominant solar technologies.

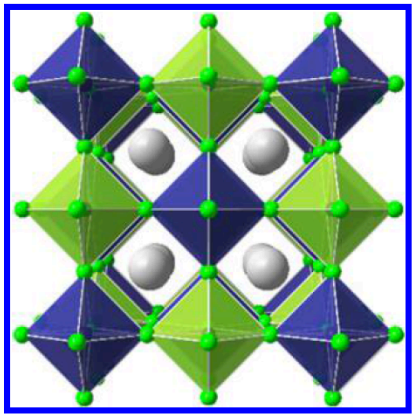

Figure 1.8: Crystal structure of $Cs_2AgBiCl_6$, a lead-free halide double perovskite. The gray spheres are Cs^+ ions, the green spheres are Cl^- ions, the blue polyhedra are Ag centered octahedra, and the green polyhedra are Bi centered octahedra. This figure was originally published in reference [64].

Recently, two lead-free halide double perovskite ($A_2BB'X_6$ – see Figure 1.8) semiconductors – $CsAgBiBr_6$ and $Cs_2AgBiCl_6$ – have been shown to have similar bandgaps as $MAPbBr_3$ and $MAPbCl_3$ [64]. For instance, the bandgap of $Cs_2AgBiBr_6$ is 2.19 eV (indirect), which compares favorably to the 2.26 eV (direct) bandgap of $MAPbBr_3$ [64]. Similarly, the bandgap of $CS_2AgBiCl_6$ is 2.77 eV (indirect), whereas the bandgap of $MAPbCl_3$ is 3.00 eV (direct) [64]. Furthermore, $Cs_2AgBiCl_6$ demonstrates high stability when exposed to both air and sunlight over a period of a month [64]. These observations suggest that it may be possible to replace organometal trihalide perovskites with these lead-free halide double perovskites in future solar cells, thus eliminating the concerns associated with the inclusion of lead in such devices.

However, these materials are still relatively new and the optoelectronic information necessary to determine their validity as solar materials has not been obtained. For

instance, knowing how the absorption coefficient varies with energy (or, conversely, wavelength) will have implications regarding the ability of these materials to absorb photons. Additionally, obtaining the complex refractive index and complex dielectric function (Equations 1 and 2) will provide information about the electronic behavior of these materials, which should then provide insights into how well these materials would work in solar cells.

These measurements can be made over a large energy range (including the solar spectrum) using electron energy-loss spectroscopy (see Section 2.2 for an overview of EELS). Thus, the primary goal for the study of $Cs_2AgBiBr_6$ and $Cs_2AgBiCl_6$ is to provide fundamental measurements of the optoelectronic properties of these materials via electron energy-loss spectroscopy. Knowing these properties should then reveal whether or not these materials are appropriate for the use in perovskite solar cells.

The culmination of this work will be discussed in Chapter 6.

Chapter 2. Experimental Methodologies

Most of the results that will be reported in Chapters 3 – 6 were collected using one of two experimental methods: (1) electron energy-loss spectroscopy collected in a scanning transmission electron microscope or (2) spectroscopy ellipsometry. Both methods will be discussed in this chapter.

2.1. Scanning Transmission Electron Microscope (STEM)

Scanning transmission electron microscopes (STEMs) can be used to image and analyze samples with atomic spatial resolution by using electromagnetic lenses to focus a beam of electrons into a small probe that is incident upon the sample [38]. Because samples used in both STEM and TEM measurements are very thin (usually less than 100 nm), the electron beam will pass through the specimen, from which various signals may be measured. For instance, after the electron beam passes through the sample, bright-field (BF) images can be obtained from the electrons that elastically scatter at low angles, high-angle annular dark-field (HAADF) images can be obtained from the electrons that are elastically scattered at high angles onto an annular detector, energy dispersive X-ray spectra (EDX) can be collected from X-rays that are excited in the sample by the incident electron beam, or electron energy-loss spectra (EELS) can be used to measure the energy-losses of the incident electrons after they have interacted with the sample [38,65]. It is the

acquisition of EELS data that will be the primary focus of this work. (For a more in-depth overview of STEMs, see references [38] and [65]).

2.2. Electron Energy-Loss Spectroscopy (EELS)

STEM-EELS is an analytical electron microscopy technique that can be used to obtain, with high spatial resolution, the dielectric response, band gap, composition, oxidation states of the individual elements in a compound, and local bonding environment, amongst other materials properties [38]. This ability to collect such varied information with high spatial resolution makes EELS an extremely versatile analytical tool within the STEM. In this section, some of the fundamental concepts necessary to understand the data presented in this work will be described. However, the author directs the reader to the seminal book by Egerton (reference [66]) for the complete, detailed discussion of all of these concepts.

A basic schematic demonstrating how STEM-EELS data is acquired is shown in Figure 2.1. In STEM-EELS, a focused electron beam is transmitted through a thin sample, during which the electrons of the incident beam can interact elastically or inelastically with the sample. The transmitted electron beam then passes through a magnetic spectrometer (which will be described in more detail later in this section), which disperses the transmitted electron beam based on the amount of energy that the beam electrons have lost due to interactions with the sample, thus forming an EELS spectrum.

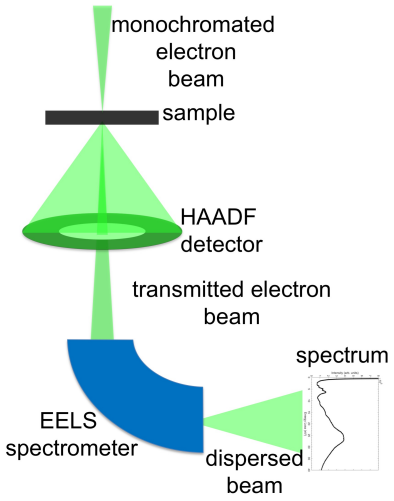

Figure 2.1: Schematic of the EELS experimental apparatus.

As shown in Figure 2.1, the incident electron beam can be monochromated in order to improve the energy resolution of the collected EELS data. (All of the EELS data that will be discussed in the following four chapters were collected using a monochromated electron beam). Using a monochromator improves the energy resolution of the EELS data collected by reducing the energy spread of the incident electron beam [66]. Every incident electron beam has an inherent spread in the beam due to the Boersch effect in which electrons interact with each other via Columbic forces [66], which reduces the energy resolution achievable in the microscope [67–69]. However, a monochromator can be used to disperse the electron beam, and then a slit can preferentially select the part of the beam that is the most monochromatic, reducing the energy spread of the beam before it interacts with the sample [38,65,66,70]. With the use of a monochromator, it is possible to collect EELS spectra with energy resolutions on the order of approximately 10 meV

[71,72], whereas, prior to the advent of monochromators in the STEM, spectra could only be collected with energy resolutions on the order of ~0.3 eV, assuming that the STEM used a cold field emission gun (FEG) source [38]. Additionally, monochromating the electron beam results in a more symmetric ZLP [65], which is critical for the appropriate removal of the ZLP, as described later in Section 2.2.1.1. However, one major drawback to monochromating the electron beam is that the number of electrons that are now incident upon the sample is significantly reduced, which adversely affects the amount of current available with which to collect EELS spectra [38,65]. This effect is usually compensated by using longer acquisition times [66]. However, it is worth noting that this effect should not be much of an issue with electron beam-sensitive samples since lower current (fewer incident electrons) typically correlates to less observable beam damage. Two primary types of monochromators (Wien and alpha filters) will be discussed in more detail in Section 3.4.1.

Once the monochromated electron beam has passed through the sample, an EELS spectrum may be acquired from the transmitted electron beam. The electrons comprising this transmitted electron beam will either have interacted elastically (lost little-to-no kinetic energy) or interacted inelastically with the sample (lost an appreciable amount of kinetic energy) [38]. Thus, each of the electrons in the transmitted beam will have a different value of energy-loss, depending on the type of interactions they have had with the sample. Plotting how many electrons have lost a specific energy versus the energy-loss of those electrons forms an energy-loss spectrum. However, to form this spectrum, it is first necessary to disperse the transmitted electrons by their energy-loss, and this is

accomplished through the use of a magnetic spectrometer [38,65]. The transmitted electron beam enters the spectrometer through the entrance aperture, at which point the electrons travel via a drift tube and are deflected by the magnetic field of a magnetic prism [38]. The amount by which the electrons are deflected depends on the energy of the electrons, themselves; if the electrons have lost more energy, they will be deflected more [38]. This is the dispersive action of the spectrometer. The magnetic prism also serves to focus the on- and off-axis electrons onto the dispersion plane of the spectrometer [38]. A series of projection lenses follow the magnetic prism, and the final EELS spectrum is then collected on a detector, such as a charge-couple diode (CCD) array [38,65].

Depending on the range of energy-losses measured, the EELS spectrum is either designated as a low-loss spectrum or a core-loss spectrum. These will both be described in more detail in the following sections.

2.2.1. Low-Loss EELS

Low-loss EELS (also known as valence-loss EELS) refers to EELS spectra consisting of energy-losses less than 50 eV [38,66,73]. Energy-losses in this regime correspond to interactions the incident electrons have had with the valence (or outer shell) electrons of the sample [38,66,73]. From these spectra, it is possible to measure a material's band gap, dielectric response, and charge carrier density with high spatial resolution [38]. Additionally, transitions from the valence band to the conduction band can be determined, and excitons, plasmons, and phonons (assuming a high enough energy

resolution is used) can be observed [65]. Even the specimen thickness can be measured using low-loss EELS [38,65].

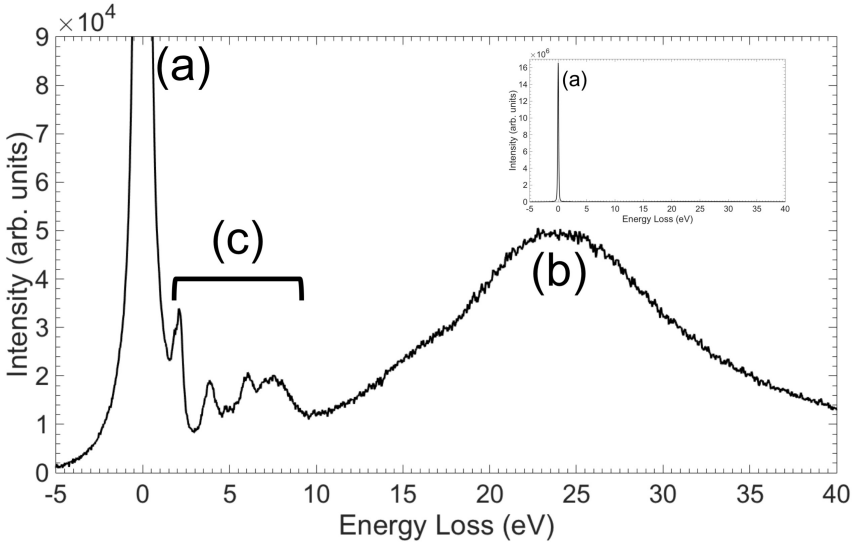

Figure 2.2: A representative low-loss EELS spectrum. The inset shows the entire intensity of the (a) zero-loss peak. Additionally, low-loss spectra are comprised of (b) a plasmon peak, and (c) low-loss structure that could be analyzed to extract optoelectronic information.

A representative low-loss EELS spectrum with various features identified, including (a) the zero-loss peak, (b) the plasmon peak, and (c) low-loss structure, is shown in Figure 2.2. The zero-loss peak (ZLP), which will be discussed more in Section 2.2.2.1, is composed of signals corresponding to electrons that have lost little-to-no energy as they have passed through the sample [38]. Because the samples investigated in the STEM are thin, this is the most intense feature in a low-loss EELS spectrum (as shown by the inset

in Figure 2.2), as most of the high-energy electrons from the incident beam will pass straight through the sample without any appreciable loss in energy. Although it is not useful for materials analysis, the ZLP is used to quantify the energy-resolution of the EELS spectrum collected, which is defined to be the energy spread of the ZLP at its full-width at half-maximum (FWHM) [38]. Additionally, the ZLP serves as a good reference for aligning EELS spectra [65].

The plasmon peak, which is typically the second most intense feature in the low-loss spectrum, corresponds to collective excitations of the valence electrons in the sample by the incident electron beam [38,66]. Essentially, as the fast electrons from the incident electron beam pass through the sample, they induce a local electric field [66]. When the valence electrons in the sample, modeled as the free-electron gas, feel this electric field, they respond via a collective oscillation, which has a characteristic frequency of ω_p (rad/s) [38,65,66]. This characteristic frequency represents the frequency at which the valence electrons would continue to oscillate barring any damping from the sample's atomic lattice [66]. This oscillation frequency can be determined from the energy of the plasmon peak, E_p, as $E_p = \hbar\omega_p$ [65,66]. Furthermore, the oscillation frequency (and, therefore, the energy of the plasmon peak) can also be related to the valence electron density (number of valence electrons per unit volume), as:

$$\omega_p = \sqrt{ne^2/\varepsilon_0 m} \qquad \text{Equation 5}$$

where n is the valence electron density, e is the charge of an electron, ε_0 is the permittivity of free space, and m is the mass of the electron [38,66]. Thus, via low-loss EELS measurements, it is possible to determine the number of valence electrons in the sample if the unit cell volume is known. Or, conversely, if it is known that the number of valence electrons is constant, it is possible to determine any changes in the size of the unit cell volume.

Other features in the low-loss spectrum are indicative of electronic transitions [38]. Further analysis of the low-loss spectrum, which will be discussed in Sections 2.2.1.1 through 2.2.1.3, can then be conducted to extract optoelectronic properties, such as the complex dielectric function, the complex refractive index, and the energy-dependent absorption coefficient spectrum from these low-loss features [38].

Additionally, as previously mentioned, low-loss EELS spectra can be used to measure the thickness, *t*, of a sample, and this is accomplished using the log-ratio method given by:

$$\frac{t}{\lambda} = \ln\left(\frac{I_t}{I_0}\right) \qquad \text{Equation 6}$$

where λ is the mean free path of inelastic scattering, I_t is the area under the entire low-loss spectrum, and I_0 is the area under only the ZLP [66]. If the mean free path of inelastic scattering is known for a material, then the absolute value of the thickness can be determined.

2.2.1.1. Zero-Loss Peak Removal

The zero-loss peak (ZLP) is primarily representative of elastic interactions the incident electron beam has had with the specimen [38,65,66]. Most commonly, the ZLP signal is due to incident electrons that have passed straight through the thin specimen, although some signal may be due to inelastic interactions that cause very small energy-losses, such as phonon excitations [38,66,73]. In general, however, the ZLP signal contributes little to the analysis of an EELS spectrum and prevents the extraction of optoelectronic properties from the low-loss EELS spectrum. Thus, analysis of any low-loss EELS spectrum first requires the removal of the zero-loss peak.

There are a variety of methods that may be used to remove the ZLP from low-loss spectra [38,74]. Most commonly (and in this work), the reflected-tail method is used via the EELS analysis software, DigitalMicrograph. In the reflected-tail method, the tail of the energy-gain (left) side of the ZLP is reflected to the energy-loss (right) side and subtracted from the original spectrum [74]. It is, therefore, necessary for this method that the ZLP is symmetric, which is the case for a well-aligned, monochromated electron beam [38,65].

Once the tail of the energy-gain side of the ZLP has been reflected to the energy-loss side, the reflected-tail routine in DigitalMicrograph will scale the reflected tail so that it is properly spliced with the rest of the ZLP [74]. This ZLP is then subtracted from the collected spectrum, leaving behind a resultant spectrum comprised of only the inelastic interactions that the incident beam has had with the sample. Figure 2.3 shows the result of performing a ZLP removal using the reflected-tail method, where the collected low-

loss spectrum is shown in black, the modeled ZLP is shown in blue, and the resultant inelastic spectrum is shown in red.

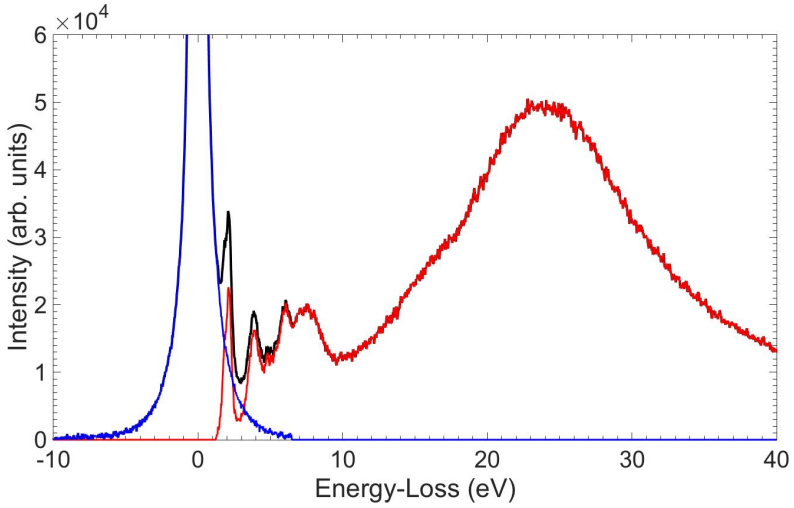

Figure 2.3: An example of using the reflected-tail method to remove the zero-loss peak (in blue) from the collected low-loss spectrum (in black). The remaining signal is attributed to the inelastic spectrum (in red).

As shown in Figure 2.3, the energy-loss (right) side of the ZLP mirrors the energy-gain (left) side of the ZLP. Exactly how much of the tail that is reflected from the energy-gain side of the ZLP to the energy-loss of the ZLP is dictated by the user by selecting a reflected-tail cutoff value [74]. It is worth noting that this introduces some subjectivity into the ZLP removal process, which is why certain analyses, such as band-gap onset measurements, may be difficult to perform via EELS [75].

2.2.1.2. Deconvolution of the Spectrum

Once the ZLP has been removed from the low-loss spectrum, all that remains are signals due to inelastic interactions the incident electron beam has had with the sample. This inelastic spectrum is a convolution of both single scattering events, in which the incident electron beam has had only one interaction with the sample, and plural scattering events, in which the incident electron beam has had multiple interactions with the sample [38]. It is known that the single scattering distribution, $J^1(E)$, which is comprised of only those single scattering events, is related to the complex dielectric function, $\varepsilon(E)$, as:

$$J^1(E) = \frac{I_0 t}{\pi a_0 m_0 v^2} \operatorname{Im}\left[\frac{-1}{\varepsilon(E)}\right] \ln\left[1 + \left(\frac{\beta}{\theta_E}\right)^2\right] \qquad \text{Equation 7}$$

where I_0 is the intensity of the ZLP, t is the thickness of the specimen, a_0 is the Bohr radius, m_0 is the electron rest mass, v is the speed of the primary electrons, β is the collection semi-angle, and θ_E is the characteristic scattering angle for a specific energy-loss ΔE [38,66]. More simply stated:

$$J^1(E) \approx \operatorname{Im}\left[\frac{-1}{\varepsilon(E)}\right] \qquad \text{Equation 8}$$

Thus, it is possible to determine $\operatorname{Im}[-1/\varepsilon(E)]$ if the inelastic spectrum is deconvoluted and the single scattering distribution is obtained.

For the low-loss EELS data presented in this work, the single scattering distribution is obtained by deconvoluting the inelastic spectrum using the Fourier-Log method, as

described in reference [66] (although other methods do exist) [38,66], utilizing the automated routine in DigitalMicrograph [74].

2.2.1.3. Analysis to Extract Optoelectronic Information

Once the single scattering distribution has been obtained, $\mathrm{Im}[-1/\varepsilon(E)]$ can be determined by dividing $J^1(E)$ by all of the constants on the right-hand side of Equation 7. Furthermore, the dielectric function is a response, or causal, function, which means that if either the real or imaginary part of the function is known, the correlating part can also be determined [65,76]. Thus, in this case, by knowing $\mathrm{Im}[-1/\varepsilon(E)]$, it is possible to determine $\mathrm{Re}[1/\varepsilon(E)]$ [38,65], and the method by which to accomplish this is the Kramers-Kronig analysis, which is described in more detail in reference [66]. The Kramers-Kronig transformation:

$$\mathrm{Re}\left[\frac{1}{\varepsilon(E)}\right] = 1 - \frac{2}{\pi} P \int_0^\infty \mathrm{Im}\left[\frac{-1}{\varepsilon(E')}\right] \frac{E' dE'}{(E')^2 - E^2} \qquad \text{Equation 9}$$

where P is the Cauchy principal part of the integral [66], can be used to obtain $\mathrm{Re}[1/\varepsilon(E)]$ via the Fourier transform methods described in reference [76]. Then, once $\mathrm{Re}[1/\varepsilon(E)]$ has been determined, the complex dielectric function, ε(E), can be written as:

$$\varepsilon(E) = \varepsilon_1 + i\varepsilon_2 = \frac{\mathrm{Re}[1/\varepsilon(E)] + i\mathrm{Im}[-1/\varepsilon(E)]}{(\mathrm{Re}[1/\varepsilon(E)])^2 + (\mathrm{Im}[-1/\varepsilon(E)])^2} \qquad \text{Equation 10}$$

from which, $\varepsilon_1(E)$ and $\varepsilon_2(E)$ can be determined [66]. Furthermore, by knowing the value of the refractive index for energies associated with visible light for an insulator or semiconductor, it is possible to extract absolute values of $\mathrm{Im}[-1/\varepsilon(E)]$ [66]. If, for Equation 9, $E = 0$, then:

$$\mathrm{Re}\left[\frac{1}{\varepsilon(0)}\right] = 1 - \frac{2}{\pi} P \int_0^\infty \mathrm{Im}\left[\frac{-1}{\varepsilon(E')}\right] \frac{E' dE'}{(E')^2} \qquad \text{Equation 11}$$

where $\mathrm{Re}[1/\varepsilon(0)]$ is approximately equal to $1/\varepsilon_1(0)$ since, for insulators and semiconductors, ε_2 is very small at low energies [66] (this is because $\varepsilon_2 = 2nk$ and k is usually 0 or close to 0 for insulators and semiconductors at 0 eV). Since $\varepsilon_1 = n^2 - k^2$ (Equation 3), this means that $\mathrm{Re}[1/\varepsilon(0)]$ can be related to the refractive index, n (again, assuming k is very small at 0 eV) [66], which is why a value for the refractive index is required as an input for the Kramers-Kronig analysis routine in DigitalMicrograph [74] used in the following chapters to obtain $\varepsilon_1(E)$ and $\varepsilon_2(E)$ from experimental EELS data.

The imaginary part of the complex dielectric function, $\varepsilon_2(E)$, can be used to identify specific single electron transitions of the sample [38]. These characteristic transitions occur when the energy that has been lost by the incident electrons, and, thus, given to one of the sample's valence electrons, is large enough that the valence electron can escape an occupied state in the valence band and move into an unoccupied state in the conduction band [38]. Low-loss EELS can be used to study these single electron transitions because the single-scattering distribution is related to the joint density of states, $\rho_J(E)$, as:

$$J^1(E) \propto \left|\int \psi_i e^{i\boldsymbol{q}\cdot\boldsymbol{r}} \psi_f^* d^3\boldsymbol{r}\right|^2 \rho_J(E) \qquad \text{Equation 12}$$

where q is the momentum vector, r is the position vector, $\psi_i(\boldsymbol{r})$ is the initial state, and $\psi_f(\boldsymbol{r})$ is the final state [66]. This density of states is known as the joint density of states because it is a convolution of the density of states for both the valence and conduction bands [66,77]. Thus, since $\varepsilon_2(E)$ is proportional to the joint density of states, features in the joint density of states should correspond to features in $\varepsilon_2(E)$ [78], which is why $\varepsilon_2(E)$ can be used to identify single electron transitions. An example of this analysis will be described in detail in Section 3.3.

Having determined $\varepsilon_1(E)$ and $\varepsilon_2(E)$, many other properties in addition to the single electron transitions can be extracted, such as the refractive index (n), and the extinction coefficient (k), (see Equations 3 and 4). Thus, low-loss EELS is extremely useful for measuring and determining optoelectronic information about the sample being studied.

2.2.1.4. Resolution Limits of Low-Loss EELS

Unfortunately, while the optoelectronic properties of a material can be obtained from low-loss EELS measurements with relatively high spatial resolution, it is not possible to achieve atomic resolution due to the delocalization of inelastic scattering [65]. Essentially, inelastic scattering events (which are used to obtain the optoelectronic properties) do not originate from a single point (i.e. an atom), but rather from a small range of spatial positions [79]. This is why the term ‘delocalization’ is used to describe

this phenomenon; the signal for a specific value of energy-loss is coming from a delocalized area of the sample due to small variances in both the scattering angle and impact parameter of the electrons comprising this signal [79]. Therefore, the spatial resolution of EELS measurements depends not only on the probe size, but also by how much the inelastic scattering is delocalized [65], as described by the localization diameter (d_{50}) [79]. This localization diameter, which is defined to be the diameter in which 50% of the inelastic scattering events are contained, can be approximated as:

$$d_{50} \sim 0.8\lambda \left[\frac{E_0}{E}\right]^{3/4} \qquad \text{Equation 13}$$

where E_0 is the energy of the incident electron beam, E is the value of energy-loss, and λ is the wavelength of the incident electrons [79]. Reference [65] has plotted the localization diameter as a function of energy-loss for three different energies of incident electron beam, as shown in Figure 2.4. It is worth noting that the authors adjusted the pre-factor value in Equation 13 from 0.8 to 0.5 based on comparisons with their own experimental data [65].

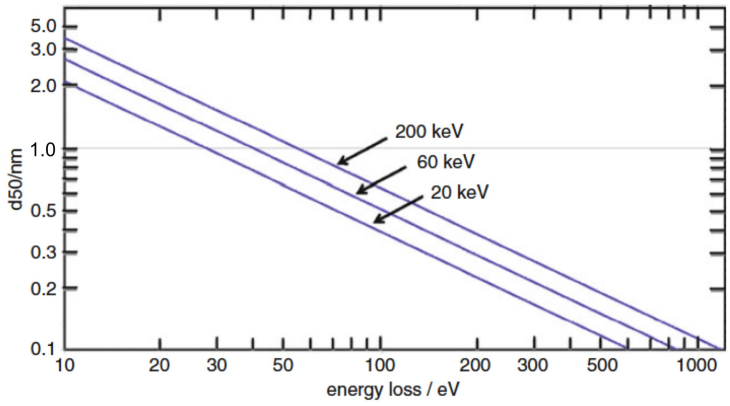

Figure 2.4: Calculated localization diameters (d_{50}) as it varies with energy-loss for various energies of incident electron beam (20 keV, 60 keV, and 200 keV). This plot was originally published in reference [65].

This plot shows that, even at a relatively low energy of the incident electron beam (60 keV), the localization diameter is larger than 1 nm for energy-losses below 30 eV, which is the energy range from which the optoelectronic properties are calculated. The authors in reference [65] suggest that 2 Å is an appropriate minimum for atomic spatial resolution, and so values of $d_{50} > 1$ nm will prevent the acquisition of atomic resolution EELS data in the low-loss region. These delocalization effects even prevent the acquisition of atomically resolved low-loss EELS data when the energy of the incident electron beam has been lowered to 20 keV (Figure 2.4) [65]. However, it is possible to collect these data with spatial resolutions on the order of just a few nanometers, which is still highly spatially-resolved.

As mentioned before, the spatial resolution of EELS data depends on both the probe size and the delocalization of the inelastic scattering, and, so, it can be defined to be:

$$d_{EELS} = \sqrt{d_{probe}^2 + d_{50}^2} \qquad \text{Equation 14}$$

where d_{EELS} is the spatial resolution achievable in an EELS measurement and d_{probe} is the diameter of the probe [65].

2.2.2. Core-Loss EELS

Instead of measuring interactions with the valence electrons of a sample, as in low-loss EELS, core-loss (also referred to as high-loss) EELS spectra measure interactions the incident electron beam has had with the inner shell (or core) electrons of the constituent atoms in the sample [38]. Core-loss EELS spectra typically correspond to spectra in which the energy-losses are above 50 eV [38,73]. Most often, these spectra provide information about the composition of a sample, although they can also be used to determine the oxidation states of the individual elements of a compound as well as information about the bonding and electronic structure [38]. An example core-loss spectrum is shown in Figure 2.5.

During a core-loss EELS acquisition, ionization events are measured. As the incident electron passes through the sample inelastically, the energy lost by the incident beam electron can be used to eject one of the core shell electrons of the sample into an unoccupied electronic state, thus ionizing the affected atom [38,73]. This ionization energy then corresponds directly to the energy-loss measured (i.e. the energy lost by the

incident electron) and can be used to identify the kind of atom ionized, and thus the composition of the sample [38,65,73]. For instance, the spectrum shown in Figure 2.5 measured the carbon-K edge, meaning that carbon is in the sample.

Core-loss EELS data can also be related to the density of states, $\rho(E)$, by the following:

$$I(E,\theta) \propto \frac{4\gamma^2}{a_0^2 q^4} \left| \int \psi_i e^{i\mathbf{q}\cdot\mathbf{r}} \psi_f^* d^3\mathbf{r} \right|^2 \rho(E) \qquad \text{Equation 15}$$

where $I(E,\theta)$ is the intensity of the ionization edge as a function of energy-loss and scattering angle, γ is the relativistic factor, a_0 is the Bohr radius, q is the momentum vector, r is the position vector, $\psi_i(\mathbf{r})$ is the initial state, and $\psi_f(\mathbf{r})$ is the final state [66,80]. This density of states is called the local density of states (LDOS) due to the highly localized nature of core-levels [66]. Furthermore, where l is the angular momentum, the majority of states observed in this local density of states will correspond to $\Delta l = 1$ transitions (although as long as transitions obey the dipole selection rule ($\Delta l = \pm 1$) they may be detected) resulting it what is actually an observation of the symmetry-projected density of states [66]. So, for instance, the carbon-K edge shown in Figure 2.5 is a representation of the symmetry-projected density of states for s → p transitions. It is worth noting that broadening effects beyond the instrumental energy resolution will affect the shape of core-loss EELS spectra. These effects include the initial state

broadening and the final state broadening, the details of which can be found in reference [66].

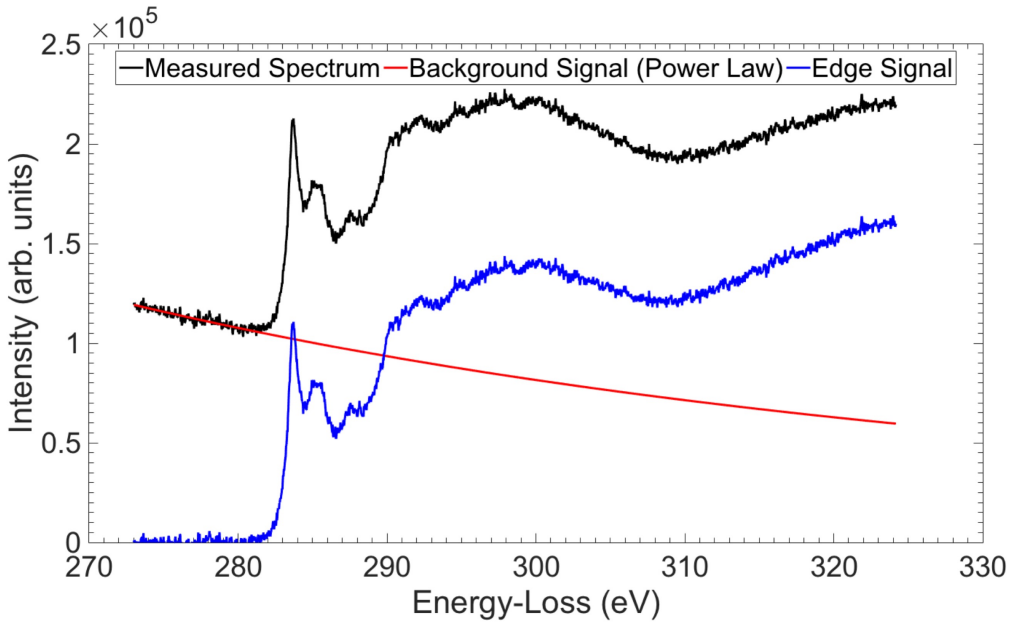

Figure 2.5: Example core-loss spectrum of the carbon-K edge. The measured spectrum is shown in black. A power law was fitted to the data prior to an energy-loss of 280.6 eV and was extrapolated out to the terminal energy-loss value (shown in red). This signal was subtracted from the measured spectrum, resulting in signals attributed only to the C-K edge (shown in blue).

Just as with low-loss EELS spectra, the core-loss EELS spectra require processing in order to extract useful information. The spectrum shown in Figure 2.5 is an example of the raw spectrum collected during the core-loss EELS measurement. This spectrum shows the carbon-K ionization edge sitting on a decreasing background, which is representative of electrons that have been inelastically scattered multiple times in random

orientations as they have passed through the sample [38]. Since these electrons that comprise the background signal are due to random scattering events, they do not provide any useful analytical information and must be subtracted from the core-loss spectrum. Generally, the background signal can be fit with a power law of the form:

$$I = AE^{-r} \qquad \text{Equation 16}$$

where I is the intensity, and A and r are both constants [38,65]. In using this routine in DigitalMicrograph, a small energy-loss window preceding the core-loss edge is selected, to which the power law is fit [74]. This fit is then extrapolated to the terminal energy of the core-loss EELS spectrum and subtracted from the raw data, leaving signal attributed only to the measured edge [74]. An example of this analysis is shown in Figure 2.5. Although the power law background subtraction routine is the most common, other fits can be used, such as exponential, polynomial, etc. [38,74], depending on which fit is most suitable for the experimental data. After having subtracted the background signal from the core-loss EELS spectrum, plural scattering can be removed from the edge signal via the Fourier-Ratio method, as described in references [66] and [74].

Once the core-loss EELS spectrum has been processed, it can be analyzed to determine information such as the composition and the electronic structure of a sample [38], all with high spatial resolution. In fact, the spatial resolution of core-loss EELS measurements is better than that for low-loss EELS data. Referring back to the plot shown in Figure 2.4, atomic resolution (as defined to be ~ 2 Å) can be achieved for a 60 keV electron beam for energy-losses greater than 340 eV, and even core-loss spectra for

energy-losses less than 340 eV can be collected with sub-nanometer spatial resolution (again, for a 60 keV electron beam) [65].

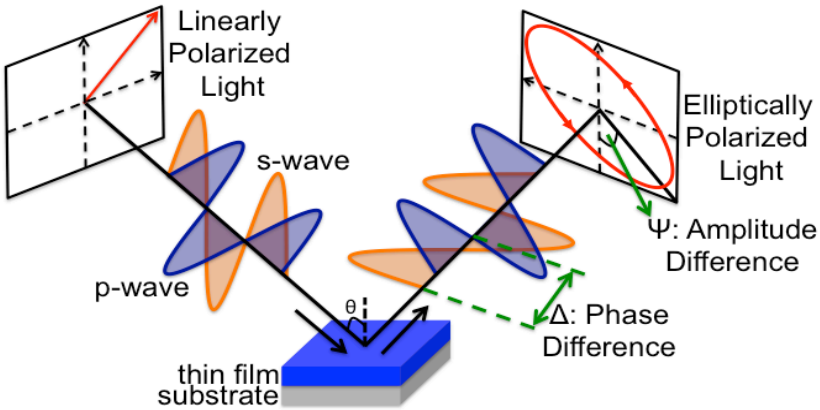

Figure 2.6: Schematic of the SE experimental set-up.

2.3. Spectroscopic Ellipsometry (SE)

Spectroscopic ellipsometry (SE) is a bulk characterization technique that can be used to obtain the refractive index, *n*, and the extinction coefficient, *k*, for a material [81–83]. In this section, a brief overview of the basic principles necessary to understand the spectroscopic ellipsometry experimental data shown later in this work will be described. For a more in-depth discussion of spectroscopic ellipsometry, the author refers the reader to references [83] and [82].

The general spectroscopic ellipsometry experimental set-up is shown in Figure 2.6. A linearly polarized light source consisting of two linearly polarized waves that are in-

phase (shown in Figure 2.6 as the s-wave and the p-wave) of a specific wavelength is directed onto the sample at a particular angle of incidence, θ [81]. When this linearly polarized light source hits the sample, reflection will occur, and from the reflected light, two experimental parameters can be measured: delta (Δ) and psi (Ψ) [81]. Δ is defined to be the change in the phase difference of the s- and p-waves after reflecting off of the sample, as given by:

$$\Delta = \delta_1 - \delta_2 \qquad \text{Equation 17}$$

where δ_1 is defined to be the phase difference between the s- and p-waves prior to hitting the sample, and δ_2 is defined to be the phase difference between the s- and p-waves after reflecting off of the sample [81,83]. Thus, unless the value of Δ is zero, then the s- and p-waves will no longer be in-phase, and the light measured on the detector will be elliptically polarized [81], as shown in Figure 2.6. Ψ, is related to the change in the amplitudes of the s- and p-waves after reflecting off of the sample, and can be given by:

$$\Psi = \tan^{-1}\left[\frac{|R^p|}{|R^s|}\right] \qquad \text{Equation 18}$$

where R^s and R^p are the reflection coefficients defined to be the ratios of the reflected amplitude to the incident amplitude for each wave [81,83]. Thus, Ψ contains information about the magnitude of the reflection coefficients. However, the reflection coefficients, R^s and R^p themselves (i.e. not their magnitudes) are what can be related to important

material parameters [81,83], and so the goal of a spectroscopic ellipsometry measurement is to determine their values. This determination can be accomplished via the fundamental equation of ellipsometry, which relates both Ψ and Δ to the ratio of the reflection coefficients given by ρ as [81,83,84]:

$$\rho = \frac{R_p}{R_s} = \tan(\Psi)\, e^{i\Delta} \qquad \text{Equation 19}$$

Thus, Ψ is related to the amplitude of ρ and Δ is related to the phase of ρ [83].

Having measured Δ and Ψ during a spectroscopic ellipsometry measurement, various oscillators (i.e. Lorentzian, Gaussian, etc.) can be used to build models of the experimental Δ and Ψ data, and a mean-squared error (MSE) minimization can be utilized to adjust the modeled values of Δ and Ψ to best fit the experimental values of Δ and Ψ [83]. Then, once the modeled values of Δ and Ψ have been optimized, the reflection coefficients can be determined [84], and *n(E)* and *k(E)* can be extracted [82]. It is important to emphasize that spectroscopic ellipsometry cannot be used to directly measure the values of *n* and *k;* rather they are determined from the models of Δ and Ψ. Lastly, by using variable angle spectroscopic ellipsometry (VASE), in which SE data is collected for multiple incident angles, it is possible to determine both the optical properties and the thickness of the film simultaneously [85].

For the spectroscopic ellipsometry measurements discussed in this dissertation, the spatial resolution was limited to ~2 mm due to the limitations of the light source used to make the probe. Additionally, the energy range over which data can be collected also

depends on the light source, and, for the ellipsometry used in the experiments that will be discussed throughout this dissertation, data could only be collected in the energy range of 0.5 – 4.5 eV. Thus, EELS, by comparison, is a much more powerful technique if high spatial resolution and a large energy range are needed for the data acquisition; otherwise, spectroscopic ellipsometry is a suitable technique for extracting the optoelectronic properties of a sample.

Chapter 3. Standard EELS Spectra of P3HT, PCBM, CuPc, and C_{60}

The bulk of the work to be presented in this chapter has been published as articles in peer-reviewed technical journals. These articles can be found in their entirety in references [86] and [87].

3.1. Observation of Electron Beam Damage in Organic Materials

When organic materials, such as polymers, are placed under a high-energy electron beam (as they are during the acquisition of electron energy-loss spectroscopy (EELS) data – see Section 2.2 for an overview of this method), electron beam damage may occur. Although organic materials may be damaged via knock-on displacement, (an elastic scattering process in which the electrons from the incident beam cause atomic nuclei to be displaced [88,89]), the primary cause of electron beam damage for organic materials is radiolysis [88]. During the imaging/spectroscopy of an organic material, the transfer of energy during an inelastic scattering process can excite an electron in the molecule from the valence band to the conduction band [89,90]. When it is a valence electron that is excited to the conduction band, an electron-hole pair will be generated in the sample, and the electron (now a secondary electron) from this electron-hole pair can travel through the sample and form other electron-hole pairs (other secondary electrons) [90]. These

secondary electrons can then, in turn, cause changes in the interatomic bonding of the sample [90], which may result in broken bonds, both in the polymer backbone or between the backbone and the side groups [38,89]. These broken bonds change the structure (local chemistry) of the polymer, which may affect the optoelectronic properties measured in EELS. In fact, EELS is commonly used to monitor this electron beam damage, as the loss of fine structure in the measured spectrum is indicative of structural changes affecting the electronic configuration of the molecules [88,89,91].

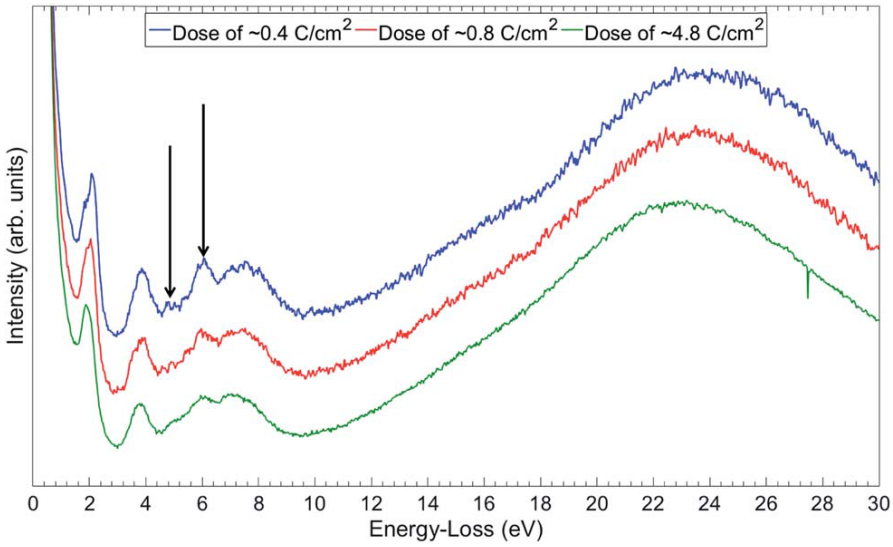

Figure 3.1: Low-loss EELS spectra collected for thin films of CuPc. During each acquisition, the electron dose incident on the sample was increased (as shown in the legend). As the electron dose increased, peaks in the CuPc low-loss spectrum lost intensity (see the arrows). This loss of intensity is indicative of changes in the local chemistry of the CuPc sample. This figure has been published in reference [86].

An example of the observation of such damage in EELS spectra is shown in Figure 3.1 for a pure film of copper phthalocyanine (CuPc). As the electron dose incident upon the specimen increases from approximately 0.4 C/cm^2 (blue line) to approximately 0.8 C/cm^2 (red line) to approximately 4.8 C/cm^2 (green line), some of the peaks in the spectra (denoted by the arrows) change in their position and intensity. As mentioned before, this change in fine structure is due to changes in the local chemistry induced by the electron beam. These changes could have a serious impact on the accuracy of the optoelectronic properties extracted from low-loss EELS data, and, as P3HT and PCBM are also organic materials, it was suspected that they would be highly susceptible to electron beam-damage as well. Thus, the first goal for the collection of low-loss EELS data for P3HT and PCBM was to ensure that the beam-damage incurred by the samples could be minimized during the acquisition of the EELS spectra.

3.2. Acquisition of Reliable Low-Loss EELS Data

In order to acquire accurate electronic structure information at the P3HT/PCBM interface of an OPV device, it was necessary to develop a method in which reliable EELS data could be collected for electron beam-sensitive materials (such as those used in OPVs). The validity of such a damage-minimization EELS acquisition method could be verified by comparing the optoelectronic properties of these materials measured by EELS with those measured by variable-angle spectroscopic ellipsometry (VASE, see Section 2.3. for an overview of this method), the latter of which utilizes a light source as the

probe (which should not damage these materials during data acquisitions). To do this, thin films of different organic materials were prepared, from which the optoelectronic properties were determined via VASE and EELS. If the results from the EELS measurements agree with the results from the VASE measurements, then this damage-minimization EELS acquisition method can be trusted to collect reliable low-loss EELS data for electron beam-sensitive materials such as P3HT and PCBM.

3.2.1. Sample Preparation

In addition to P3HT and PCBM, two other organic materials – copper phthalocyanine (CuPc) and C_{60} – were selected for the development of a reliable low-dose EELS acquisition method for organic materials. CuPc and C_{60} were selected because they are more robust under the electron beam than both P3HT and PCBM due to their lack of side chains (Figure 3.2) and are also used in OPVs [92].

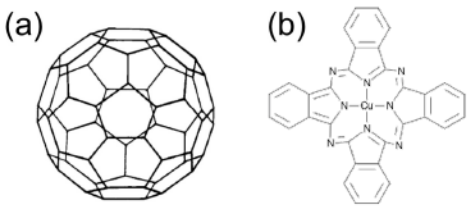

Figure 3.2: Diagrams of (a) C_{60} and (b) CuPc. Part (a) of this figure was originally published in reference [93].

As direct comparisons were to be made between VASE and EELS measurements, it was necessary that the thin films studied were identical, as any differences in the samples could result in differences in the measured optoelectronic properties. One method for preparing thin films of P3HT and PCBM is to spin-coat the thin film onto a PEDOT:PSS-coated substrate, from which the films can be gathered by floating the PEDOT:PSS and thin film off of the substrate in deionized water and allowing the PEDOT:PSS layer to dissolve [30]. However, there were concerns that this method of preparation could cause sample contamination of the P3HT and PCBM thin films if, for instance, the PEDOT:PSS layer had not completely dissolved into the deionized water. This possible contamination could have adverse effects on the quality and reliability of the EELS data collected, and so, instead, thin films of CuPc, C_{60}, and PCBM were deposited onto freshly cleaved, room temperature, (100)-oriented rock salt substrates (NaCl for C_{60} [94–96], KCl for CuPc [97] and PCBM) via thermal evaporation utilizing a deposition chamber situated within an argon-filled glove box. Thin films were also deposited onto glass slides for the purpose of measuring the thicknesses of the films. The conditions utilized during the preparation of these films are listed in Table 3.1 (the deposition temperature for PCBM is not listed because it was deposited using a resistive heater running at 0.8 – 1.6 Amps) .

Table 3.1: Growth conditions used for the deposition of CuPc, C_{60}, and PCBM thin films via thermal evaporation. Parts of this table have been published in reference [86].

Material	Average Chamber Pressure (torr)	Average Growth Rate (nm/min)	Deposition Temperature (°C)
CuPc	3.0×10^{-7}	1.7	210
C_{60}	6.0×10^{-7}	0.6	230
PCBM	4.5×10^{-6}	0.5	N/A

Although it has been shown in the literature that it is possible to deposit thin films of P3HT via thermal evaporation [98,99], attempts to deposit P3HT using this method were unsuccessful. Thus, thin films of P3HT were prepared not by thermal evaporation but via spin-coating a solution of P3HT in dichlorobenzene (10 mg of P3HT in 1 mL of dichlorobenzene) onto room temperature (100)-oriented KCl substrates (for EELS) and glass slides (for VASE). Atomic force microscopy (AFM) was used to measure the thicknesses of the CuPc, C_{60}, P3HT, and PCBM films that had been deposited onto glass slides. These measurements confirmed that all of the films were less than 50 nm in thickness, which means that they should be electron transparent and plural scattering during the EELS measurements (Section 2.2.1.2) should be reduced. UV-Vis absorption measurements (Figure 3.3) also confirmed that these films compare favorably with other of CuPc [100], C_{60} [101], P3HT [30], and PCBM [102] thin films reported in the literature.

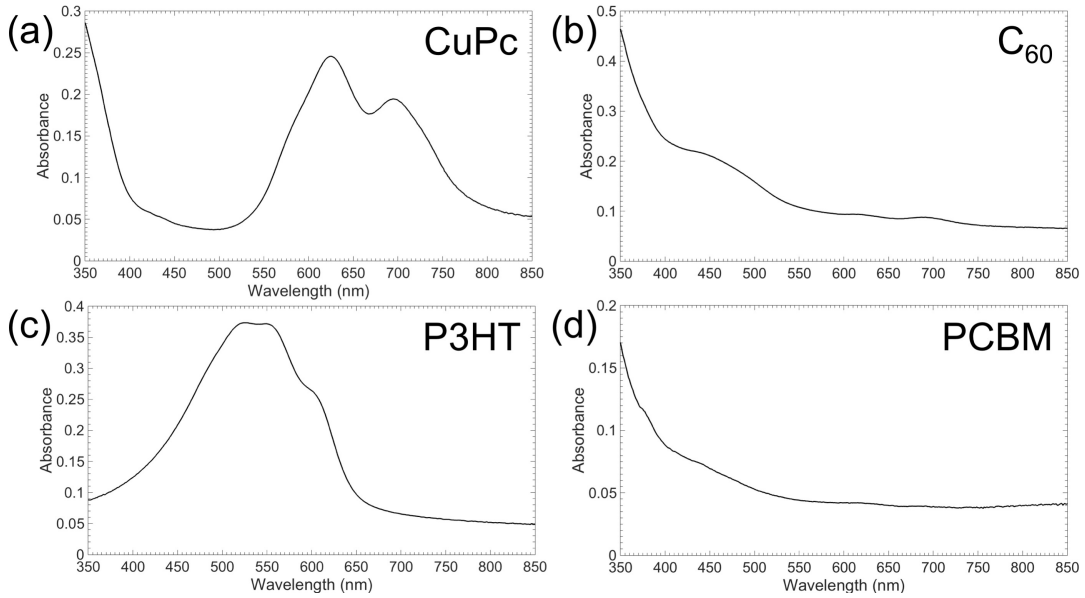

Figure 3.3: Absorbance spectra, obtained via UV-Vis spectroscopy, for (a) CuPc, (b) C_{60}, (c) P3HT, and (d) PCBM. These spectra agree reasonably well with data found in the literature [30,100–102].

3.2.2. Determination of the Complex Dielectric Function via VASE

Variable-angle spectroscopic ellipsometry (VASE) measurements were conducted using the thin films as prepared on the rock salt (CuPc, C_{60}, PCBM) or glass slide (P3HT) substrates. An overview of this technique is provided in Section 2.3. For these measurements, a J.A. Woolam Variable Angle Spectroscopic Ellipsometer was used, and values of psi, Ψ, and delta, Δ, were collected for incident angles of 60°, 65°, and 70°, over the energy range of 0.5-4.5 eV (acquired in 0.01 eV steps), as shown in Figure 3.4. A model consisting of generalized oscillators was then built and fitted to the experimental data via mean-squared error minimization. These models (Figure 3.4, red lines) match the experimental data fairly well, suggesting that the extracted values of the energy-

dependent refractive index, *n(E)*, and energy-dependent extinction coefficient, *k(E)*, should be accurate.

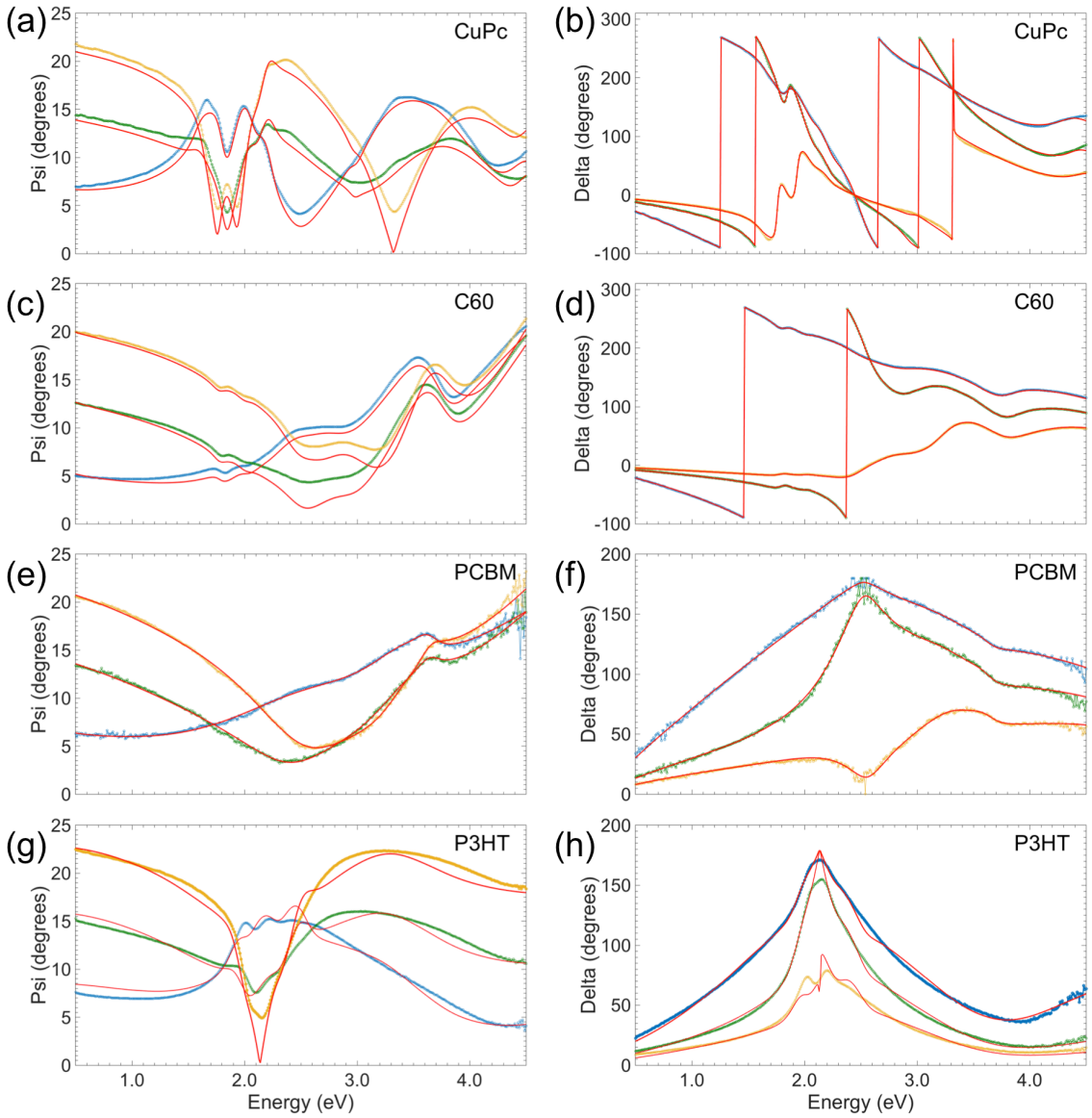

Figure 3.4: Shown in this figure are the experimental psi, Ψ, and delta, Δ, data collected for (a and b) CuPc, (c and d) C_{60}, (e and f) PCBM, and (g and h) P3HT via VASE measurements. These data were collected at various incident angles (blue = 60°, green = 65°, and yellow = 70°). Also shown are the results of the models (red), which match the experimental data fairly well. This figure has been published in reference [86].

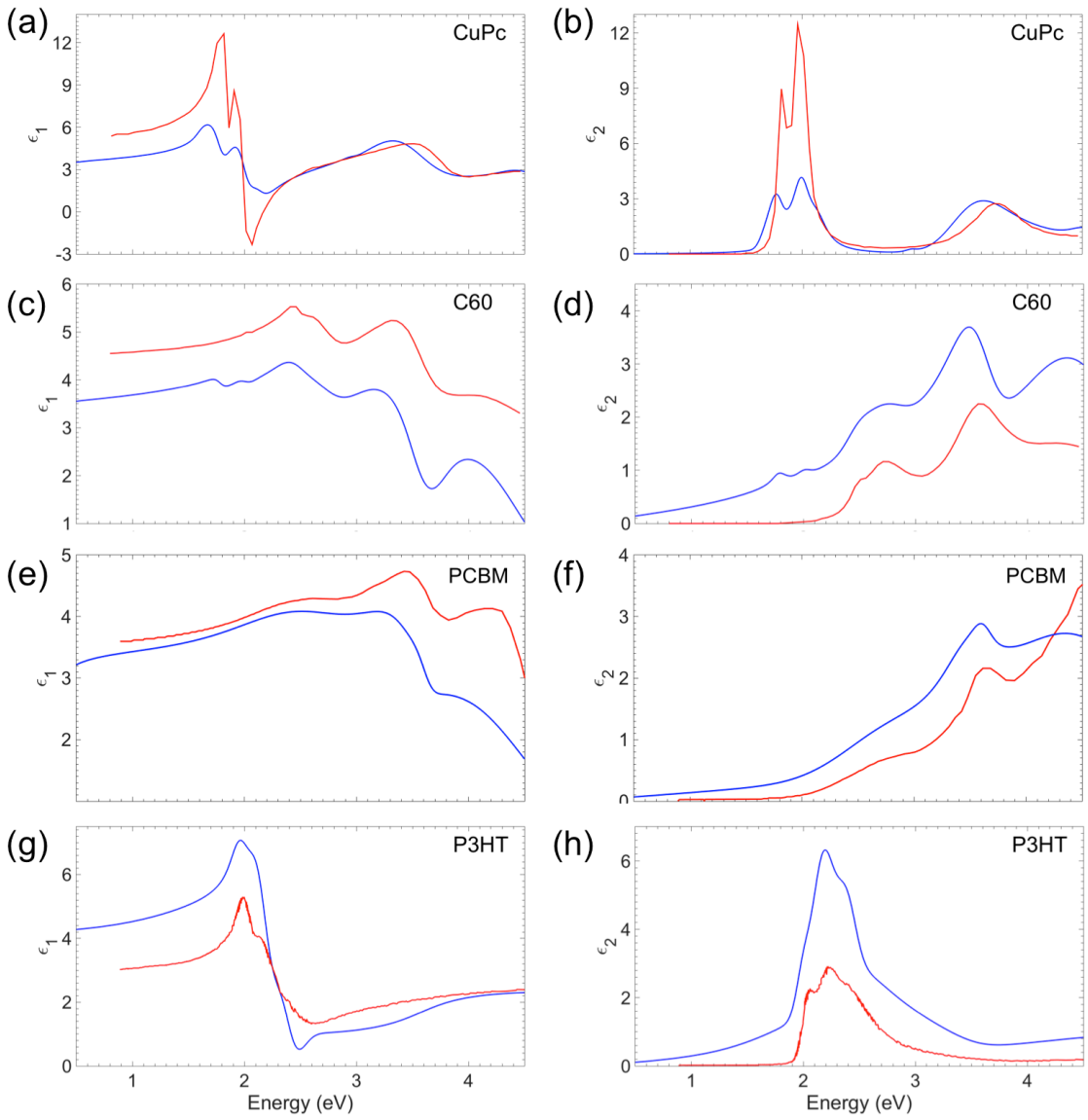

Figure 3.5: Using equations 3 and 4, the real (left column, ε_1) and imaginary (right column, ε_2) parts of the complex dielectric function were calculated for the data obtained via VASE (shown in blue) for (a and b) CuPc, (c and d) C_{60}, (e and f) PCBM, and (g and h) P3HT. These experimental spectra were compared to ε_1 and ε_2 spectra available in the literature (shown in red) from reference [103] for CuPc and C_{60} and from reference [43] for P3HT and PCBM. These comparisons show that the collected VASE data is consistent with prior measurements. This figure has been published in reference [86].

These values of *n(E)* and *k(E)* were used to calculate the real (ε_1) and imaginary (ε_2) parts of the complex dielectric function using Equations 3 and 4, and the calculated ε_1 and ε_2 spectra obtained from the VASE experiments were compared with the results of other VASE measurements that had been previously reported in the literature (Figure 3.5). For all four materials, the VASE measurements are in fairly good agreement with previously published data [43,103]. Thus, once ε_1 and ε_2 have been obtained via EELS, it should be possible to compare those spectra to the VASE ε_1 and ε_2 spectra shown in Figure 3.5 (blue lines) in order to determine if the CuPc, C_{60}, P3HT, and PCBM thin films have been damaged by the electron beam during the EELS data acquisitions.

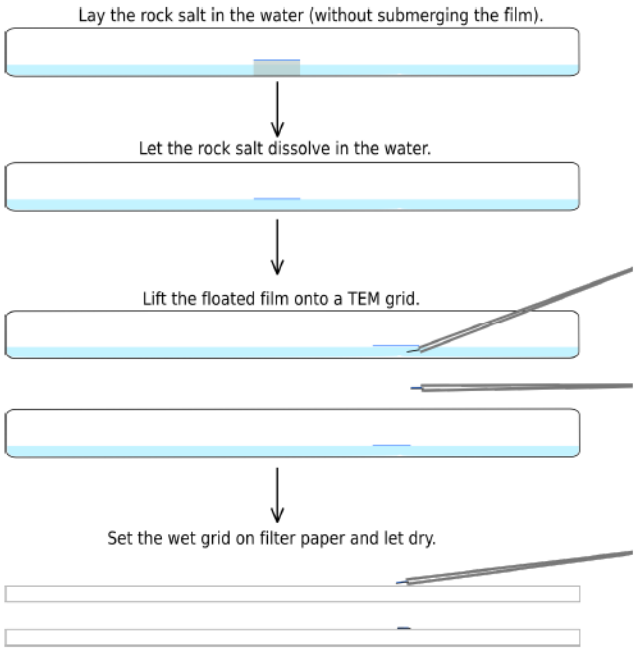

Figure 3.6: Steps taken to float the CuPc, C_{60}, P3HT, and PCBM thin films off of their rock-salt substrates and onto lacey-carbon TEM copper grids.

3.2.3. Development of a Damage-Minimization EELS Acquisition Method

In order to collect EELS data from the thin films, it was first necessary to float the films off of their respective substrates and onto a lacey-carbon TEM copper grid. By placing the thin film/rock salt samples into room temperature distilled water, the rock salt substrates dissolved, leaving behind only the thin films floating on the surface of the distilled water. These thin films were then collected onto separate TEM grids, and the grids were placed onto filter paper overnight in order to dry. This process is outlined in Figure 3.6.

EELS data was collected for these films using a monochromated 60 keV electron beam in an FEI Titan^3 60-300 Image-Corrected S/TEM outfitted with a Gatan Quantum spectrometer. A damage-minimization STEM-EELS method was devised in order to collect reliable data for these electron beam-sensitive materials. First, the microscope and spectrometer were aligned in an area of the TEM grid that did not contain any of the organic thin films. The sample stage was then adjusted until the edge of the organic thin film was visible in the field of view (approximately 1 μm^2 in area). Next, the electron beam was blanked (so that it was no longer incident on the sample), and the sample stage was blindly moved such that the thin film was brought into the field of view. This ensured that the sample had never been exposed to the electron beam before the EELS data acquisition, thus removing all possible electron beam damage prior to the EELS measurement. Once the sample was brought into the field of view, the electron beam was unblanked, and the scanning electron beam was set to raster continuously across the field of view. Immediately after the beam began to raster across the sample, the EELS

acquisition was started. During these EELS acquisitions, a single spectrum was collected at whatever point the rastering beam was at during its continuous scan. Thus, it was important to ensure that the thin films covered the entire field of view. If holes or carbon film were in the field of view, it was possible that the EELS spectrum collected may have coincided with the rastering beam being over the hole or carbon film. In an attempt to further reduce the amount of damage incurred by the samples during the acquisition of one spectrum, short EELS exposure times (2 – 4 ms) were utilized. Since these exposure times were much longer than the dwell times used for the rastering electron beam (which were on the order of a few microseconds), this meant that the EELS spectra collected were from a small region of the sample rather than from a single point. This reduced the beam-damage observed in the EELS data because the exposure of the electron beam was spread over a small area of the sample for each 2 – 4 ms exposure, as opposed to keeping the electron beam stationary at a single point for 2 – 4 ms. However, although the EELS exposure times were longer than the rastering beam's dwell time, they were still relatively short exposure times, which resulted in noisy data. Thus, instead of collecting just one spectrum, multiple EELS spectra were collected and summed together (creating a single stacked spectrum) in order to improve the signal-to-noise ratio (SNR) of the data. For instance, during the first EELS acquisition of a new sample area, ten random spectra were acquired and summed together to form one stacked spectrum. Immediately after the acquisition of the EELS data, the electron beam was blanked, and the entire acquisition process was repeated in order to observe any indications of beam damage in the EELS data. During this second acquisition, ten random spectra were again acquired and

summed together to form one stacked spectrum. After this acquisition, the electron beam was once again blanked and the acquisition settings for one more measurement were prepared. For this third acquisition, one hundred random spectra were acquired and summed together to form one stacked spectrum. The summation of one hundred spectra was chosen because, if there were no signs of observed beam damage, the SNR of this data set would be much improved as compared to the summation of only ten spectra.

This acquisition method resulted in EELS data that was not highly spatially-resolved. However, since the first step in studying these organic materials via EELS was to prove that reliable data could be collected, the spatial resolution was sacrificed in order to simplify the development of the beam-damage minimization acquisition method.

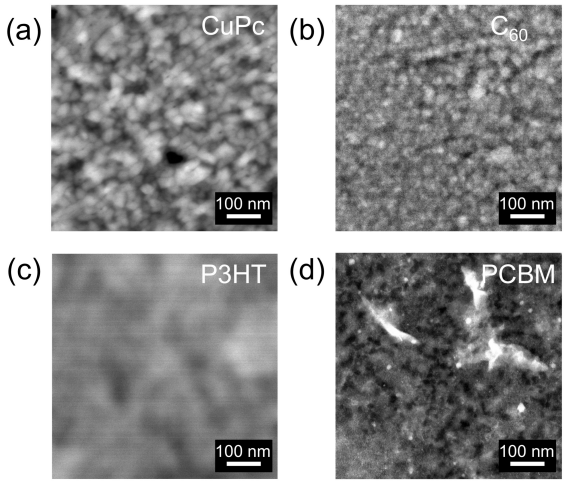

Figure 3.7: HAADF images collected for each of the thin films *after* the EELS acquisitions: (a) CuPc, (b) C_{60}, (c) P3HT, and (d) PCBM. Insets show schematics of these materials. These images were collected using a monochromated 60 keV electron beam. This figure has been published in reference [86].

These data were collected using a convergence angle (α) of 5 mrad, a collection angle (β) of 15 mrad, and for an energy range of -10 to 40 eV (energy dispersion of 0.025 eV/channel). A larger value of β than α was used to ensure that all of the signal from the transmitted electron beam was collected. These conditions resulted in data with measured energy resolutions between 0.16 – 0.23 eV (through sample). Only after all of the EELS data sets were acquired were high-angle annular dark-field (HAADF) images of the films collected (Figure 3.7).

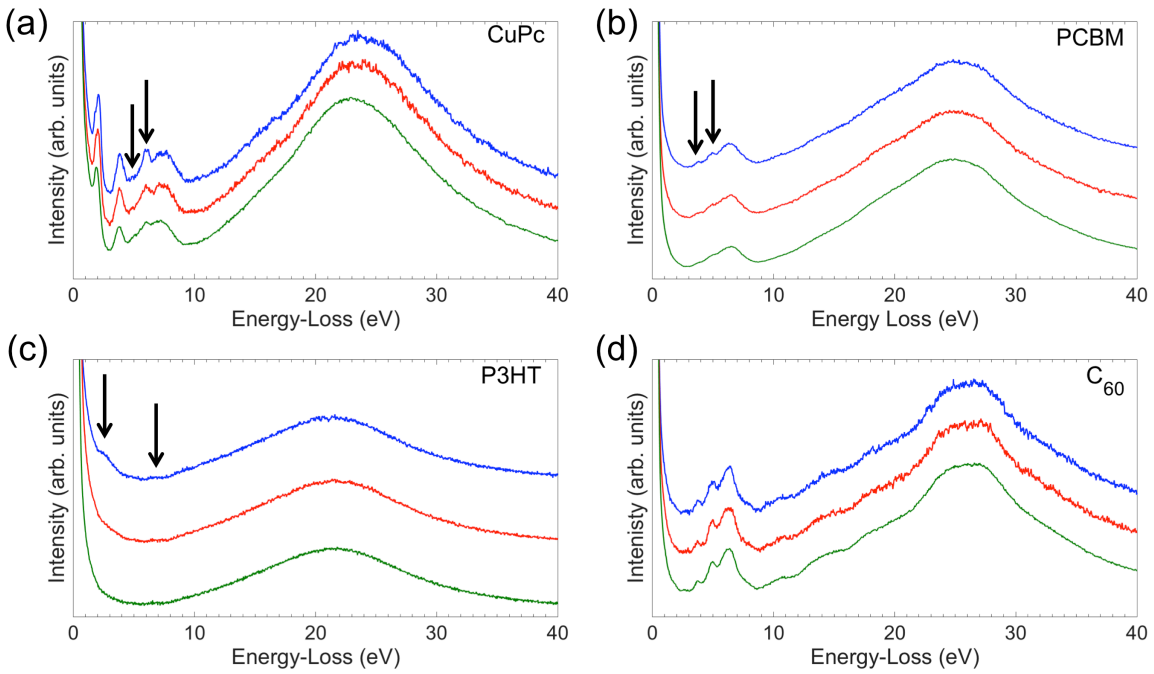

Figure 3.8: Multiple EELS acquisitions for (a) CuPc, (b) PCBM, (c) P3HT, and (d) C_{60}. For all but C_{60}, electron beam damage was detected in the second and third acquired spectra, as the features marked with arrows either disappeared or lost intensity (first acquisition = blue, second acquisition = red, and third acquisition = green).

3.2.4. Determination of the Complex Dielectric Function via EELS

For the extraction of the complex dielectric function, the first acquired spectra (10 summed single spectra – first acquisition) were used for CuPc, P3HT, and PCBM because the second (10 summed spectra – second acquisition) and third (100 summed spectra – third acquisition) serially acquired spectra exhibited signs of electron beam damage (Figure 3.8a-c). However, for C_{60}, there were no indications of electron beam damage in the third acquired spectrum, so it was used for analysis due to its improved SNR (Figure 3.8d).

It is worth noting that the P3HT and PCBM spectra collected during the first acquisitions (shown in blue) appear to be consistent with measurements shown in Figure 1.4a-b (red curves), as originally published in reference [29]. However, since it is possible that the data sets from reference [29] were collected from electron beam-damaged P3HT and PCBM films, it was still necessary to extract the complex dielectric function from these EELS spectra and compare the results to those obtained from the previously described VASE measurements.

In order to process these EELS data, the zero-loss peaks (ZLPs) of each of the four data sets needed to be removed. As discussed in Section 2.2.1.3, ZLPs correspond to elastically scattered electrons that pass through the sample with little-to-no energy-loss; thus, they provide no information concerning the optoelectronic properties of the sample. For these data, the ZLPs were removed using the reflected-tail subtraction routine available in DigitalMicrograph [74]. In this method (see Section 2.2.1.3), the ZLP tails from the energy-gain (left) side of the ZLP are reflected to the energy-loss (right) side of

the ZLP in order to subtract the ZLP intensity from the low-loss spectrum. Since the tails of the ZLPs collected on this STEM extended well beyond 5 eV, the low-loss spectra were collected starting at an energy-loss value of -10 eV to ensure that enough of the energy-gain tails were available to reflect to the energy-loss side of the ZLP. Additionally, the reflected-tail cutoff value (given in multiples of the full-width at quarter-maximum, FWQM) at which the reflected-tail would be spliced with the experimental ZLP was adjusted using the global menu in DigitalMicrograph. This value dictates exactly how much of the energy-gain tails are reflected onto the energy-loss side of the ZLP, and, if an appropriate cutoff value is not selected, it is possible that too much (or, conversely, not enough) signal may be subtracted during the ZLP removal. This could introduce artifacts into the resulting inelastic spectrum, which would then affect the complex dielectric function extracted from the EELS data. An example of the result of the reflected-tail routine is shown in Figure 3.9a for EELS data of C_{60}.

After subtracting the ZLP (elastic scattering signal) from the low-loss spectra, all that remained were signals associated with electrons that had interacted inelastically with the sample. These signals formed inelastic spectra, as shown in Figure 3.9b-e. In all four of the spectra, numerous low-loss peaks are observed, suggesting that the electron beam damage has been minimized during the EELS acquisitions. However, the only way to definitively prove that these spectra are representative of relatively undamaged materials was to extract the real (ε_1) and imaginary (ε_2) parts of the complex dielectric function in order to compare to the previously discussed VASE data. In order to extract the real (ε_1) and imaginary (ε_2) parts of the complex dielectric function, it was first necessary to

obtain the single scattering distribution since, as discussed in Section 2.2.1.2, the single scattering distribution is proportional to $\mathrm{Im}[-1/\varepsilon(E)]$. However, the inelastic spectra are convolutions of both single scattering events and multiple scattering events. Thus, the Fourier-Log deconvolution routine available in DigitalMicrograph was used to obtain the single scattering distribution for these four inelastic spectra.

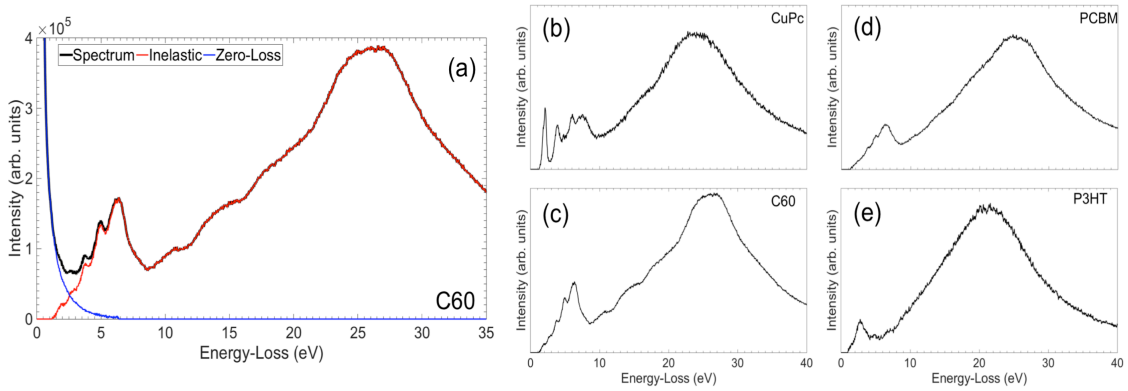

Figure 3.9: Part (a) shows the low-loss EELS spectrum (black) collected for C_{60}. The reflected-tail ZLP subtraction method was used to model the ZLP (blue). Once this ZLP was subtracted, all that remained was the inelastic spectrum (red). Parts (b – e) show the inelastic spectra obtained for (b) CuPc, (c) C_{60}, (d) PCBM, and (e) P3HT. This figure has been published in reference [86].

Once the single scattering distributions had been obtained, Kramers-Kronig analysis (see Section 2.2.1.3) was used to extract the complex dielectric function. In order to run the Kramers-Kronig routine in DigitalMicrograph, the refractive index is required in order to obtain absolute values of the real (ε_1) and imaginary (ε_2) parts of the complex dielectric function [66,74] (see Section 2.2.1.3). Refractive indices of n = 1.9 were

utilized for the Kramers-Kronig analysis of CuPc and PCBM, and refractive indices of n = 2.0 were utilized for the Kramers-Kronig analysis of C_{60} and P3HT.

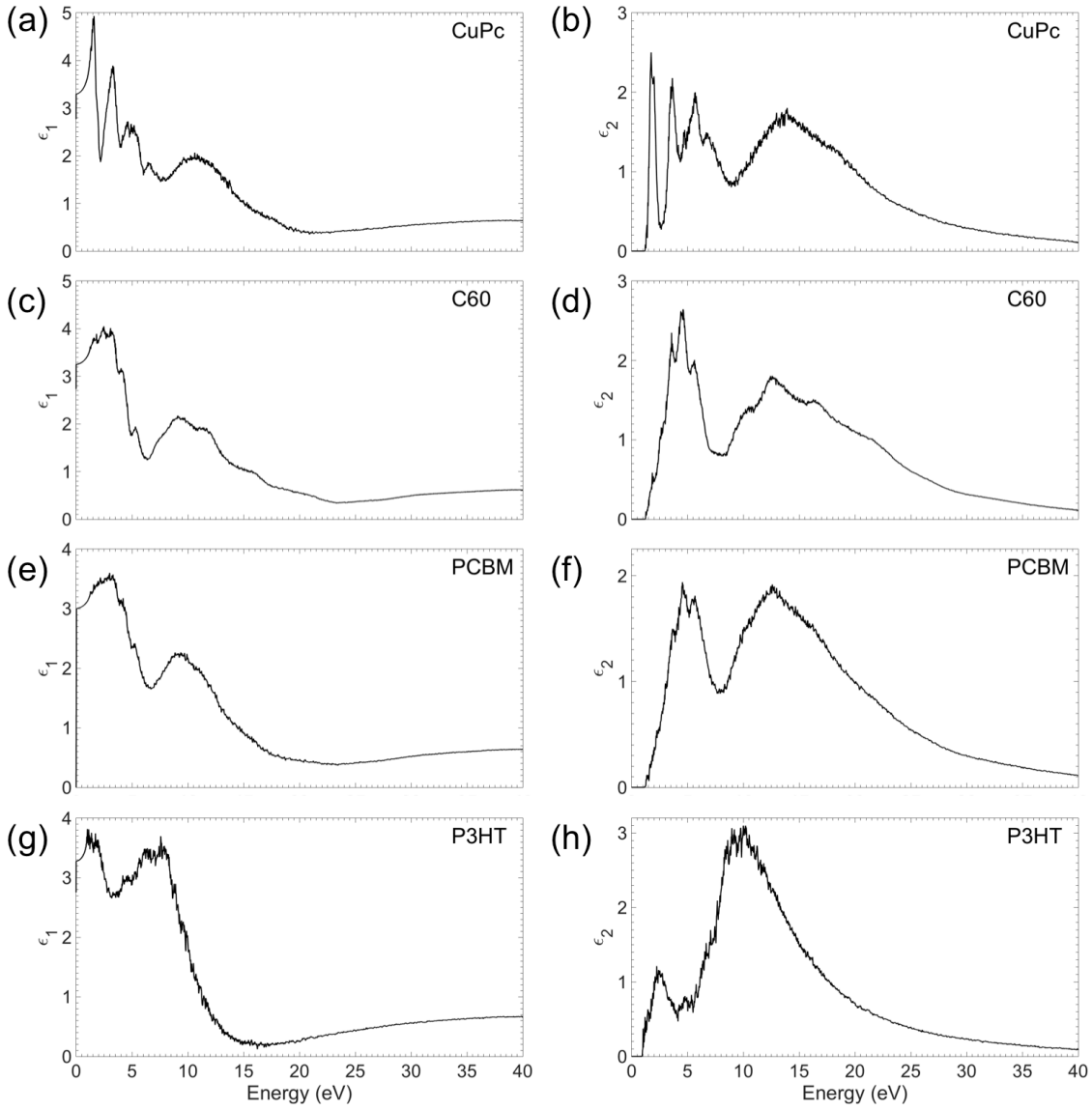

Figure 3.10: Real (left column, ε_1) and imaginary (right column, ε_2) parts of the complex dielectric function extracted from low-loss EELS spectra for CuPc (a and b), C_{60} (c and d), PCBM (e and f), and P3HT (g and h). This figure has been published in reference [86].

The results of the Kramers-Kronig analysis are shown in Figure 3.10 (left column = ε_1, right column = ε_2). In the ε_2 spectra for all four materials, numerous peaks are observed, which, as discussed in Section 2.2.1.3, indicates that many single electron transitions have been measured via these EELS measurements. As it is extremely likely that beam damage would have resulted in the loss of some of these features (demonstrated in Figure 3.11 for CuPc), the observation of numerous peaks further suggests that this EELS acquisition method has minimized the amount of beam-damage incurred by these organic samples.

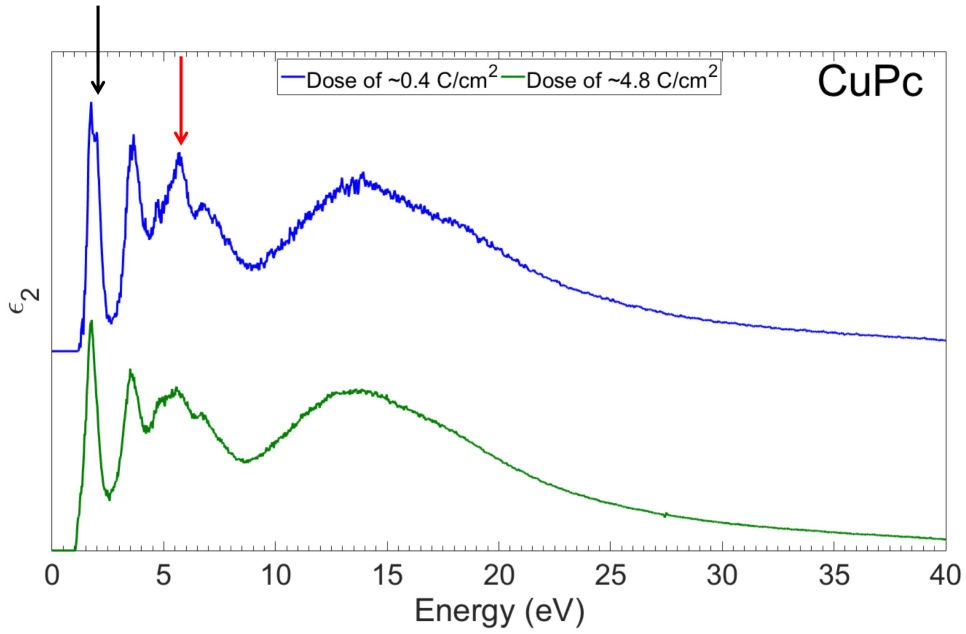

Figure 3.11: As the beam dose increases, features in the CuPc ε_2 spectrum disappear (see black arrow) or lose intensity (red arrow). This is indicative of changes in the electron structure, which are most likely due to changes in the local chemistry arising from electron beam-damage.

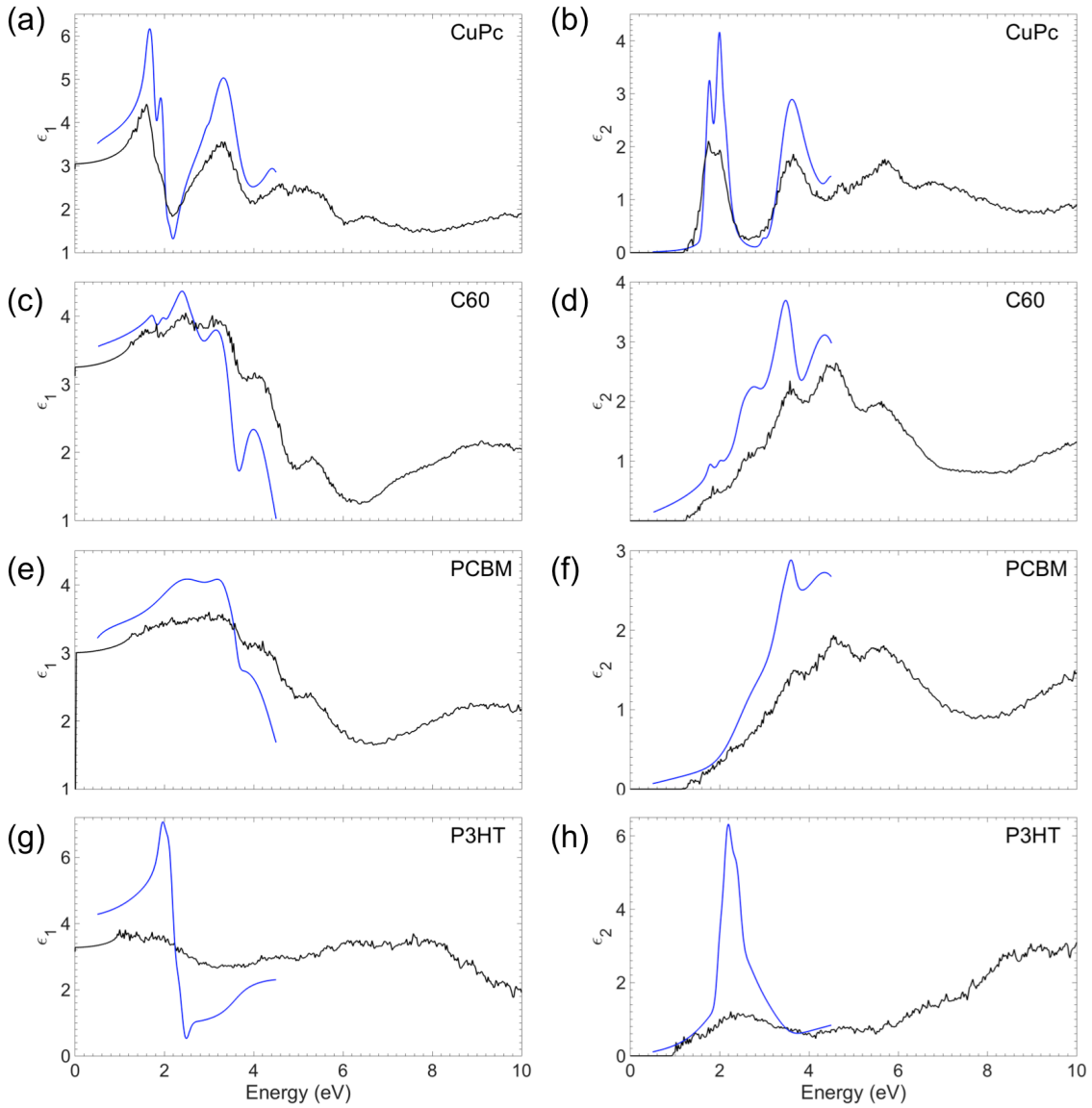

Figure 3.12: Comparisons of the real (left column, ε_1) and imaginary (right column, ε_2) parts of the dielectric function obtained using VASE (blue) and obtained using EELS (black) for CuPc (a and b), C_{60} (c and d), PCBM, (e and f), and P3HT (g and h). The number of peaks and the energies at which these peaks occur agree favorably between the VASE and EELS results. This figure has been published in reference [86].

3.2.5. Comparing the Optoelectronic Properties: VASE and EELS Data

To conclusively prove that the EELS data collected for CuPc, C_{60}, P3HT, and PCBM were representative of materials that had been undamaged by the electron beam, the ε_1 and ε_2 data obtained via VASE and EELS were compared (Figure 3.12). As discussed in the previous section, electron beam damage should result in the absence of peaks in the EELS ε_2 spectra as compared to the VASE ε_2 spectra. However, by comparing the number of peaks observed in each ε_1 and ε_2 spectrum, as well as the energy at which these peaks are observed, the VASE and EELS data sets compare favorably with each other. This confirms both that the beam damage minimization EELS acquisition method developed for studying these organic materials is effective and that the EELS data collected and shown here is reliable.

When comparing the CuPc ε_2 spectra (Figure 3.12b), it is interesting that the two peaks at ~2 eV are reversed in their relative intensities (VASE vs. EELS). As shown in Figure 3.5b, the VASE ε_2 spectrum agreed well with literature data, suggesting that the relative intensities of these two peaks is correct for the VASE data. Thus, it is highly likely that some error was made in the processing of the EELS data. Most likely this error occurred during the ZLP removal from the low-loss spectrum. For the data collected on the FEI Titan^3 60-300 Image-Corrected S/TEM, the tail on the energy-loss side of the ZLP extends well into the right (energy-loss) side of the low-loss spectrum. As shown in the example ZLP collected through vacuum (i.e. not through a sample), using identical conditions as these data (Figure 3.13), the ZLP extends out to ~5 eV. When the ZLP

extraction routine is performed in DigitalMicrograph, the reflected-tail will terminate at the first energy-loss value at which the intensity goes negative on the tail, which is usually due to noise), thus leaving extra intensity in the inelastic spectrum that should have been subtracted by the ZLP extraction routine but was in fact not subtracted. This extra intensity may explain why the first peak in the CuPc ε_2 spectrum of the EELS data is more intense than the second peak, as lower energy-losses would be affected more by the extra intensity left from the ZLP extraction routine. This does not affect this analysis, however, as all of the peaks observed in the VASE data are also observed in the EELS data, confirming that any electron beam damage in the CuPc sample has been minimized. It only suggests that the absolute values of ε_2 obtained for CuPc may not be accurate.

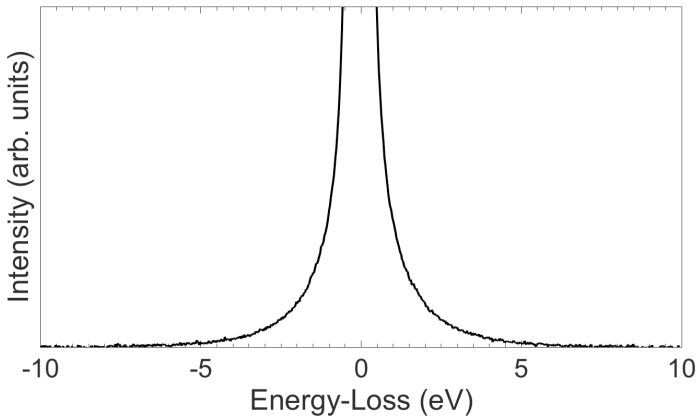

Figure 3.13: Example ZLP collected through vacuum, demonstrating how the tails of the ZLP extend out to approximately 5 eV, which can affect the removal of the ZLP.

Furthermore, it is worth noting that the peaks at approximately 2 eV in the VASE-acquired ε_1 and ε_2 spectra of C_{60} that were absent in the literature data (Figure 3.5c-d) are observed in the EELS-acquired data (Figure 3.12c-d). This suggests that these peaks are real, whereas they may have been dismissed as an artifact from the fitting (VASE) or an artifact from noise (EELS) without the comparisons made here between the two data sets.

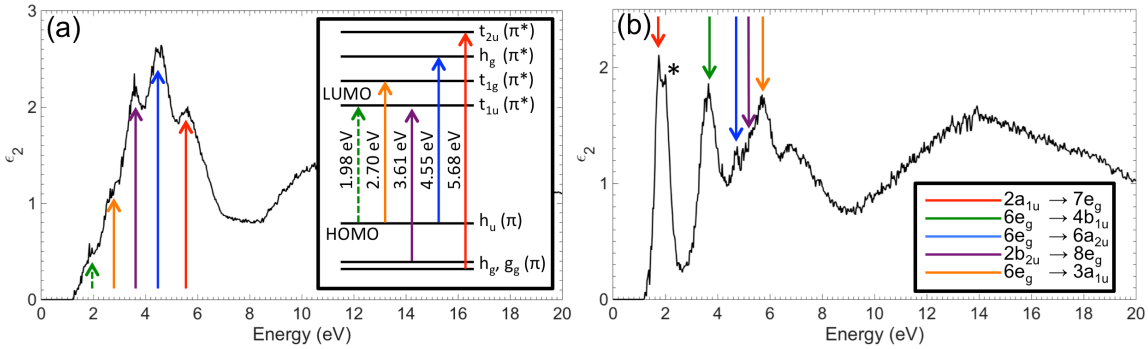

Figure 3.14: Part (a) of this figure identifies which single electron transitions have been measured in the experimental ε_2 spectrum for C_{60} [104,105], whereas part (b) identifies which single electron transitions have been measured in the experimental ε_2 spectrum for CuPc [106,107]. The inset of part (a) was adapted from reference [104]. This figure has been published in reference [86].

3.3. Assignment of Single Electron Transitions

As discussed in Section 2.2.1.3, it is possible to relate ε_2 spectra to known single electron transitions by comparing the energies of the peaks in ε_2 to the energies of the known transitions. Fortunately, such single electron transitions and their energies were

readily available in the literature for both C_{60} and CuPc, which made it possible to identify which transitions were measured during the acquisition of the low-loss EELS data previously shown.

Figure 3.14a shows the correlation of peaks in the experimental EELS ε_2 spectrum to known single electron transitions that were identified for a C_{60} absorption coefficient (α) spectrum by reference [104] and were calculated by references [108,109]. Since it is possible to relate the absorption coefficient to the imaginary part of the complex dielectric function [78], this means that the energies of the peaks measured in this α spectrum should relate closely to the energies of the peaks measured in the ε_2 spectrum obtained from these EELS measurements (this relationship can be mathematically shown proven since $\alpha = 4\pi k/\lambda$ and $\varepsilon_2 = 2nk$). As shown in this figure, it was possible to relate the energies of the known single electron transitions to each of the first five peaks of the C_{60} ε_2 spectrum, and, thus, identify which single electron transitions were observed during these EELS measurements. This includes the symmetry-breaking h_u to t_{1u} transition, the observation of which has been attributed to disorder in C_{60} thin films by reference [104]. Furthermore, it was possible to determine the type of molecular orbital (bonding, π, or anti-bonding, π^*) for each state shown in the inset [105].

Similar comparisons were made for the experimental ε_2 spectrum of CuPc (Figure 3.14b) by comparing known single electron transitions obtained from density functional theory calculations [106] and measured using vapor-phase absorption spectroscopy [107]. Again, all five allowed transitions (the details of which are in Table 3.2) were measured in the experimental ε_2 spectrum (see the colored arrows). In addition to these five

transitions, a vibronic component of the $2a_{1u} \rightarrow 7e_g$ transition [107] was also measured at ~2 eV (denoted by the asterisk).

Table 3.2: Shown are the known CuPc single electron transitions (as adapted from reference [106]). This table has been published in reference [86].

Type	Transition	Theoretical Energy (eV)
$\pi\,(\mathrm{C}) \rightarrow \pi\,(\mathrm{C,N})$	$2a_{1u} \rightarrow 7e_g$	1.589
$\pi\,(\mathrm{C,N_p}), d_\pi \rightarrow \pi\,(\mathrm{C,N_p})$	$6e_g \rightarrow 4b_{1u}$	4.409
$\pi\,(\mathrm{C,N_p}), d_\pi \rightarrow \pi\,(\mathrm{C})$	$6e_g \rightarrow 6a_{2u}$	4.693
$\pi\,(\mathrm{C}) \rightarrow \pi\,(\mathrm{C})$	$2b_{2u} \rightarrow 8e_g$	5.186
$\pi\,(\mathrm{C,N_p}), d_\pi \rightarrow \pi\,(\mathrm{C})$	$6e_g \rightarrow 3a_{1u}$	5.837

Knowing these transitions, and, more specifically, the molecular orbitals that they correspond to means that it should be possible to determine which bonds are changing (if any) at the interface between these two materials. Furthermore, it is possible to determine which bonds are breaking in these materials when the samples begin to exhibit beam-damage. For instance, in the CuPc ε_2 spectra shown in Figure 3.11, as the electron dose is increased, the feature at ~6 eV (denoted by the red arrow) disappears. Based on the single electron transitions shown in Table 3.2, this indicates the breaking of π-bonds for transitions from $6e_g \rightarrow 3a_{1u}$. However, as shown in Figure 3.11, an electron dose of ~4.8 C/cm^2 has not resulted in all of these bonds breaking, as there is still some measurable

intensity at ~6 eV, suggesting that some of these $6e_g \rightarrow 3a_{1u}$ transitions are still occurring. The same cannot be said for the feature at ~2 eV. This vibronic component of the $2a_{1u} \rightarrow 7e_g$ transition has completely disappeared after the sample has been exposed to ~4.8 C/cm^2. This proves that, when CuPc is exposed to this high of an electron dose, all of the π-bonds arising from the vibronic components of the $2a_{1u} \rightarrow 7e_g$ transition have been broken.

Unfortunately, known single electron transitions for both P3HT and PCBM were not available in the literature, and, thus, it was not possible to identify the single electron transitions observed in their ε_2 spectra or determine which bonds were breaking as a result of electron beam damage. However, if these transitions are computed in the future, it should be relatively simple to compare these experimental ε_2 spectra to those known transitions.

3.4. Acquisition of Low-Loss Data with Higher Energy Resolution

Having proven that reliable EELS data could be collected for CuPc, C_{60}, P3HT, and PCBM, identical measurements were conducted using a Nion UltraSTEM 100 MC 'HERMES' S/TEM with higher energy resolution capabilities than that of the FEI Titan^3 60-300 Image-Corrected S/TEM used in the acquisition of the EELS data previously discussed.

3.4.1. Monochromators: An Overview

As discussed in Section 2.2, in order to measure EELS spectra with the best energy resolutions, monochromators are used. This is because, without a monochromator, the energy resolution of EELS spectra is restricted by the inherent energy spread of the electron beam from the electron gun [67,68]. The type of monochromator installed in a STEM has a large effect on the highest achievable energy resolution possible in EELS measurements. The FEI Titan^3 60-300 Image-Corrected S/TEM (hereafter referred to as 'Titan') used in the collection of all of the EELS discussed thus far utilizes a Wien filter for monochromating the electron beam. This monochromator, designed by Tiemeijer, is a double-focusing Wien filter that is placed behind the field emission electron gun [68], and the details of this monochromator can be found in reference [67]. Essentially, the electron beam is kept at a low voltage (less than 5 keV), passed through the Wien filter during which it is dispersed and then accelerated to the operating voltage of the microscope [68,70]. After acceleration, an energy-selecting slit is used to filter out electrons based on their dispersion [69,110]. For 20 keV electron beams, this monochromator design has been shown to result in an energy resolution of 0.1 eV, which is much improved from the 0.5 – 0.7 eV inherent spread of the field emission electron gun [67,68]. This is consistent with the experiments discussed so far (which were made using a 60 keV electron beam and resulted in measured energy resolutions of about 0.15 eV through vacuum with a dispersion of 0.025 eV/channel), since the energy resolution for EELS spectra worsens with increasing accelerating voltage due to the increase in the energy spread of the electron beam [38].

The Nion UltraSTEM 100 MC 'HERMES' S/TEM (hereafter referred to as 'Nion'), however, utilizes a magnetic monochromator, known as an alpha filter due to the trajectory of the electrons through the filter, which is described in detail in references [69] and [111]. The primary difference between the alpha filter and the Wien filter is that the electrons are dispersed at their final voltage (i.e. 60 keV for these measurements) rather than at a lower accelerating voltage as in the Wien filter design used in the FEI microscopes [69]. Furthermore, the monochromator and spectrometer are linked to the high tension, which means any instabilities in the high tension (electron beam) as it passes through the monochromator are tracked by the spectrometer [69,111]. This improves the energy resolution of the EELS data as energy shifts due to instabilities of the high tension source are eliminated [69]. Using this type of monochromator, energy resolutions of 9 meV for a 60 keV electron beam are attainable, which makes it possible to measure vibrational features in the extreme low-loss region of an EELS spectrum [71]. It is worth noting that these improved energy resolutions were observed for an electron beam with a higher accelerating voltage than the one reported by Tiemeijer for his monochromator (0.1 eV for 20 keV electron beam [67]). This improved monochromator design means that vibrational spectroscopy measurements could be made with relatively high spatial resolution, which would make EELS an even more powerful analytical technique.

Having obtained access to a Nion STEM with this type of monochromator, the low-loss EELS measurements previously discussed (made on the Titan STEM) were repeated to see if any more electronic information could be gleaned from these four organic

materials (CuPc, C_{60}, P3HT, and PCBM) due to the improved energy resolution achievable in this microscope.

3.4.2. Experimental Methods

The samples of CuPc, C_{60}, P3HT, and PCBM used in the acquisition of the Nion EELS data were identical to those used in the collection of EELS data on the Titan microscope. Again, a 60 keV monochromated electron beam was used in combination with the damage-minimization acquisition method described in Section 3.2. The data were collected in dual-EELS mode with a convergence semi-angle (α) of 34 mrad and a collection semi-angle (β) of 44 mrad. In dual-EELS mode, two EELS spectra are consecutively collected (i.e. one after the other) during each acquisition. These two spectra can be set to collect over different energy-loss ranges, which is why dual-EELS mode is commonly used to acquire both low-loss and core-loss EELS spectra at the same time. However, for these experiments, dual-EELS mode was used to avoid oversaturation of the detector. If the maximum intensity of the ZLP is too large, the detector will become oversaturated, which will cause distortions in the collected low-loss spectra. These distortions then make it impossible to subtract the ZLP from the low-loss spectra, thus rendering the data set useless.

In order to ensure that the detector did not oversaturate, a short acquisition time (5 ms) had to be used. However, such a short acquisition time resulted in low-loss spectra with poor signal-to-noise ratios (SNRs). Thus, dual-EELS mode was used to acquire one spectrum that encompassed the ZLP (5 ms acquisition time, energy-loss range of -1 to 9

eV, energy dispersion = 0.005 eV/channel) and one spectrum that avoided the maximum intensity of the ZLP (100 – 300 ms acquisition times, energy-loss range of 0.05 – 10 eV, energy dispersion = 0.005 eV/channel). By setting the start energy-loss of the second spectrum to 0.05 eV, the acquisition times used to collect the low-loss spectra could be increased as the maximum of the ZLP (at 0 eV) was no longer acquired in these spectra.

In order to measure these EELS spectra with the highest energy resolution (35 meV) possible for these acquisition conditions, it was necessary to use an energy dispersion of 0.005 eV/channel, which meant that it was only possible to collect low-loss EELS data for energy-losses up to 10 eV. As discussed in Section 2.2.1.2, it is necessary to remove plural scattering from inelastic spectra in order to use Kramers-Kronig analysis to extract the complex dielectric function. However, to perform a deconvolution of an inelastic spectrum, it is necessary that the spectrum extends beyond the plasmon peak so as to avoid the introduction of artifacts into the experimental data [66]. Thus, single EELS spectra were also collected for the energy-loss range of -5 to 35 eV (energy dispersion = 0.002 eV/channel, energy resolution = 60 meV). This ensured that a low-loss spectrum encompassing the plasmon peak (and beyond) was acquired for these samples.

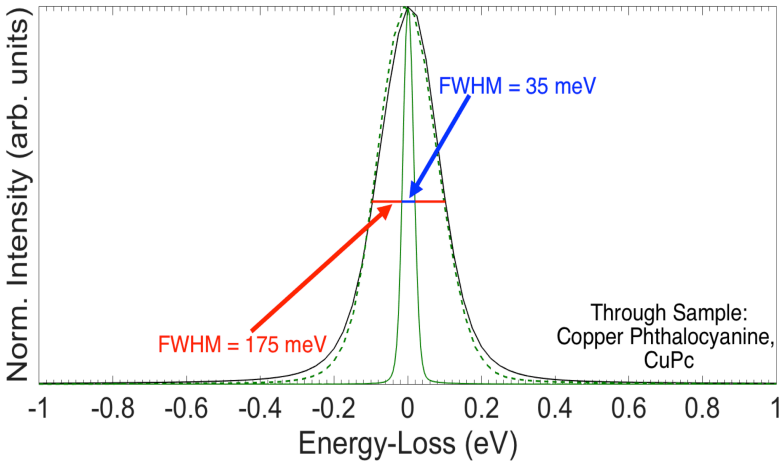

	FEI Titan³	Nion UltraSTEM	FEI Titan³/ Nion UltraSTEM	Normalized
FWHM	175 meV	35 meV	5.00	1
FWQM	275 meV	50 meV	5.50	1.1
FWTM	375 meV	65 meV	5.77	1.154

Figure 3.15: Normalize ZLPs collected from the Titan (solid black) and the Nion (sold green) STEMs for electron beams transmitted through a CuPc thin film are shown. By adjusting the Nion ZLP (solid green) to the same energy resolution of the Titan ZLP (175 meV), the ZLP shown in the dashed green line was obtained. The values of the full-width at half-maximum (FWHM), the full-width at quarter-maximum (FWQM), and the full-width at tenth-maximum (FWTM) were also measured for the experimentally acquired ZLPs. This figure has been published in reference [87].

3.4.3. Analysis of the Zero-Loss Peaks

Before comparing the low-loss EELS data collected on the Nion to that collected on the Titan (from Chapter 3), the zero-loss peaks (ZLPs) acquired from passing through the CuPc thin film sample were compared, as shown in Figure 3.15. The experimental ZLP acquired from the Titan data (energy resolution = 175 meV) is shown in black, and the experimental ZLP acquired from the Nion data (energy resolution = 35 meV) is shown in green. In first comparing these two ZLPs, it is obvious that the improved energy

resolution of the Nion ZLP should simplify the acquisition and analysis of low-loss features that are less than 1 eV in energy-loss (such as vibrational peaks, as demonstrated by reference [71]. Secondly, the tails of the Nion ZLP do not extend as far into the energy-loss side of the low-loss spectrum as they do for the Titan ZLP, which should simplify the ZLP subtraction process. Furthermore, it is interesting to note that the shapes of the Nion and Titan ZLPs vary slightly. This is mathematically shown by comparing ratios of the Titan data to the Nion data for the full-width at half-maximum (FWHM), full-width at quarter-maximum (FWQM), and full-width at tenth-maximum (FWTM), as listed in the table in Figure 3.15. These ratios show that there is a 10% increase and 15 % increase in the ZLP tails for the Titan ZLP at the FWQM and FWTM, respectively. This difference is obvious when the Nion ZLP is adjusted so that it has the same energy resolution of the Titan data, as shown by the dashed green line in Figure 3.15.

One possible explanation for this difference in ZLP shape is that the Titan data may have been PSF-limited as those spectra were collected with a smaller energy dispersion (0.025 eV/channel) than the Nion data was (0.005 eV/channel). The PSF refers to the spread of the ZLP due to the detector [38,66]. Ideally, the energy resolution of the spectrum could be set such that the entire ZLP could fit within a single channel of the CCD [38]. However, the ZLP (and, therefore, other spectral features) is broadened beyond this single channel by the detector (for example, as it passes through the scintillator), and ZLP signal is detected on multiple channels of the CCD, even if the energy resolution is such that it signal should only be detected on one channel [38,66]. Thus, it is possible that, at smaller energy dispersions (i.e. 0.1 eV/channel), the energy

resolution of the spectrum can become PSF-limited since the spreading of the ZLP by the detector may be larger than the actual energy resolution of the spectrum.

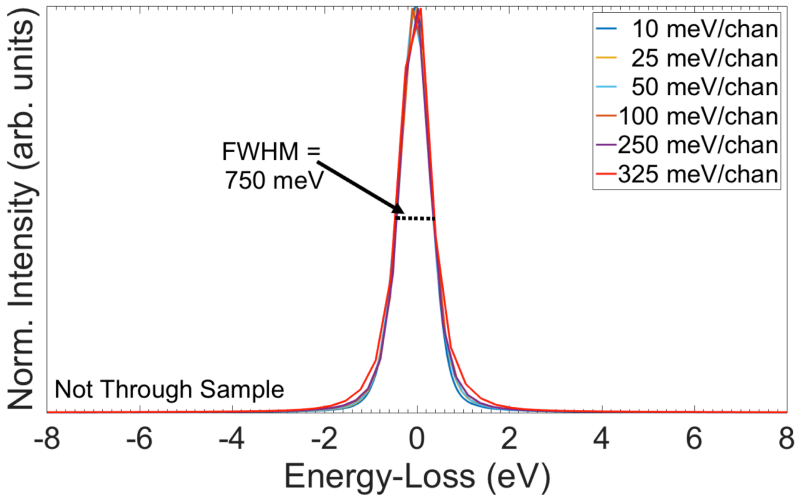

	325 meV/channel	250 meV/channel	100 meV/channel	50 meV/channel	25 meV/channel	10 meV/channel
FWHM (meV)	650	750	300	200	150	150
FWQM (meV)	1300	1000	500	350	250	230
FWTM (meV)	1950	1500	700	450	350	320
FWHM/ FWQM	0.50	0.75	0.60	0.57	0.60	0.65
FWHM/ FWTM	0.33	0.50	0.43	0.44	0.43	0.47

Figure 3.16: Normalized ZLPs collected for different energy dispersions from the Titan STEM for electron beams that did not pass through a sample are shown. These ZLPs have all been adjusted to match the energy resolution for the ZLP with the worst energy resolution (750 meV). This figure has been published in reference [87].

In an effort to determine if the Titan data was PSF-limited, ZLPs with different values of energy dispersion were collected on the Titan STEM for an electron beam with a nominal energy resolution of 150 meV. By adjusting each of these ZLPs until they all had

the same energy resolution (see Figure 3.16), it is clear that, for data collected with energy dispersions of 10 meV/channel, 25 meV/channel (used in the Titan EELS acquisitions), 50 meV/channel, and 100 meV/channel, there is good agreement in the ZLP shape and the ratios of the FWHM/FWQM and FWHM/FWTM. This suggests that the Titan data is not PSF-limited when an energy dispersion of 0.25 eV/channel is used to acquire low-loss spectra.

However, while a clear-cut answer for the difference in these ZLP shapes is not currently available, this analysis does prove that utilizing this Nion STEM results in a ZLP with both a smaller value of FWHM (therefore a higher energy resolution) and a decrease in the residual ZLP signal at the FWQM and FWTM, all of which should improve the quality of the EELS data acquired.

3.4.4. Comparing the Low-Loss Spectra: Titan Data and Nion Data

Before extracting the optoelectronic properties, the low-loss spectra collected on the Titan and on the Nion were compared to see if the enhanced energy resolution of the Nion revealed any new features (Figure 3.17). In comparing these spectra, many of the same features are observed in both the Nion (green) and Titan (black) data sets. However, certain features that appeared only as shoulders on the ZLP in the P3HT, PCBM, and C_{60} Titan data are observed as distinct peaks in the Nion data, as pointed out by the red arrows in Figure 3.17b-d. Furthermore, what appeared to only be one broad peak at ~7 eV in the CuPc Titan data is clearly shown to be two distinct peaks in the Nion data (blue

arrows in Figure 3.17a). Nevertheless, although some of the low-loss features are more defined in the Nion data, no new peaks are observed for energy-losses greater than 1 eV.

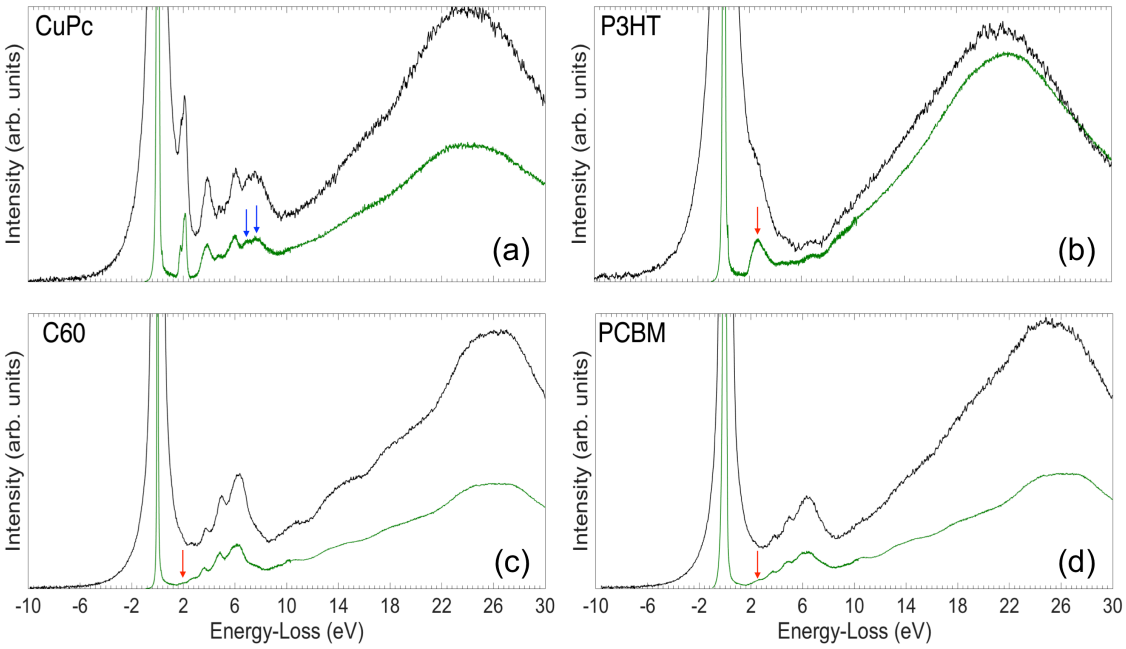

Figure 3.17: The low-loss spectra measured from the Nion STEM (green) and the Titan STEM (black) are compared for (a) CuPc, (b) P3HT, (c) C_{60}, and (d) PCBM. Peaks that are more defined in the Nion data are indicated by red and blue arrows (see the text). This figure has been published in reference [87].

In all four Nion data sets, the intensity of the ZLP tails are essentially zero prior to the onset of the first major peak in the low-loss spectra. Although bandgap analysis was not conducted here, these reduced ZLP tails should make it easier to measure the bandgap for low bandgap materials (assuming the bandgaps are greater than ~1.5 eV). Furthermore,

these reduced tails of the Nion ZLPs should simplify the ZLP subtraction process, as less of the ZLP is actually extending into the collected inelastic spectra.

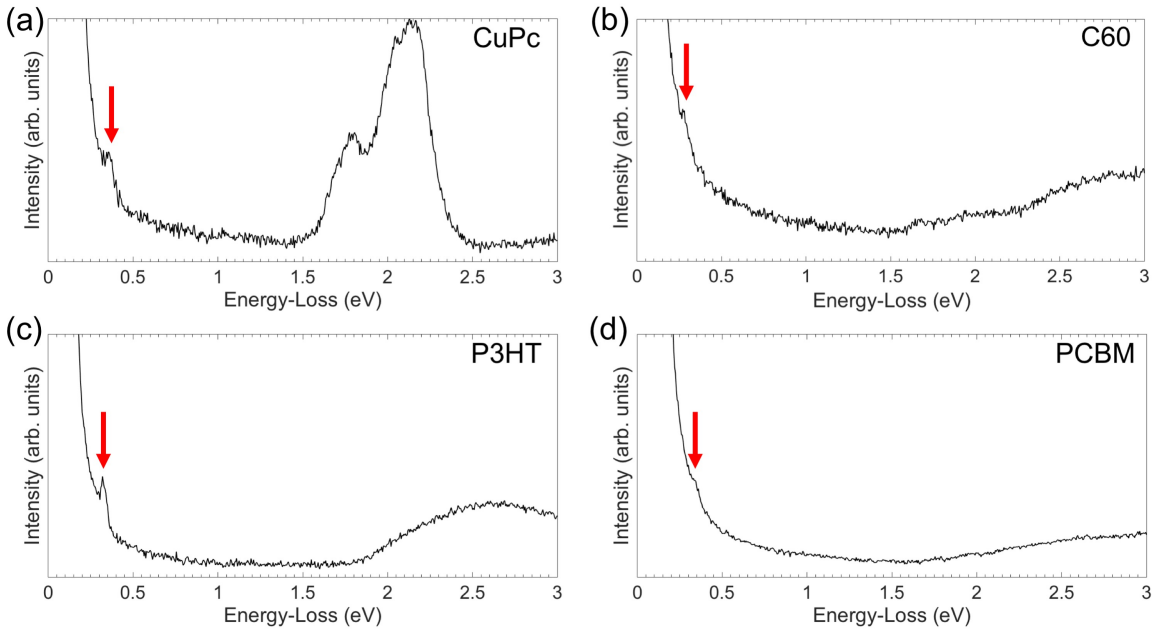

Figure 3.18: Nion (a) CuPc spectrum, (b) C_{60} spectrum, (c) P3HT spectrum, and (d) PCBM spectrum displaying features attributed to O-H and C-H vibrational modes. Part (a) of this figure has been published in reference [87].

Although no new features were observed for energy-losses greater than 1 eV, there is a new feature observed in all four Nion low-loss spectra below 1 eV, as shown in Figure 3.18. These features are most likely O-H or C-H vibrational modes [112] that were obscured by the ZLP in the Titan low-loss spectra.

3.4.5. Comparing Optoelectronic Properties: Titan Data and Nion Data

Though comparisons of the Nion and Titan low-loss spectra (see previous section) suggest that the complex dielectric function obtained for the Nion data should be similar to that obtained for the Titan data, the only way to prove this was to extract the spectra for the real (ε_1) and imaginary (ε_2) parts of the complex dielectric for the Nion data and compare them to the results previously obtained for the Titan data (Figure 3.10). As with all previous analyses, two major processing steps were required before Kramers-Kronig analysis could be used to extract the complex dielectric function: ZLP subtraction (see Section 2.2.1.1) and deconvolution (see Section 2.2.1.2).

Unfortunately, removing the ZLPs from the Nion low-loss spectra proved to be non-trivial. As discussed in Section 3.4.2, it was necessary to use dual-EELS mode to acquire low-loss spectra with high energy resolutions since the exposure times needed to collect spectra with good SNRs caused the ZLP to oversaturate the detector. During these dual-EELS acquisitions, one spectrum collected the ZLP (Figure 3.19a) and the other spectrum collected the low-loss region (0.05 – 10 eV, Figure 3.19b). Since the second spectrum did not collect a full ZLP, it was necessary to splice these two spectra together. However, when these two spectra were spliced together using the splicing tool in DigitalMicrograph, the resulting spectrum (Figure 3.19c) was inappropriate for use of the reflected-tail ZLP subtraction method (as described in Section 2.2.1.1) and attempts to use the reflected-tail method resulted in a poor subtraction of the ZLP (Figure 3.19d).

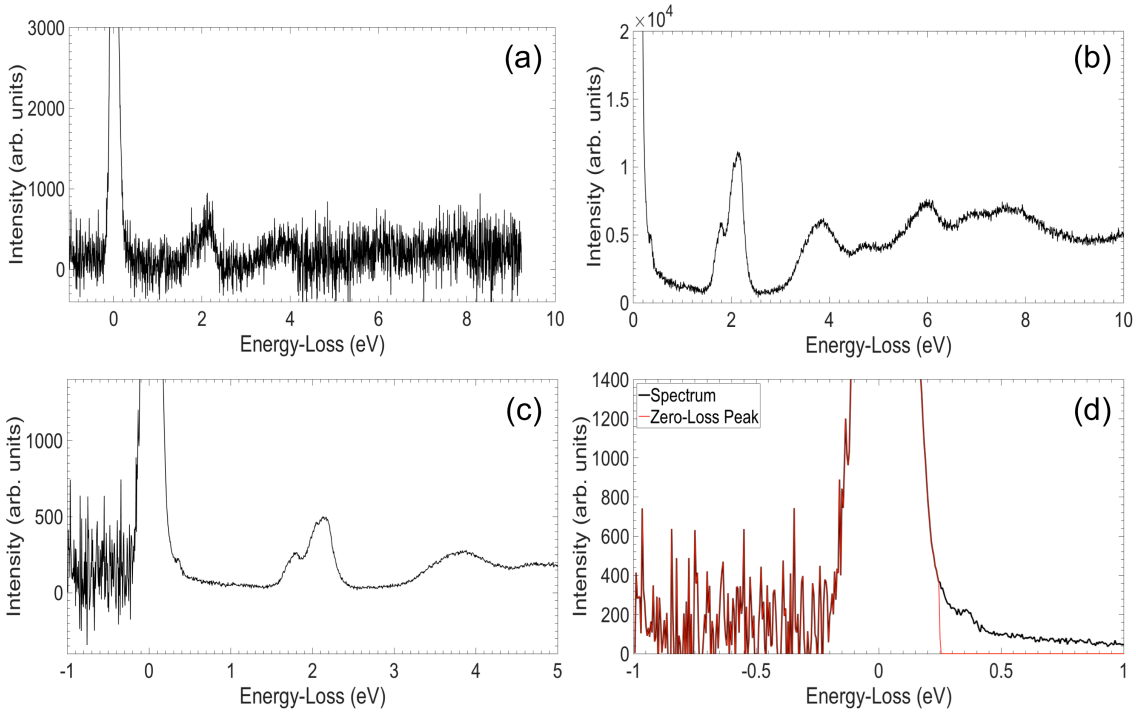

Figure 3.19: The (a) ZLP and (b) high-resolution low-loss spectra collected in dual-EELS mode on the Nion for CuPc. These two spectra were spliced together, which resulted in the spectrum in (c). Due to the large noise signal on the left side of the ZLP in (c), the ZLP extraction routine did not work properly (d). This figure has been published in reference [87].

Thus, it was necessary to develop a method by which proper subtraction of the ZLP could be ensured. This was accomplished by smoothing out the energy-gain (left) side of the ZLP by replacing the noisy data with a fitted function. Attempts to fit the energy-gain tail with various functions were made, and, ultimately, a modified-Voigt function of the form:

$$f(\Delta E) = \frac{2ab\sqrt{\frac{4\ln(2)}{\pi}}e^{-4\ln(2)*(\Delta E)^2}}{\pi c\,(4(\Delta E)^2+b^2)} \qquad \text{Equation 20}$$

where a, b, and c are fitting coefficients, and ΔE is the energy-gain was proven to provide the best fits of the energy-gain tails. An example of this fit is shown in Figure 3.20a for CuPc, in which the experimental data is shown in black and the fitted function is shown in red. These fits were applied to energy-losses of -1 to -0.06 eV, as attempts to fit this function to values beyond -0.06 eV (i.e. -0.01 eV) resulted in a poorer fit of the energy-gain tail as the function was also trying to adequately fit the body of the ZLP.

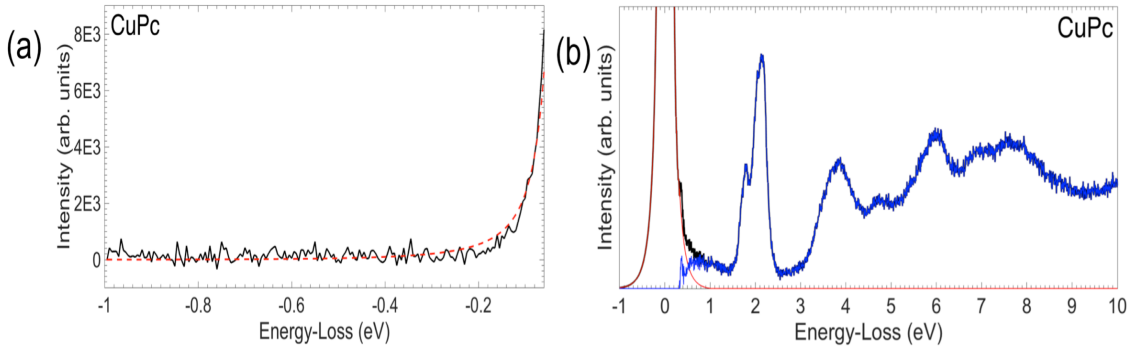

Figure 3.20: (a) The left (energy-gain) tail of the CuPc ZLP (black) was fitted to Equation 20 for the energy range of -1 to 0.06 eV (red dashed line) in order to remove the noise shown in Figure 3.17c. (b) By replacing the noisy energy-gain tail with the smoothed fit, the reflected-tail method was successful in removing the ZLP (red) from the spliced spectrum (black). Once the ZLP was subtracted, only the inelastic spectrum remained (blue). This figure has been published in reference [87].

Once the fitting parameters of the modified-Voigt function were determined, the noisy data from -1 to -0.06 eV was replaced with data calculated using this modified-Voigt function. In other words, the noisy black data in Figure 3.20a was replaced with the smoothed fitted data of the dashed red line. This then allowed for a proper removal of the ZLP via the reflected-tail method, as shown in Figure 3.20b for CuPc. Following the successful removal of the ZLP for the CuPc Nion data, this method was repeated for C_{60}, P3HT, and PCBM, and the ZLPs were correctly subtracted for all three of these Nion data sets.

Having subtracted the ZLPs from the Nion low-loss EELS spectra, the inelastic spectra needed to undergo Fourier-Log deconvolution in order to obtain the single scattering distribution. However, as mentioned in Sections 2.2.1.2 and 3.4.2 in order for the deconvolution routine to work properly, it is necessary that the spectrum extends beyond the plasmon peak so as to avoid the introduction of artifacts into the experimental data [66]. As discussed in Section 3.4.2, an energy dispersion of 0.005 eV/channel was used to acquire the high-resolution ZLP and low-loss spectra (energy resolution = 35 meV). However, the use of this energy dispersion meant that it was only possible to collect low-loss spectra up to 10 eV. Since the plasmon peaks of these materials occur at higher energy-losses (see Figure 3.9b-e), these high-resolution low-loss spectra could not be deconvoluted as-is. Thus, the lower-resolution (60 meV) low-loss spectra collected for energy-losses of -5 to 35 eV (see Section 3.4.2) was spliced to the high-resolution low-loss spectra (which consist of the ZLP with smoothed energy-gain tails and the low-loss

data to 10 eV, such as the spectrum shown in Figure 3.20b) in order to extend the low-loss data beyond the plasmon peak.

Before splicing the two experimental spectra together (high-resolution, -1 to 10 eV, and lower-resolution, -5 to 35 eV), it was first necessary to interpolate the lower-resolution data set so that it had the same energy dispersion as the high-resolution data (0.005 eV/channel). Then, once the lower-resolution data was interpolated, the two spectra were spliced at 10 eV, and the intensity of the lower-resolution data was adjusted so that the splicing was smooth, the results of which are shown in Figure 3.17. These resulting spectra consist of the high-resolution (35 meV) data for energy-losses less than 10 eV, and the lower-resolution (60 meV) data for energy-losses greater than 10 eV.

Finally, once spectra encompassing energy-losses of -1 to 35 eV were obtained, Fourier-Log deconvolution was used to obtain the single scattering distributions. Kramers-Kronig analysis (Section 2.2.1.3) was then performed on these single scattering distributions in order to extract the complex dielectric function for the Nion data via the automated routine available in DigitalMicrograph. The results of this Kramers-Kronig analysis were then compared to the results obtained for the Titan data, as shown in Figures 3.21 (for the real part, ε_1) and 3.22 (for the imaginary part, ε_2).

In comparing the ε_1 spectra obtained from the Nion data (green) to the Titan data (black) in Figure 3.21, it is clear that the two data sets compare quite well. However, the Nion data is better resolved, as would be expected due to the improved energy resolution of this instrument. For instance, in the CuPc ε_1 spectra shown in Figure 3.21a, there is a distinct peak at ~2 eV in the Nion data, whereas only a shoulder is observed in the Titan

data. Similarly, there is better definition between the two peaks from 2 – 4 eV in the Nion PCBM ε_1 spectrum as compared to the Titan PCBM ε_1 spectrum, and in the two features between 4 – 7 eV in the Nion P3HT ε_1 spectrum as compared to the Titan P3HT ε_1 spectrum.

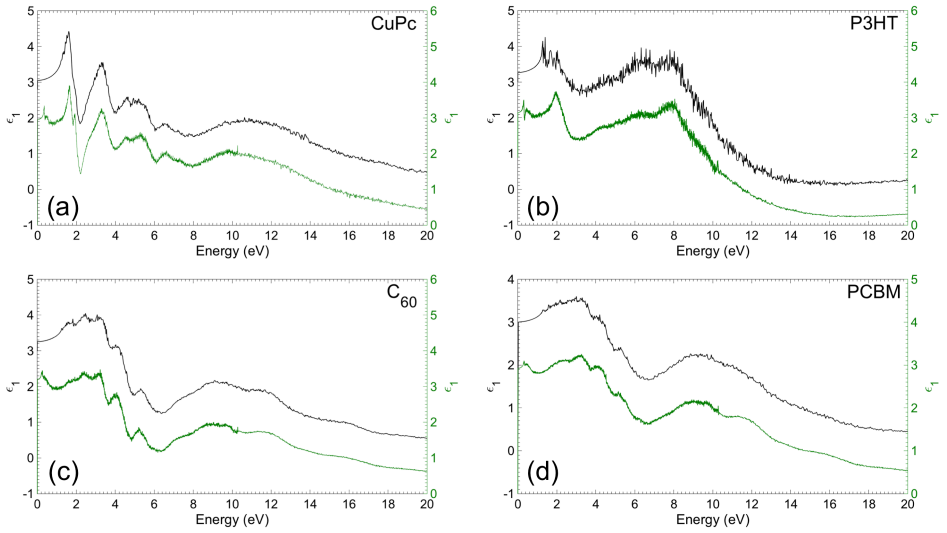

Figure 3.21: The real part (ε_1) of the complex dielectric function extracted from the Nion (green) and Titan (black) data sets for (a) CuPc, (b) P3HT, (c) C_{60}, and (d) PCBM. This figure has been published in reference [87].

In comparing the ε_2 spectra obtained from the Nion data (green) to the Titan data (black) in Figure 3.22, again, the two data sets compare quite well. As discussed in Section 2.2.1.3 and as demonstrated in Section 3.3, peaks in the ε_2 spectra correlate to specific single electron transitions from occupied to unoccupied molecular orbitals. Thus, any new electronic information gleaned from the higher energy resolution data collected

on the Nion should result in the observation of new peaks in the Nion ε_2 spectra as compared to the Titan ε_2 spectra. However, although certain features are better defined in the Nion spectra as compared to the Titan spectra (for instance, in the CuPc ε_2 spectra, the two features between 6 and 8 eV are more clearly separated in the Nion ε_2 spectrum and the peak at ~2.5 eV in the Nion PCBM ε_2 spectrum is more distinct) no new features are observed. This suggests that using an FEI Titan[3] 60-300 Image-Corrected S/TEM should be adequate for collecting all of the optoelectronic information contained in the complex dielectric function of these four materials (assuming an energy resolution of approximately 175 meV). It is worth reiterating that this analysis applies only to these four materials (CuPc, C_{60}, P3HT, and PCBM), and that the improved energy resolution of the Nion may reveal new electronic information for other materials.

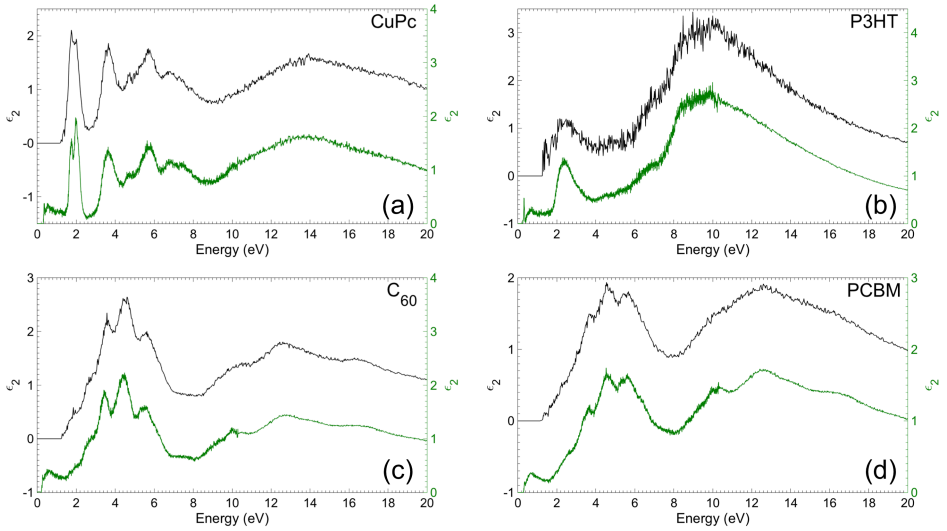

Figure 3.22: The imaginary part (ε_2) of the complex dielectric function extracted from the Nion (green) and the Titan (black) data sets for (a) CuPc, (b) P3HT, (c) C_{60}, and (d) PCBM. This figure has been published in reference [87].

Although no new features are observed in the Nion ε_2 spectra as compared to the Titan ε_2 spectra (Figure 3.22), the relative intensities of the two peaks at ~2eV in the CuPc spectra are reversed. As discussed in Section 3.2.5, the reversal of the relative intensities in the Titan data is likely attributable to an error in the ZLP subtraction due to the extended tails of the Titan ZLP. However, this error has been avoided in the Nion data since the tails of the Nion ZLPs do not extend as far into the acquired inelastic spectra, which should result in more accurate absolute values of ε_1 and ε_2.

3.4.6. Extraction of Absorption Coefficient Spectra

Through algebraic manipulations (see Appendix A), it is possible to relate the absorption coefficient, α, to both the real, ε_1, and imaginary, ε_2, parts of the complex dielectric through:

$$\alpha = \frac{2\pi\varepsilon_2}{\lambda}\left(\sqrt{\frac{\varepsilon_1+\sqrt{(\varepsilon_1)^2+(\varepsilon_2)^2}}{2}}\right)^{-1} \qquad \text{Equation 21}$$

where λ is wavelength. Using this relationship and the extracted energy-dependent ε_1 and ε_2 spectra, the absorption coefficient spectra were extracted from both the Titan and Nion data for all four materials (Figure 3.23). As shown in this figure, the absorption coefficient spectra compare well for all four materials. Furthermore, not only are all of the same peaks observed, but the values of the absorption coefficients are also similar. In

the case of C_{60}, these absorption coefficient spectra are also in fairly good agreement with data available in the literature [104]. Furthermore, the same single electron transitions that were identified in the ε_2 spectra for CuPc and C_{60} (Figure 3.14) are observed in these absorption coefficient spectra. This was expected because, as discussed in Section 3.3 and as shown in Equation 21, α is proportional to ε_2. However, the energies of these peaks are slightly shifted, which is likely due to the fact that α also depends on ε_1.

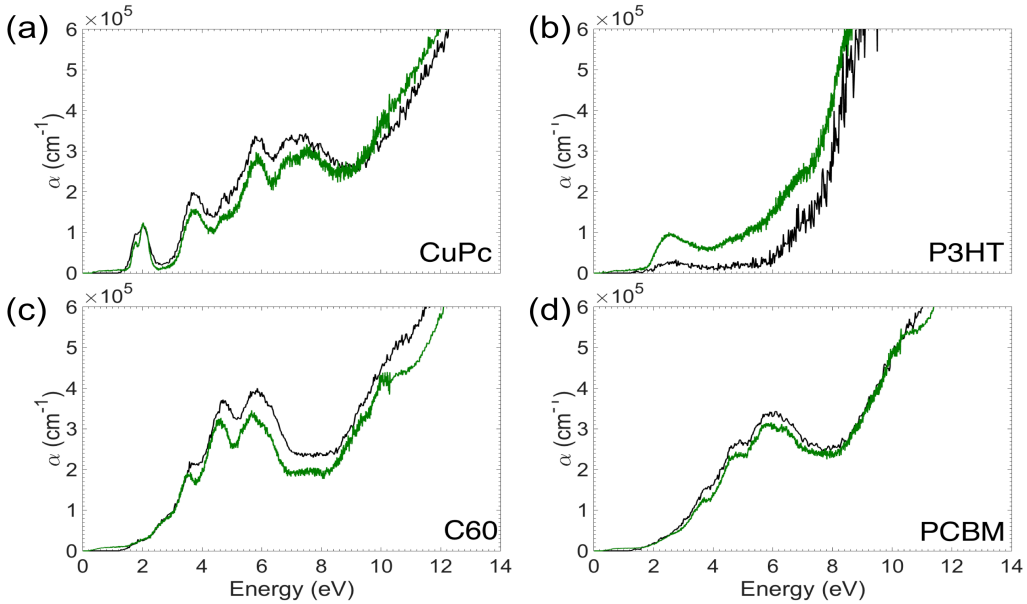

Figure 3.23: The absorption coefficient (α) spectra extracted from the Nion (green) and Titan (black) data sets for (a) CuPc, (b) P3HT, (c) C_{60}, and (d) PCBM. These spectra were obtained by using Equation 21. This figure has been published in reference [87].

This analysis again demonstrates the power of electron energy-loss spectroscopy. By collecting low-loss EELS spectra, it is possible to obtain many optoelectronic properties, such as the complex dielectric function, the energy-dependent absorption coefficient, or

even the complex refractive index, over a much larger energy range than is achievable via spectroscopic ellipsometry or UV-Vis absorption.

3.5 Summary

As discussed in Section 1.1, electron energy-loss spectroscopy (EELS) is the ideal technique with which to measure the electronic structure at the P3HT/PCBM interface of a P3HT:PCBM bulk-heterojunction organic photovoltaic. However, since P3HT and PCBM are electron beam-sensitive materials (as are most organic materials), it was first necessary to prove that reliable EELS data could be collected for these materials. This was accomplished by (1) preparing bulk thin films of P3HT, PCBM, CuPc, and C_{60}, (2) determining the real (ε_1) and imaginary (ε_2) parts of the complex dielectric function by means of variable-angle spectroscopic ellipsometry (VASE), the measurements of which should not damage these samples, (3) developing an optimized EELS acquisition method that minimizes the damage incurred by electron beam-sensitive materials, (4) extracting the real (ε_1) and imaginary (ε_2) parts of the complex dielectric function from these EELS measurements, and (5) comparing the EELS and VASE data to prove that the beam damage was minimized during the EELS measurements. This analysis proved that it *is* possible to collect reliable EELS data for beam-sensitive materials, and these collected EELS spectra can now serve as standards by which to compare future EELS measurements of P3HT, PCBM, CuPc, and C_{60}. Furthermore, it was possible to identify the specific single electron transitions measured in the ε_2 spectra for CuPc and C_{60},

which, to the best of the author's knowledge, was the first time this had been accomplished using EELS.

This beam damage-minimization EELS acquisition method was then used to repeat the EELS experiments with a Nion UltraSTEM 100 MC 'HERMES' S/TEM, which has higher energy resolution capabilities than the FEI Titan^3 60-300 Image-Corrected S/TEM used for all of the previously discussed EELS measurements. The improved energy resolution of the Nion UltraSTEM 100 MC 'HERMES' S/TEM made it possible to observe vibrational features in the extreme low-loss region of the EELS data. However, comparing the FEI Titan^3 60-300 Image-Corrected S/TEM and Nion UltraSTEM 100 MC 'HERMES' S/TEM data at higher energy-losses showed that the lower energy resolution of the FEI Titan^3 60-300 Image-Corrected STEM is more than adequate to obtain all of the optoelectronic information for CuPc, C_{60}, P3HT, and PCBM. This is an important observation, as it suggests that EELS data collected at the donor/acceptor interface of an OPV utilizing an FEI Titan^3 60-300 Image-Corrected S/TEM should reveal all of the pertinent information necessary to understand how the electronic structure at the interface correlates to the performance of the OPV.

Lastly, the energy-dependent absorption coefficients were obtained for CuPc, C_{60}, P3HT, and PCBM, the analysis of which demonstrated how STEM-EELS is an can be used to determine various optoelectronic properties besides the complex dielectric function.

In summary, the work presented in this chapter has proven that it is possible to determine the optoelectronic properties of electron beam-sensitive materials via EELS

measurements. In the next chapter, these methods will be extended so as to prove that spatially-resolved measurements of the optoelectronic information of beam-sensitive materials can also be collected.

Chapter 4. Spatially-Resolved EELS Measurements of OPV Devices

The next logical step, after proving that reliable EELS data could be collected for beam-sensitive organic photovoltaic materials, was to try and collect spatially-resolved EELS data in an actual organic photovoltaic (OPV) device.

4.1. Spatially-Resolved Low-Loss EELS of a CuPc/C_{60} Bilayer Structure

The bulk of the work to be presented in this section has been published in a peer-reviewed technical journal, which can be found in its entirety in reference [86].

Before making spatially-resolved EELS measurements on an actual P3HT:PCBM bulk-heterojunction OPV device, in which the P3HT and PCBM domains are mixed together, preliminary tests were conducted on a simple CuPc/C_{60} bilayer structure in an attempt to prove that it would be possible to collect spatially-resolved EELS data for electron beam-sensitive materials. By using this simpler bilayer construction, it was possible to know exactly which material was being probed by the electron beam and where exactly the interface between the two materials was located, which made these measurements considerably easier than if a P3HT:PCBM bulk-heterojunction were first studied.

4.1.1. Sample Preparation and Experimental Methods

The CuPc/C_{60} bilayer structure (Figure 4.1) was prepared by collaborators at Imperial College London via thermal evaporation (the details of which are given in reference [86]). Since the goal of these measurements was to collect spatially-resolved EELS data, a cross-sectional sample of the CuPc/C_{60} bilayer structure was prepared using an FEI Helios NanoLab 600 DualBeam FIB/SEM. To ensure that any beam-damage from the FIB was minimized, a FIB preparation technique similar to that described in reference [92] was utilized.

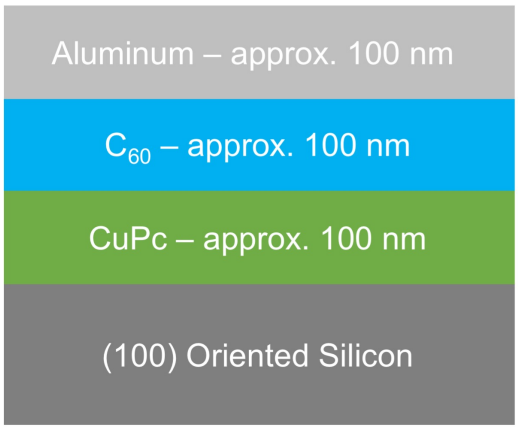

Figure 4.1: Schematic of the CuPc/C_{60} bilayer structure to be used in preliminary measurements of spatially-resolved EELS data.

EELS data of the CuPc/C_{60} bilayer structure was collected using a monochromated 60 keV electron beam in an FEI Titan^3 60-300 Image-Corrected S/TEM equipped with a Gatan Quantum spectrometer. A damage-minimization EELS acquisition method similar to that described for the bulk thin films in Section 3.2.3. was used to collect the data. However, it was necessary to adjust the method for the utilization of spectrum imaging, which is an EELS acquisition method in which spatially-resolved EELS data can be collected. During the measurements described in Chapter 3, the scanning electron beam was allowed to raster across the thin films continuously, and, at random points of this rastering, EELS spectra were collected. Thus, while it was known that the data was coming from a limited area of the sample (~1 μm^2 field of view), it was not precisely known from where in that ~1 μm^2 area the spectra had been collected. However, spectrum imaging allows spatial information to also be acquired during EELS acquisitions; essentially, as the STEM beam rasters along the sample, an EELS spectrum is collected at every point (pixel), thereby creating a three-dimensional data cube in which positional and spectral information is obtained [65,66,73]. Thus, similar to the measurements described in Section 3.2.3, the microscope and spectrometer were aligned far from the area of interest, the electron beam was blanked, and the sample area was blindly moved in the field of view. However, instead of continuously scanning the electron beam and collecting spectra from random points, the EELS acquisition parameters were adjusted for the acquisition of spectrum images. For these CuPc/C_{60} spectrum images collected, a step size of 1.6 nm (meaning that an EELS spectrum was collected every 1.6 nm) was used, as well as an exposure time of 20 μs. These spectra

were also collected with a convergence angle (α) of 5 mrad and a collection angle (β) of 15 mrad. Furthermore, instead of using the default CCD readout setting of 1x1 binning, which collects (for this microscope and spectrometer) ~7 pixels/second, the binning was set to be 1x130. This improved the speed of the acquisition to ~570 pixels/second, which allowed these large data sets to be collected very quickly. Once all of these settings were adjusted, the electron beam was unblanked and the EELS acquisition was immediately started. After acquiring these data sets, the data was analyzed using DigitalMicrograph.

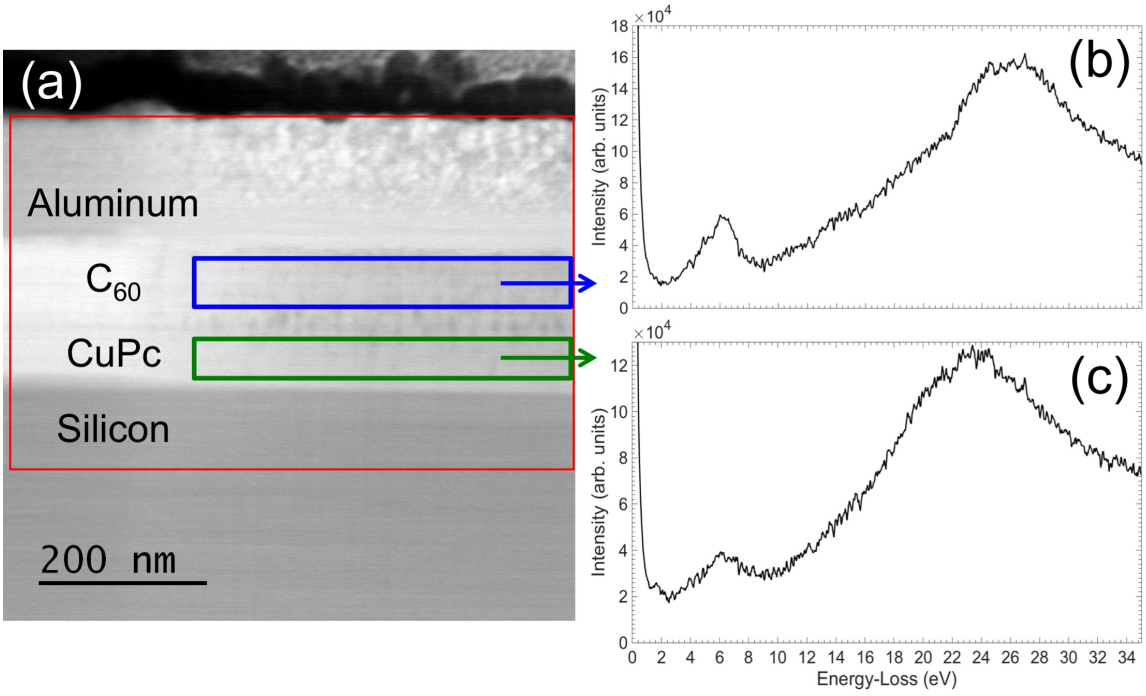

Figure 4.2: (a) HAADF image of the CuPc/C_{60} bilayer structure. The red box shows were spatially-resolved EELS data was collected, whereas the blue and green boxes show specifically where pixels were summed together to obtain the (b) C_{60} and (c) CuPc low-loss EELS spectra. This figure has been published in reference [86].

4.1.2. Determination of the Complex Dielectric Function

Before any data could be extracted from the collected spectrum image, the zero-loss peak (ZLP) of each pixel (spectrum) was first calibrated so that the ZLP maxima were all set to 0 eV. In order to extract a bulk low-loss spectrum for CuPc, pixels from only this layer were summed together to obtain the low-loss spectrum shown in Figure 4.2c. The pixels used in this summation were those enclosed by the green box (Figure 4.2a), which corresponded to a sample area of 48 nm by 448 nm (30 rows of 280 pixels). A similar process was used to extract a bulk low-loss spectrum for C_{60}. Pixels corresponding to an area of 57.6 nm by 448 nm (36 rows of 280 pixels, enclosed by the blue box in Figure 4.2a) were summed together, and the low-loss spectrum in Figure 4.2b was extracted. Care was taken to ensure that the pixels used to obtain these summed spectra were far enough from any interfaces (Al/C_{60}, C_{60}/CuPc, and CuPc/Si) so that these spectra were representative of only the bulk materials.

Comparing this low-loss spectrum for C_{60} to that collected for the bulk C_{60} thin film from Chapter 3 (Figure 3.8d, green line) shows very good agreement between the data sets. While the peaks may not be as distinct in this data, there are still the three major peaks at ~4 eV, ~5 eV, and ~6 eV that have been attributed to the bulk C_{60} signal. Conversely, comparing this CuPc low-loss spectrum with that collected for the bulk CuPc thin film (Figure 3.8a) shows that the two data sets differ significantly, which will likely impact the extracted imaginary part of the complex dielectric function (ε_2). However, it is worth noting that the energy of the plasmon peak for this CuPc low-loss spectrum (~24 eV) is similar to the value measured for the pure CuPc film (Figure 3.8a, blue line),

suggesting that the differences in the two spectra are not due to chemical differences between the two materials. However, to determine if there were any differences in the ε_1 and ε_2 spectra for this bilayer structure as compared to the bulk thin films, the zero-loss peak of each summed spectrum was first subtracted using the reflected-tail method (Section 2.2.1.1). The resultant spectrum was then deconvoluted (Section 2.2.1.2), and Kramers-Kronig analysis was used to determine ε_2 (Section 2.2.1.3). The results of these calculations are shown in Figure 4.3, along with the results for the bulk thin films obtained in Chapter 3 (Figures 3.10b and 3.10d).

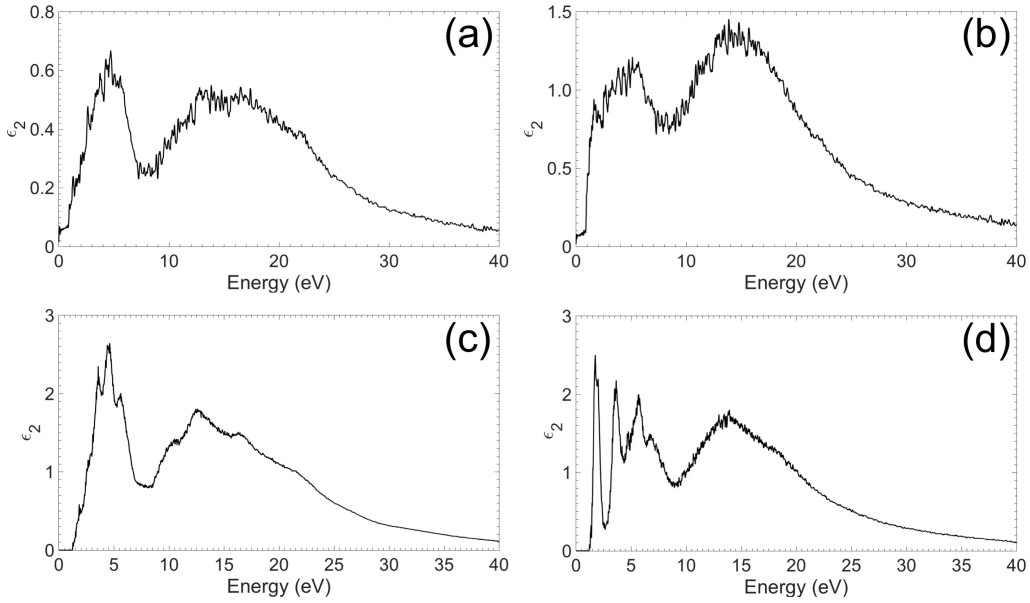

Figure 4.3: ε_2 spectra obtained via summing pixels from the (a) C_{60} and (b) CuPc layers of the CuPc/C_{60} bilayer structure (see text for details). Also shown are the ε_2 spectra obtained for the bulk thin films of (c) C_{60} and (d) CuPc, as discussed in Chapter 3. All four parts of this figure have been published in reference [86].

Just as with the low-loss spectrum, the peaks in ε_2 from the C_{60} layer (Figure 4.3a) correspond well to peaks measured for the pure C_{60} film (Figure 4.3c), although the data is noisier. However, the same observation cannot be made for the CuPc ε_2 spectrum collected from the CuPc layer in this structure (Figure 4.3b) and from the pure film (Figure 4.3d), as the sharp features from the pure film's ε_2 spectrum are not detected in the ε_2 spectrum extracted from the CuPc layer of the bilayer structure. The cause of the differences in these ε_2 spectra is not completely understood, although it has been theorized that the growth conditions used in the preparation of the CuPc layer of the bilayer structure resulted in molecules with various orientations, which would, in turn, result in an ε_2 spectra with contributions of the ε_2 signals from all of these various orientations [86]. Thus, differences between the CuPc ε_2 spectrum obtained from the pure thin film and the ε_2 spectrum obtained from the CuPc layer of the bilayer structure are most likely indicative of differences in the morphology of these thin films rather than beam damage incurred by the CuPc layer of the bilayer structure. Furthermore, since the ε_2 spectra for the pure C_{60} thin film and the C_{60} layer of the bilayer structure agreed, this analysis demonstrates that reliable spatially-resolved low-loss EELS data can be collected for electron beam-sensitive materials.

4.1.3. Tracking the CuPc/C_{60} Interface

Having shown that low-loss EELS data could be collected for OPV materials utilizing the technique of spectrum imaging, the next step was to try and track any differences in

the low-loss spectra from the bulk C_{60} layer, through the CuPc/C_{60} interface, and into the bulk CuPc layer. For the purposes of these comparisons, the CuPc low-loss EELS signal measured by summing the pixels in the bulk layer of the bilayer structure was taken to be the standard by which to compare these spectra. Instead of extracting low-loss spectra from relatively large areas (as shown in Figure 4.2a), pixels were only summed for areas of 4.8 nm by 448 nm (same length but smaller width). Spectra were first extracted for the bulk C_{60} layer (see Figure 4.4), and then subsequent spectra were collected in 5 nm steps through the remaining C_{60} layer, through the C_{60}/CuPc interface, and into the bulk CuPc layer. In the topmost spectra, the three peaks (at ~4, 5, and 6 eV) indicative of the C_{60} signal are observed. However, as the area investigated moves through the interface and into the CuPc layer, these three peaks are no longer observed. Rather, the two primary features in the CuPc spectrum in Figure 4.2c (at ~1.5 and 6 eV) are observed. Thus, it can be assumed that the signal measured halfway between (i.e. the pink and light blue lines in Figure 4.4) should be indicative of the interfacial signal between these two materials. Additionally, a shift in the energy of the plasmon peak was observed from ~26 eV (in the pure C_{60}) to ~23.5 eV (in the pure CuPc), and both of these values agree well with the data shown in Figure 3.9.

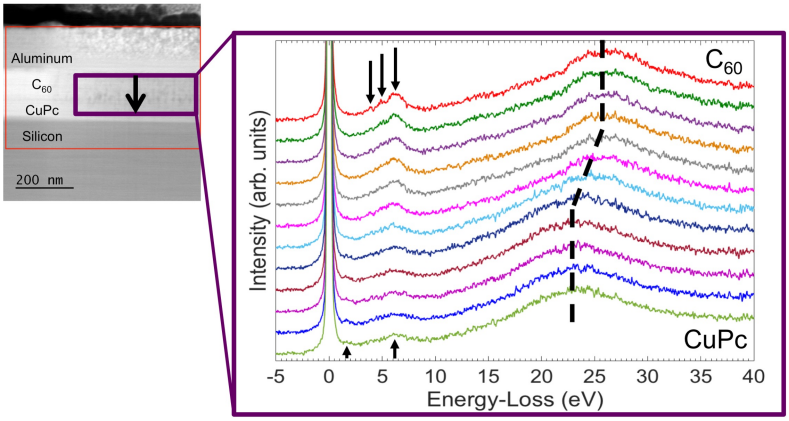

Figure 4.4: The low-loss signals were tracked from the bulk C_{60} (top spectrum) layer, through the C_{60}/CuPc interface, and into the bulk CuPc (bottom spectrum) layer for the area shown on the HAADF image enclosed by the purple box. These low-loss spectra were collected in ~5 nm steps. The dashed line shows the shift in the plasmon peak's energy, whereas the arrows indicate low-loss peaks attributable to pure C_{60} (top three arrows) and pure CuPc (bottom two arrows). This figure has been published in reference [86].

Unfortunately, since the ε_2 spectrum from the CuPc layer of this bilayer structure did not match that of the bulk CuPc thin film (for reasons previously discussed), it was not possible to track what peaks in ε_2 were changing (or if any new peaks were observed) in the C_{60} and CuPc spectra at the interface. However, it is clear from this analysis that it should be possible to acquire low-loss EELS data and extract the complex dielectric function at the interface between two organic materials.

4.2. Spatially-Resolved Low-Loss EELS of P3HT:PCBM OPVs

Having shown that it was possible to collect spatially-resolved low-loss EELS data for beam-sensitive materials in the case of a CuPc/C_{60} bilayer structure, the next step was to apply these same methods to an actual OPV device containing a P3HT:PCBM bulk-heterojunction photoactive layer. The primary goal of this study was to determine whether the pure P3HT and pure PCBM signals could be differentiated, and whether or not the interfacial signal between the two domains could be extracted. A P3HT:PCBM bulk-heterojunction OPV was prepared by collaborators at Lock Haven University of Pennsylvania, and a schematic of the device is shown in Figure 4.5a. The layers of MoO_3 and $CsCO_3$ are just a few nanometers thick, and so they are not resolvable in the HAADF image shown in Figure 4.5b.

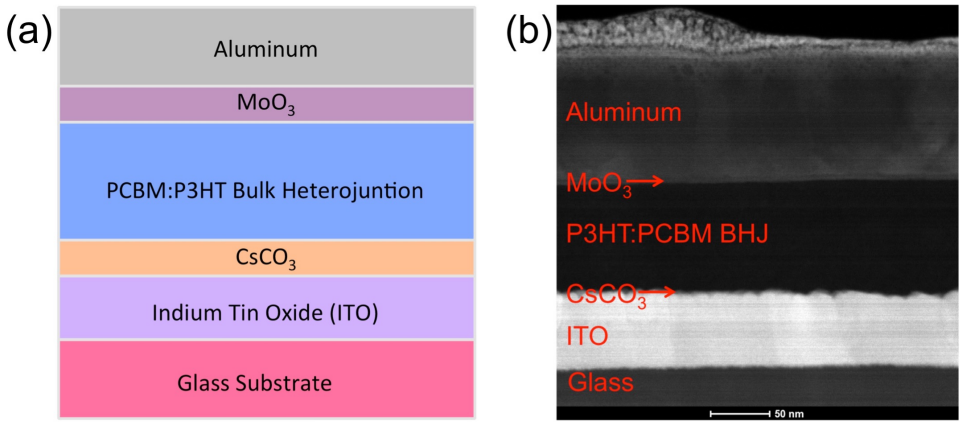

Figure 4.5: The (a) schematic of the P3HT:PCBM bulk-heterojunction OPV used in these EELS measurements and (b) the corresponding HAADF image collected *after* the acquisition of an EELS spectrum image.

4.2.1. Sample Preparation and Experimental Methods

A cross-sectional sample of the OPV device was prepared using an FEI Helios NanoLab 600 DualBeam FIB/SEM. While the goal in preparing any FIB foil for STEM-EELS measurements is to try to prepare thin samples (less than ~50 nm) so as to reduce the amount of plural scattering in the collected data, it was critical that this sample was even thinner. This is because the domain sizes of P3HT and PCBM within the P3HT:PCBM bulk-heterojunction are on the order of ~10 nm (as discussed in Section 1.1). As these domains are not continuous throughout the bulk-heterojunction, there is the possibility that the extracted FIB foil could contain portions from both P3HT and PBCM domains if the foil is not thinner than the size of the domains within the bulk-heterojunction. This would result in a measured low-loss EELS spectrum with contributions from both materials (P3HT and PCBM), from which it would be nearly impossible to differentiate the pure P3HT, pure PCBM, and P3HT/PCBM interfacial signals. However, it is extremely difficult to prepare FIB foils that are less than ~10 nm in thickness, so the goal for these preliminary measurements of a P3HT:PCBM bulk-heterojunction organic photovoltaic was to try and make the foil as thin as possible with the hope that the projection issue could be minimized.

Once the FIB foil was prepared of the OPV device, STEM-EELS measurements were made in an FEI Titan^3 60-300 Image-Corrected S/TEM equipped with a Gatan Quantum spectrometer using a 60 keV monochromated electron beam. The same spectrum-imaging acquisition methods used for the CuPc/C_{60} bilayer structure were also utilized for these OPV devices (see Section 4.1.1). For these measurements, the step size used was 1 nm,

the exposure time was 0.5 ms, the convergence angle (α) was 8.3 mrad, and the collection angle (β) was 13.8 mrad. Again, 1x130 binning of the CCD readout was used to acquire the data as quickly as possible (see Section 4.1.1). DigitalMicrograph was then used to analyze the spectra.

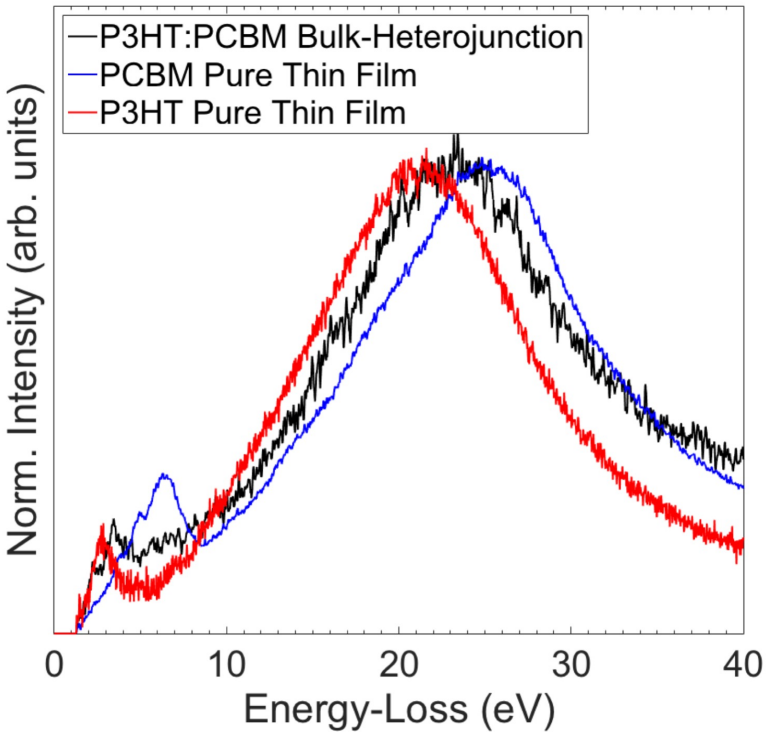

Figure 4.6: Inelastic spectra for the P3HT:PCBM bulk-heterojunction (shown in black), and for pure PCBM (shown in blue) and pure P3HT (shown in red). The plasmon energy of the P3HT:PCBM bulk-heterojunction sits right between the plasmon energies of the pure P3HT and pure PCBM films, suggesting that this signal may have contributions from both P3HT and PCBM domains in the thin film.

4.2.2. Spatial-Mapping of the Low-Loss Structure in the Bulk Heterojunction

Before extracting any spectra from the spectrum image, each pixel (spectrum) was aligned so that the zero-loss peak (ZLP) maxima were all centered about 0 eV. Using the reflected-tail method (Section 2.2.1.2) these ZLPs were then subtracted from every pixel (spectrum). This resulted in a spectrum image of only the inelastic signal for the P3HT:PCBM bulk-heterojunction (BHJ) layer.

Since the plasmon peak energy for pure P3HT is ~21 eV, and the plasmon peak energy for pure PCBM is ~25 eV (these values have been taken from Figures 3.9d and 3.9e), it should be possible to differentiate between P3HT domains and PCBM domains within the P3HT:PCBM bulk-heterojunction based on the plasmon peak energy of extracted low-loss spectra. However, when low-loss spectra were extracted from various areas throughout the P3HT:PCBM bulk-heterojunction, the plasmon peak energies were found to consistently fall between these two values (21 eV and 25 eV), as demonstrated in Figure 4.6. This inelastic spectrum was extracted from an area of 5 nm by 5 nm, the dimensions of which were selected so that the areas studied were smaller than the diameter of the domains (~10 nm) and is represented by the solid black line. Also shown in Figure 4.6 are the inelastic spectra obtained for pure P3HT (solid red line) and pure PCBM (solid blue line) discussed in Chapter 3. By comparing the P3HT:PCBM bulk-heterojunction signal to the pure P3HT and pure PCBM signals, it is clear that the energy of the P3HT:PCBM bulk-heterojunction plasmon peak falls directly in between the plasmon peak energies of pure P3HT and pure PCBM.

Additionally, a spatial map showing the variance of the plasmon energy throughout the bulk-heterojunction layer was extracted, as shown in Figure 4.7. This temperature map of the energy window 21.539 eV to 26.989 eV shows that the value of the plasmon energy is fairly constant throughout the bulk-heterojunction layer, suggesting that different regions of P3HT and PCBM are not differentiable.

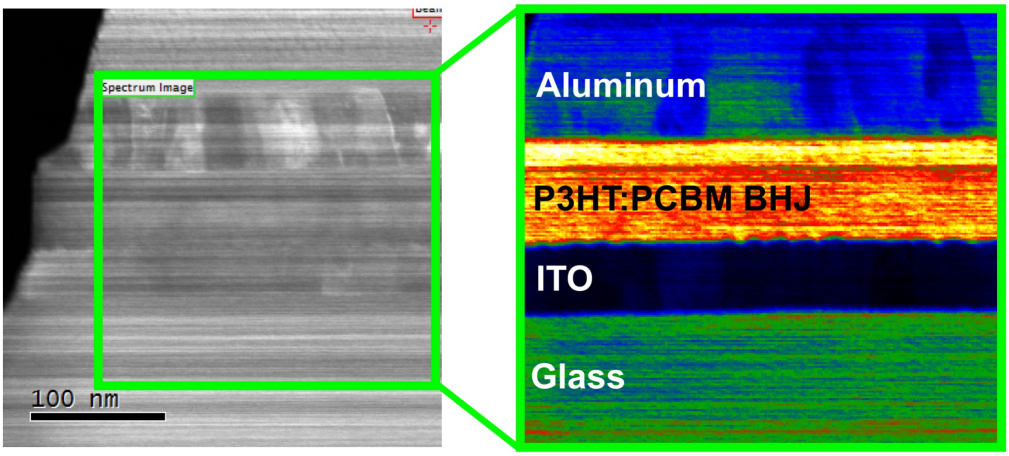

Figure 4.7: Temperature map for the energy window of 21.539 – 26.989 eV. This energy window corresponds to the energy of the plasmon peak shown for the P3HT:PCBM BHJ in Figure 4.6. As is clear from this temperature map, the energy of the plasmon peak is fairly constant throughout the entire BHJ.

The consistency in these plasmon peak energies suggests that these spectra are all convolutions of P3HT and PCBM signals Most likely, this indicates that the thickness of the sample is not on the order of one domain size (~10 nm), which is further corroborated by the fact that the t/λ value for this extracted spectrum is 0.8. This is thin enough to

avoid plural scattering but must not be thin enough to avoid the projection issues discussed previously in this section. However, knowing that the data collected were likely convolutions of both the P3HT and PCBM signals, the spectrum image was still analyzed to determine if any useful/interesting information could be extracted from the EELS data collected. (It is worth noting that it is not possible to normalize the intensity of each pixel of a spectrum image in DigitalMicrograph, which, unfortunately, affects the raw intensity displayed in the temperature map shown in Figure 4.7. The top of the P3HT:PCBM BHJ layer looks more intense in the temperature map only because the sample was thinner in that region, resulting in more counts in the low-loss spectra.)

Although the plasmon peak energies were fairly constant throughout the P3HT:PCBM bulk-heterojunction, the inelastic spectra differed depending on the area from which they were extracted. For example, by summing areas of 5 nm by 5 nm in different areas of the P3HT:PCBM bulk-heterojunction (Figure 4.8g), the inelastic spectra shown in Figures 4.8a-f were extracted. First and foremost, observations of low-loss features in these inelastic spectra suggests that any beam damage was minimized during the acquisition of the spectrum image of the P3HT:PCBM bulk-heterojunction. Secondly, when these spectra are compared to each other, it is interesting that different features are observed depending on the area from which the inelastic spectra were extracted. For example, sharp peaks at approximately 2 eV and 3.5 eV are observed in the inelastic spectra for areas A, D, and E, whereas such sharp peaks are not observed in the inelastic spectra for areas B, C, and F (although hints of these peaks are observed in the inelastic spectra from areas B and C). In order to determine whether these two sharp

peaks were directly attributable to either P3HT or PCBM, the inelastic spectrum extracted from area A was compared to the standard inelastic spectra collected for pure P3HT and pure PCBM. For these comparisons, the Nion STEM data (Section 3.4) was used due to the improved energy resolution of these spectra.

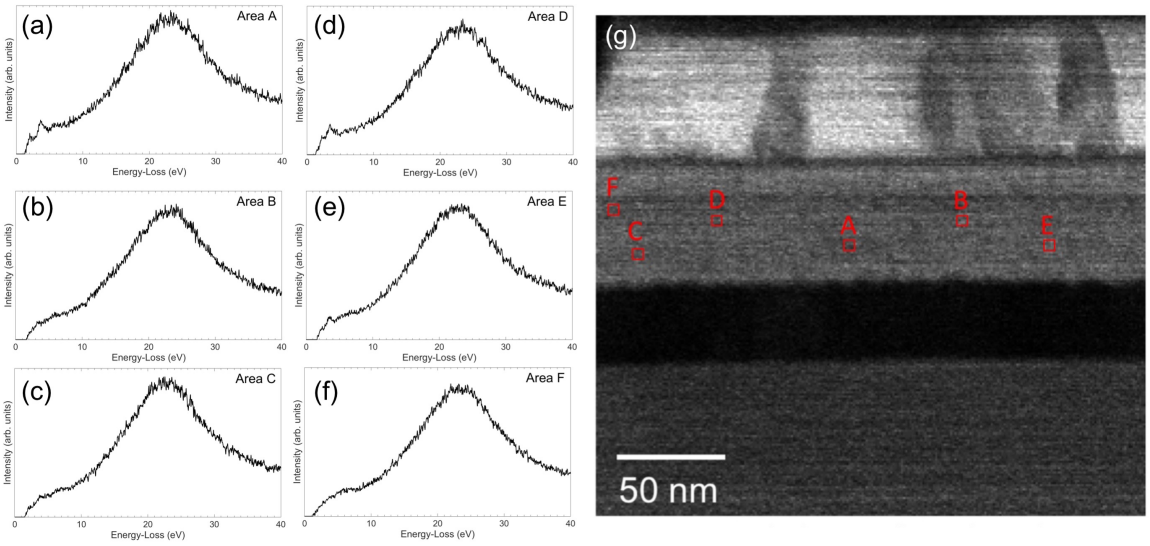

Figure 4.8: Representative inelastic spectra (a) – (f) selected from the corresponding areas (5 nm by 5 nm) as shown in (g). Two sharp peaks are only visible in spectra from areas (a), (d), and (e).

Comparing these inelastic spectra (Figure 4.9), it appears that the signal collected from area A has contributions from both PCBM and P3HT. The first peak, at ~2 – 3 eV (denoted by the red arrow) appears in both the P3HT:PCBM bulk-heterojunction inelastic spectrum (black line) and the pure P3HT inelastic spectrum (pink line). There also seems to be an hint of a peak at ~5 eV (denoted by the purple arrow) in the P3HT:PCBM bulk-

heterojunction inelastic spectrum, which could be due to the peak observed at that same energy in the pure PCBM inelastic spectrum. Finally, the peak at ~6 eV (denoted by the orange arrow) in the P3HT:PCBM bulk-heterojunction could be coming from the similar feature in the pure PCBM inelastic spectrum.

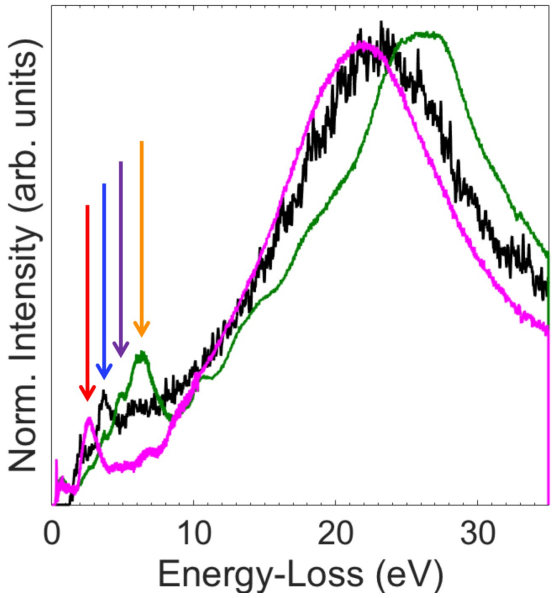

Figure 4.9: Overlay of inelastic spectra from area A of the P3HT:PCBM bulk-heterojunction from device D (black line), pure PCBM (green line), and pure P3HT (pink line). The pure PCBM and pure P3HT inelastic spectra are from the measurements made using the Nion STEM, as described in Section 3.4.

Although the previously discussed peaks seem to correlate to either P3HT or PCBM, it is possible that an interfacial signal at 3.5 eV has been detected in the P3HT:PCBM bulk-heterojunction inelastic spectrum. This peak at 3.5 eV (denoted by the blue arrow) does not appear to correspond to a strong peak in either the pure P3HT or pure PCBM

inelastic spectra. Even though a small feature is observed in the pure PCBM inelastic spectrum, the feature observed in the P3HT:PCBM bulk-heterojunction inelastic spectrum is more intense, suggesting that it is not simply arising from PCBM. Thus, it is possible that this feature corresponds to a transition arising at the interface between the P3HT and PCBM domains of the sample. When the electron beam passes through multiple layers of different materials (i.e. P3HT and PCBM domains), the inelastic spectrum collected should be a convolution of both the bulk materials and their interfacial responses. Thus, the observation of a P3HT peak (red arrow), PCBM peaks (purple and orange arrows), and possibly a P3HT/PCBM interfacial peak (blue arrow) further supports the hypothesis that the P3HT:PCBM bulk-heterojunction inelastic spectra obtained from these low-loss EELS measurements are most likely convolutions of signals from both P3HT and PCBM domains (as well as the interfaces between), which would occur if the sample was thicker than the sizes of the P3HT and PCBM domains in this bulk-heterojunction layer.

Temperature maps corresponding to the 2 eV and 3.5 eV features were obtained for the inelastic spectra of the P3HT:PCBM bulk-heterojunction, as shown in Figure 4.10. For the 2 eV peak, an energy range of 1.389 – 2.639 eV was used to obtain the map in Figure 4.10b. When looking at this temperature map, it appears that some signal at 2 eV is observed throughout the entire layer, and that there are just a couple of areas in which this feature is slightly more intense. This is consistent with the spectra shown in Figure 4.8. For instance, in Figure 4.8c, there is a peak at ~2 eV; it is just not as sharp as the peak observed in Figure 4.8a. Similarly, a temperature map of the 3.5 eV peak was

obtained by mapping the energy range of 2.989 – 4.589 eV (Figure 4.10c). Intensity corresponding to the 3.5 eV peak is observed throughout the entire layer, although there are a couple of areas in which the intensity is more intense. This is, again, consistent with the spectra shown in Figure 4.8, as the spectrum in Figure 4.8c has a small peak at ~3.5 eV, whereas the spectrum in Figure 4.8a has a sharp peak.

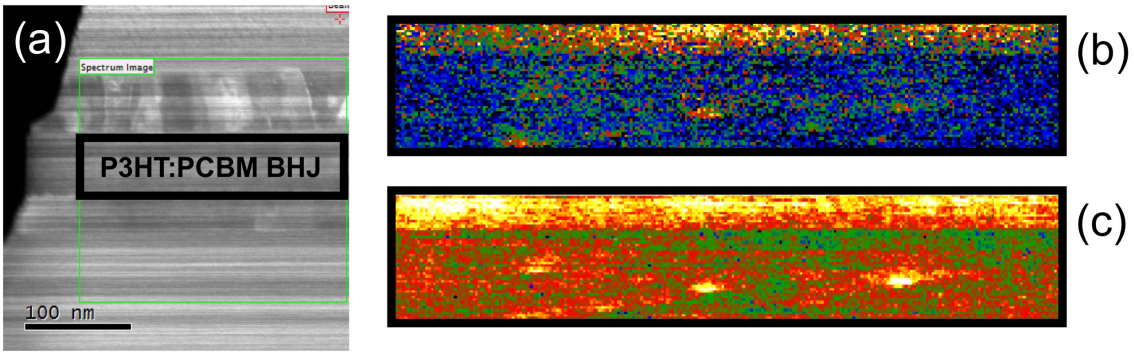

Figure 4.10: Temperature maps for the area corresponding to the (a) P3HT:PCBM bulk-heterojunction. These temperature maps are for the inelastic spectra over energy ranges of (b) 1.389 – 2.639 eV and (c) 2.989 – 4.589 eV. These energy ranges encompass the ~2 eV peak (b) and the ~3.5 eV peak (c).

It is not completely understood why only certain areas of this P3HT:PCBM bulk-heterojunction have sharp 2 eV and 3.5 eV features, whereas these features are less intense throughout the rest of the bulk-heterojunction layer. Thus, at this point, the next step should be to repeat this measurement and see if similar trends in the inelastic spectra are observed.

In the inelastic spectra examined here, evidence of both P3HT and PCBM signals were observed, suggesting that the sample was not irreparably beam-damaged during the acquisition of this EELS data. Although it was not possible to differentiate between P3HT and PCBM domains within this P3HT:PCBM bulk-heterojunction sample (and, therefore, measure the signal at a single P3HT/PCBM interface), this analysis strongly suggests that it should be possible to accomplish this goal if a sample with a thickness of ~10 nm can be prepared.

4.2.5. Summary

Spatially resolved low-loss EELS data was collected for a cross-sectional sample of a CuPc/C_{60} bilayer structure by extending the beam-damage minimization EELS acquisition method described in Chapter 3 to the acquisition of spectrum images. From these spectrum images, low-loss spectra were extracted for areas corresponding to the bulk CuPc and bulk C_{60} layers within this bilayer structure. Comparisons of these spectra suggest that the organic materials in this bilayer structure were minimally altered during the acquisition of the low-loss EELS data. Furthermore, it was demonstrated that changes in low-loss spectra could be detected at a relatively high spatial resolution by moving from the bulk C_{60} layer, through the C_{60}/CuPc interface, and into the bulk CuPc layer in 5 nm steps.

Following these primary measurements, an actual P3HT:PCBM bulk-heterojunction organic photovoltaic was studied using the same methods in order to acquire spatially

resolved low-loss EELS data. Unfortunately, it was not possible to differentiate between the P3HT and PCBM domains within this P3HT:PCBM bulk-heterojunction layer, and, therefore, it was not possible to extract the signal at a P3HT/PCBM interface. Most likely, this indicates that the sample studied was too thick and that the EELS spectra collected were comprised of contributions from both P3HT and PCBM domains (which was further supported by the observation of P3HT and PCBM peaks in the analyzed inelastic spectra).

Having proven that reliable EELS measurements could be collected with high spatial resolution for beam-sensitive organic materials, the major limitation in measuring the optoelectronic properties at the P3HT/PCBM interface in a P3HT:PCBM bulk-heterojunction organic photovoltaic will be preparing samples whose thickness is on the order of the domain size (~10 nm). However, for simpler functional devices (i.e. bilayers) that utilize electron beam-sensitive materials, the work shown here demonstrates how it should be possible to collect low-loss EELS data that is both reliable *and* spatially-resolved.

Chapter 5. EELS of an Organic Ferrimagnetic Semiconductor: $V[TCNE]_{x\sim2}$

As discussed in Section 1.2.1, vanadium tetracyanoethylene – $V[TCNE]_{x\sim2}$ – is an organic-based ferrimagnetic semiconductor known primarily for its room-temperature magnetic ordering. This property makes it a desirable material for various applications, such as magnetic shielding, magnonic circuits, and spintronic devices [47,50,51,54–56]. In fact, various studies have been conducted on $V[TCNE]_{x\sim2}$ in an effort to understand the magnetic properties of this material [48–50,53,55,56]. However, the optoelectronic properties have not yet been measured. Additionally, it has not been determined how the oxidation state of the vanadium ions varies throughout the thin film (if it does at all) as all previous reports of the vanadium oxidation state have utilized bulk characterization techniques [47,48,54].

In an effort to resolve these uncertainties, electron energy-loss spectroscopy (EELS) has been used to: (1) determine the oxidation state of vanadium in $V[TCNE]_{x\sim2}$, as discussed in Section 5.2, (2) track how the vanadium oxidation state varies throughout the $V[TCNE]_{x\sim2}$ thin film, as discussed in Section 5.3, and (3) probe the optoelectronic properties of $V[TCNE]_{x\sim2}$, as discussed in Section 5.4.

5.1. Sample Preparation and Experimental Methods

Samples of $V[TCNE]_{x\sim2}$ films were prepared by collaborators at The Ohio State University via chemical vapor deposition, the details of which are available in reference [113].

As discussed in Section 1.2.1, $V[TCNE]_{x\sim2}$ films are air-sensitive, which makes it extremely difficult to measure electron energy-loss spectra, because, unless a vacuum TEM transfer rod is available, the sample must be exposed to air during the sample loading process. Such exposure to air could cause the $V[TCNE]_{x\sim2}$ films to oxidize, which could affect the measured optoelectronic properties and oxidation states of the vanadium ions. Since a vacuum TEM transfer rod was not readily available, a sample loading process was developed in which a plan-view Al/$V[TCNE]_{x\sim2}$/SiN sample (Figure 5.1) was loaded into a (normal) TEM sample rod while both the sample and TEM sample rod were located within an argon-filled glovebox. Once the plan-view sample was loaded into the TEM sample rod, the end of the TEM sample rod was enclosed in a sealed cap, thus ensuring that the sample remained in the argon gas environment as the TEM sample rod was transported to the FEI Titan^3 60-300 Image-Corrected S/TEM used for these experiments. Once at the microscope, the sealed cap was removed from the end of the TEM sample rod, and the rod was immediately loaded into the microscope (into a vacuum environment). Thus, this process limited the amount of time that the sample was exposed to air to just the few seconds that it took to load the TEM sample rod into the microscope after the sealed cap was removed. As exposing the sample to some air was unavoidable via this method, an aluminum capping layer was grown on top of the

$V[TCNE]_{x\sim2}$ film to help prevent direct exposure of the $V[TCNE]_{x\sim2}$ layer to the air. Although the process of loading the plan-view sample into the TEM sample rod within an argon-filled glovebox was tedious, this method proved to be relatively efficient in limiting the amount of air the sample was exposed to prior to the EELS measurements.

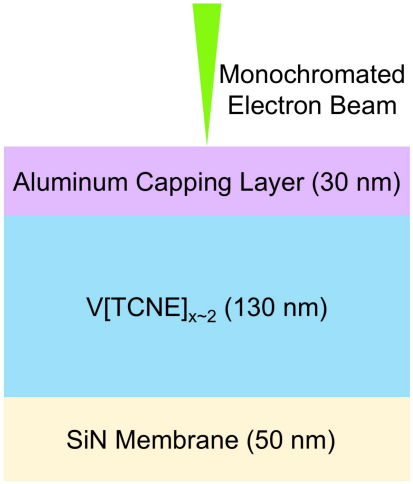

Figure 5.1: Schematic of the plan-view $V[TCNE]_{x\sim2}$ sample investigated using EELS. The SiN membrane serves as a support film for the $V[TCNE]_{x\sim2}$, and the Al served as a capping layer to prevent direct exposure of the $V[TCNE]_{x\sim2}$ thin film to air.

Once the sample was in the microscope, EELS data was collected using a monochromated 300 keV electron beam in an FEI Titan^3 60-300 Image-Corrected S/TEM outfitted with a Gatan Quantum spectrometer. These data were collected using the beam damage-minimization method developed for the organic photovoltaics in Section 3.2.3, as it was expected that the $TCNE^{2-}$ component of the $V[TCNE]_{x\sim2}$ thin films may be electron beam-sensitive (see Section 3.1. for an overview of beam damage

in organic materials). First, the microscope and spectrometer were both aligned in an area of the plan-view Al/V[TCNE]$_{x\sim2}$/SiN sample from which data was not going to be collected. The sample stage was then adjusted until the plan-view sample was brought into the field of view (which was approximately 1 μm^2 in area), following which the electron beam was blanked. While the electron beam was blanked, the sample stage was blindly adjusted so that an area of the plan-view sample that had not been previously exposed to the electron beam was brought into the field of view. Once the sample stage had been adjusted, the electron beam was unblanked and set to continuously raster across the sample. Immediately following this step, a low-loss EELS acquisition was begun, during which ten single spectra were collected from random areas within the field of view (using a dwell time of 100 ms) and summed together to form one single stacked spectrum. By summing the ten single spectra together and forming a single stacked spectrum, the signal-to-noise ratio (SNR) of the spectrum was improved. This method resulted in the low-loss spectrum shown in Figure 5.2.

Since this data was collected from an electron beam that was transmitted through a multi-layered plan-view sample, the data shown in Figure 5.2 is a convolution of the Al, V[TCNE]$_{x\sim2}$, and SiN signals, as well as any contributions from responses at the interfaces between those materials. Thus, it is not possible to immediately determine which features in this low-loss spectrum are attributable to V[TCNE]$_{x\sim2}$ (as opposed to Al or SiN). Theoretically, it should be possible to extract only the V[TCNE]$_{x\sim2}$ signal from this low-loss spectrum via the methods developed by Bolton and Chen [114]. However, when these methods were applied to this data set, it was determined that the analysis was

too challenging and time-consuming to pursue if there were the slightest possibility that data could instead be collected from a cross-sectional sample (the benefit in collecting EELS data from a cross-sectional sample is that spectra could be acquired for only the $V[TCNE]_{x\sim2}$ thin film, which would simplify the analysis of the EELS data tremendously).

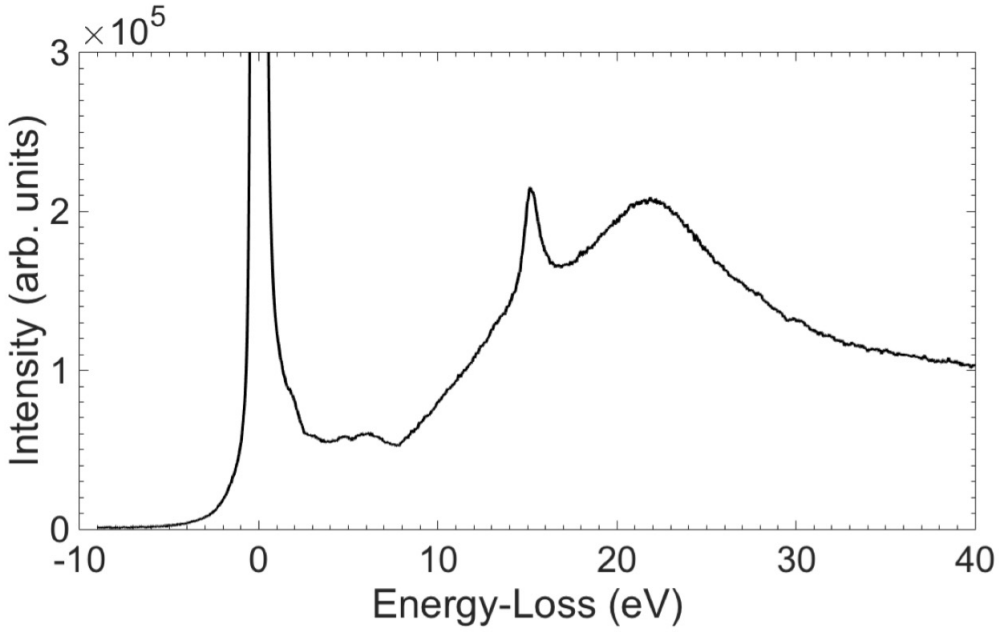

Figure 5.2: Low-loss EELS spectrum collected for the Al/$V[TCNE]_{x\sim2}$/SiN plan-view sample described in Figure 5.1. This spectrum is a convolution of the Al, $V[TCNE]_{x\sim2}$, and SiN signals, as well as their interfacial responses.

The easiest way in which to prepare a cross-sectional sample of a $V[TCNE]_{x\sim2}$ film would be to use a focused ion beam (FIB) microscope. However, as loading samples into and out of the FIB requires exposing the sample to air if special holders/attachments are

not available, it was not clear if it would even be possible to prepare a $V[TCNE]_{x\sim2}$ cross-sectional sample without the film oxidizing during this sample preparation process. Nevertheless, preparing a cross-sectional $V[TCNE]_{x\sim2}$ sample using the FIB was attempted, because, as mentioned before, preparing cross-sectional samples would simplify the EELS analysis immensely.

Although it was impossible to avoid exposing the sample to air during the FIB sample preparation process, certain steps were taken to ensure that any air-exposure was minimized. Again, collaborators grew a thin film of $V[TCNE]_{x\sim2}$ (this time on a Si substrate) and capped the layer with Al to prevent direct air exposure of the $V[TCNE]_{x\sim2}$ thin film while the sample was loaded into the FIB (Figure 5.3a). While inside an argon-filled glovebox, this $Al/V[TCNE]_{x\sim2}/Si$ sample was attached to an aluminum stub by using a carbon sticky tab, after which the sample was placed into an enclosed plastic container. This plastic container was then placed into multiple plastic bags in an attempt to keep the sample within an argon gas environment until it was to be loaded into the FEI Helios NanoLab 600 DualBeam FIB/SEM. Directly upon removal from the plastic bags and the plastic container, the $Al/V[TCNE]_{x\sim2}/Si$ sample was loaded into the FIB, and a cross-sectional thin foil of the sample was extracted. After extraction, this thin foil was immediately loaded into the TEM sample rod and, finally, into the FEI Titan^3 60-300 Image-Corrected S/TEM microscope.

Unlike the sample loading process for the plan-view sample, this process was more challenging, as there were multiple points during the sample preparation process that the sample was exposed to air. However, the goal of this method was to minimize the time

during which the sample was exposed to air with the hope that oxidation of the $V[TCNE]_{x\sim2}$ layer could be prevented.

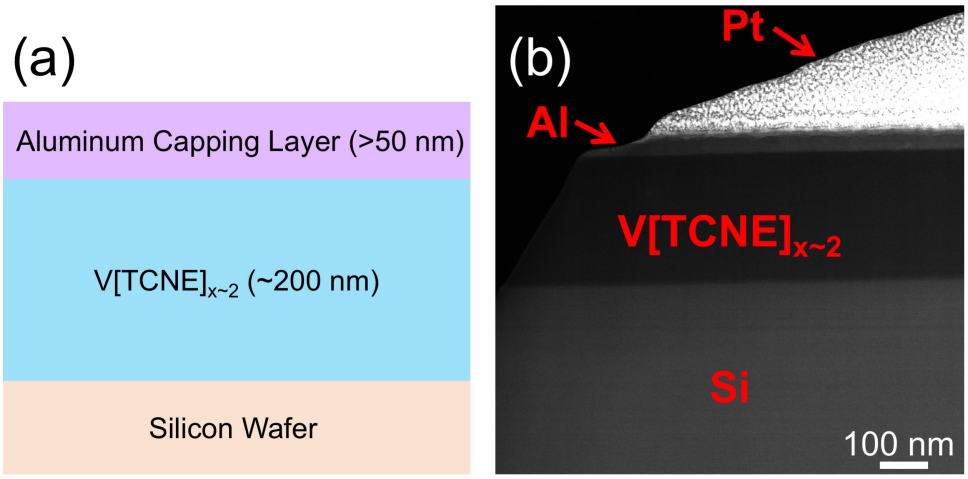

Figure 5.3: (a) Schematic of the sample prepared for cross-sectional EELS measurements. (b) HAADF image of the cross-section FIB foil prepared for the $V[TCNE]_{x\sim2}$ EELS measurements.

As with the plan-view sample, the FEI Titan^3 60-300 Image-Corrected S/TEM outfitted with a Gatan Quantum spectrometer was used in the acquisition of the EELS data. To collect site-specific EELS data, the method of spectrum imaging was utilized. As described in Section 4.1.1, spectrum imaging makes it possible to collect three-dimensional data sets in which extracted EELS spectra can be correlated to specific areas of the sample [65,66,73]. Since both the optoelectronic properties and the vanadium oxidation states were to be probed, both low-loss and core-loss spectrum images were

acquired. The low-loss spectrum images were collected for energy-losses less than 40 eV, and the core-loss spectrum images were collected for energy-losses between 505 and 55 eV. This core-loss energy range encompassed the oxygen-K edge (at 532 eV [115]), which could be used to prove whether or not the $V[TCNE]_{x\sim2}$ layer had oxidized during the sample preparation process, as well as the V-$L_{2,3}$ edge (L_3 = 513 eV, L_2 = 521 eV [116]), which could be used to determine the oxidation state of the vanadium ions in $V[TCNE]_{x\sim2}$. High-angle annular dark field (HAADF) images were collected after acquiring the EELS data, and an example HAADF image is shown in Figure 5.3b.

Analysis of the core-loss spectrum images were discussed in Sections 5.2 and 5.3, and the analysis of the low-loss spectrum images will be discussed in Section 5.4 (the specific accelerating voltages, steps sizes, exposure times, convergence angles, and collection angles used during the acquisitions of these low-loss and core-loss EELS data sets will also be outlined in these sections).

5.2. EELS of an Organic Ferrimagnetic Semiconductor: $V[TCNE]_{x\sim2}$

Based on X-ray absorption near edge structure (XANES) measurements of various vanadium oxides (see Figure 5.4), it has been determined that the energy of the V-L_3 peak should increase from 515.5 eV to 519 eV in approximately 0.7 eV steps as the oxidation state of vanadium increases from V^0 to V^{5+} [117]. This suggests that, if the energy of the V-L_3 peak is known, it should be possible to determine the oxidation state of the vanadium ions in $V[TCNE]_{x\sim2}$ thin films.

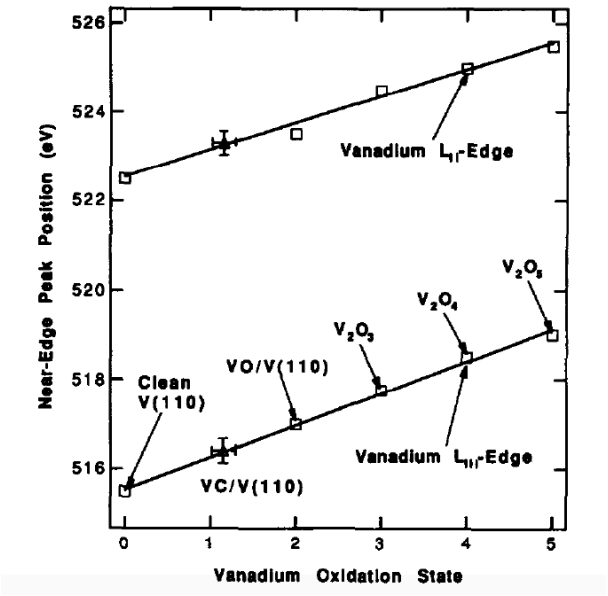

Figure 5.4: Relationship between the energy of the V-L_3 edge and the V oxidation state, as determined via XANES measurements of various vanadium oxides. This plot was originally published in reference [117].

As reported in reference [48], researchers have used XANES to determine the oxidation state of V in $V[TCNE]_{x\sim2}$. Figure 5.5a shows the results of these XANES measurements, and, from which the oxidation state of V in $[TCNE]_{x\sim2}$ was determined to be approximately V^{2+} [48]. These measurements were consistent with other XANES measurements of $V[TCNE]_{x\sim2}$ thin films, as shown in Figure 5.5b [118]. Although XANES can be used to determine similar information about a sample as core-loss EELS can (such as oxidation states) [38], these measurements cannot be made with the high spatial resolution that is achievable in the STEM, which means that only the bulk signal of the oxidation state can be extracted. Thus, core-loss EELS (see Section 2.2.2 for an overview) measurements were made to determine: (1) the oxidation state of the vanadium

ions in $V[TCNE]_{x\sim2}$ and if it confirms previous assertions that the oxidation state is V^{2+} and (2) how the oxidation state varies (if it does) throughout the $V[TCNE]_{x\sim2}$ thin film. The first analysis will be discussed in this section, while the second analysis will be discussed in the next section (Section 5.3).

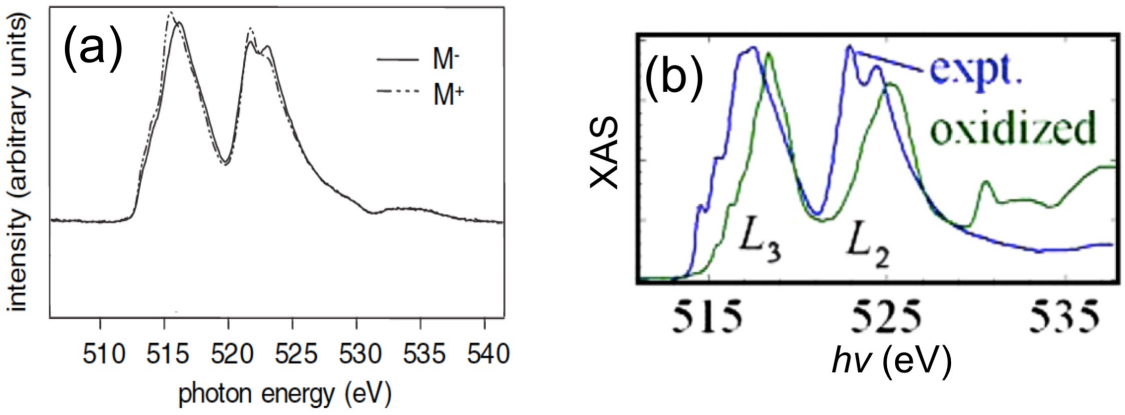

Figure 5.5: (a) XANES measurements of the V-$L_{2,3}$ edge in $V[TCNE]_{x\sim2}$. The first peak is attributable to the V-L_3 peak and the second is attributable to the V-L_2 peak. This plot was originally published in reference [48] and has been adapted for use in this dissertation. (b) XANES measurements of the V-$L_{2,3}$ edge in $V[TCNE]_{x\sim2}$ for oxidized (green) and un-oxidized (blue) films. This plot was originally published in reference [118] and has been adapted for use in this dissertation.

For these EELS measurements, a FEI Titan^3 60-300 Image-Corrected S/TEM with a 300 keV monochromated electron beam was utilized to collect low-loss and core-loss EELS spectrum images using dual-EELS mode (which is described in Section 3.4.2). Although the oxidation state will be determined from the core-loss EELS spectrum

images, it was necessary to also collect low-loss EELS spectrum images in order to properly align the core-loss EELS data. If the core-loss EELS data were not aligned, an absolute value of the V-L_3 peak could not be extracted, and, thus, the oxidation state of the vanadium ions could not be determined. However, the only way to accurately align any EELS spectrum is to set the maxima of the zero-loss peak (ZLP, described in Section 2.2) to 0 eV, which is why corresponding low-loss EELS spectrum images were also collected via dual-EELS mode. These low-loss and core-loss EELS spectrum images were collected using an α (convergence angle) of 5.5 mrad, a β (collection angle) of 8.5 mrad, and an energy dispersion of 0.025 eV/channel (a larger value of β than α was used to ensure that all of the signal from the transmitted electron beam was collected). Furthermore, the core-loss spectrum images were acquired using a step size of 3.5 nm and an exposure time of 50 ms per pixel. Additionally, the CCD was set to 1x130 binning (rather than 1x1 binning) to increase the readout speed to ~570 pixels/second. This reduced the time necessary for the acquisition of these large data sets (see Section 4.1.1).

The first step in analyzing the collected core-loss spectrum image was to align each pixel (spectrum) by using the ZLP of the sister low-loss spectrum image collected during the dual-EELS acquisition. Once the core-loss spectra were properly calibrated, 84 rows of 114 pixels of the core-loss spectrum image were summed together (corresponding to an area of ~400 nm by ~295 nm, see the red box in Figure 5.6), and a core-loss spectrum was extracted (blue line in Figure 5.6), the energy resolution of which was 0.35 eV. In examining this core-loss spectrum, there is no appreciable signal measured at the oxygen-K edge (532 eV [115]), which proves that the sample did not oxidize during the sample

preparation process. This suggests that, if the proper steps are taken (as described in Section 5.1), it should be possible to prepare cross-sectional FIB foils of air-sensitive samples like $V[TCNE]_{x\sim2}$. Secondly, the two peaks observed in the core-loss spectrum shown in Figure 5.6 are attributable to the V-$L_{2,3}$ edge [116], for which the first peak is attributed to the V-L_3 peak and the second peak is attributed to the V-L_2 peak.

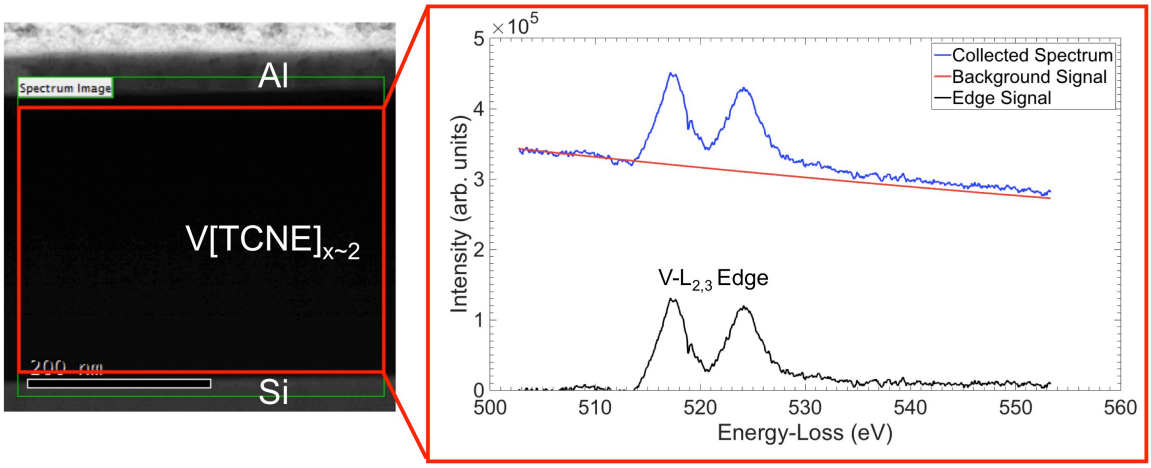

Figure 5.6: Area from which the bulk core-loss EELS data shown on the right was extracted (~400 nm by ~295 nm). A power law model was used to extract the background signal (red) from the collected core-loss spectrum (blue) in order to obtain the V-$L_{2,3}$ edge signal (black).

Having extracted the core-loss spectrum, the background signal of the V-$L_{2,3}$ edge was subtracted from the spectrum using the power law background subtraction routine in DigitalMicrograph (Section 2.2.2), as shown by the red line in Figure 5.6. The remaining signal (shown in black) correlates to the actual V-$L_{2,3}$ edge signal. In order to

quantitatively determine the value of energy-loss corresponding to the maximum of the V-L_3 peak, Gaussian functions of the form $f(x) = Ae^{-((x-B)/C)^2}$ were then fitted to each of the peaks V-$L_{2,3}$ of the edge signal shown in Figure 5.6. This value of energy-loss should correspond to a specific vanadium oxidation state as energy shifts of core-loss edges correspond to changes in the chemistry of the specimen [66].

From the Gaussian functions fitted to the V-L_3 peak, the energy-loss associated with the maximum of this peak is 517.4 eV, which best corresponds to an oxidation state of ~V^{2+} based on the results of Figure 5.4. This corroborates previous measurements in which the oxidation state was determined to be V^{2+} for vanadium in $V[TCNE]_{x\sim2}$ thin films [47,48,54]. However, what is more interesting is that, upon comparing the shape of the V-$L_{2,3}$ edge obtained from these EELS measurements to that obtained from XANES measurements (Figure 5.5), the EELS V-L_2 peak does not exhibit the same doublet structure that is observed in the both the XANES data. (The XANES data shown in Figure 5.5a were collected with reversed magnetizations, M^+ and M^- [48]). Although the observation of only a single V-L_2 peak is consistent with other EELS measurements of vanadium compounds [119,120], it is not immediately clear why the EELS data should differ from the XANES data for the V-L_2 peak. The natural line widths of the V-L_2 core level should not prohibit the observation of the doublet on the V-L_2 peak since the energy broadening of this core level is only ~0.3 eV [66], which is below the energy resolution (0.35 eV) used to acquire the data. Furthermore, since the doublet peaks are separated by at least 1 eV, the energy resolution should not prohibit the observation of the doublet structure either.

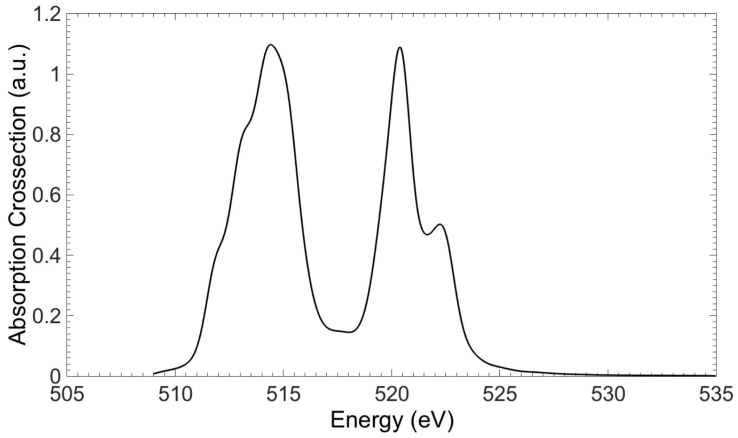

Figure 5.7: Simulated V-$L_{2,3}$ edge using the CTM4XAS software [121]. The V^{2+} oxidation state used, along with octahedral symmetry, 10Dq = 2.4 eV, Gaussian broadening = 0.35 eV, L_3 broadening = 0.2 eV, and L_2 broadening = 0.4 eV (all other values were left as defaults).

Computer simulations using the CTM4XAS software developed by de Groot [121] were used to perform crystal field multiplet calculations in order to simulate the core-loss EELS spectrum for the V-$L_{2,3}$ edge. In this simulation, the oxidation state of the vanadium was set to V^{2+}, the symmetry was set to octahedral (Oh) [48,49,54,118], and the Gaussian broadening (which correlates to the instrumental broadening) was set to 0.35 eV since that was the energy resolution of the EELS measurements. A previous report available in the literature stated that, for $V[TCNE]_{x\sim2}$, the value of the cubic crystal field splitting (10Dq) should be 2.4 eV, and the values of the L_2 and L_3 broadening should be 0.4 eV and 0.2 eV, respectively [118]. Using these values, the simulated spectrum shown in Figure 5.7 was obtained. In this spectrum, the doublet peak is still observed for the L_2 peak, further confirming that the energy resolution of the EELS

measurement should not be the reason for why this doublet structure is not observed in the experimental data. Furthermore, although the availability of a Coster-Kronig decay channel broadens the L_2 component [120,122], this broadening should be accounted for in the 0.4 eV. XANES measurements showed that the V-L_2 doublet peak broadens to a single peak when oxidized (see Figure 5.5b) [118], but, as proven here, there is no oxygen signal in the core-loss EELS spectrum (Figure 5.6), suggesting that this sample has not been oxidized.

Thus, it is currently unclear why the EELS V-L_2 peak does not exhibit the same doublet structure observed in the XANES data available in the literature for $V[TCNE]_{x\sim2}$ [48,118]. Since these are magnetic materials, there is the possibility that magnetic effects could affect the EELS data collected, or, conversely, perhaps the sample grown is not homogenous in its octahedral symmetry, which may also affect the shape of the V-L_2 peak. Before immediately attempting to answer these questions, though, it would be most prudent to first determine if it is even possible to measure the doublet structure of the V-L_2 peak via EELS by making similar measurements as the ones shown here on standard vanadium compounds (i.e. oxides and carbides). Then, depending on whether or not the $V\text{-}_{L2}$ doublet structure is observed the question that can be asked is either (1) why is this structure observed in XANES measurements but not EELS measurements, or (2) why is this structure observed in standard vanadium compounds but not $V[TCNE]_{x\sim2}$.

5.3. Spatial-Mapping of the Oxidation State of Vanadium

A primary advantage of measuring the oxidation state of vanadium ions in $V[TCNE]_{x\sim2}$ thin films using STEM-EELS is that the homogeneity/inhomogeneity of the vanadium oxidation state can be tracked throughout the thin film with very high spatial resolution. The same data set acquired in the previous section was used to extract the V-$L_{2,3}$ edge for much smaller areas of the $V[TCNE]_{x\sim2}$ layer, as only 5 rows of 117 pixels (~17.5 nm in height, ~410 nm in width) were summed together (as opposed to 84 rows of 114 pixels used in the previous section). These spectra were extracted sequentially from the top of the $V[TCNE]_{x\sim2}$ film to the bottom of the film in order to track any changes in the core-loss spectra, and the background signal was subtracted using the power law subtraction (Section 2.2.2) routine available in DigitalMicrograph, leaving only the edge signal remaining. Figure 5.8 shows this tracking of the V-$L_{2,3}$ edge signal through the $V[TCNE]_{x\sim2}$ thin film.

While Figure 5.8a suggests that there is no variance in the energy at the maxima of the V-L_3 edge, (and therefore in the oxidation state of the vanadium ions) from the top of the $V[TCNE]_{x\sim2}$ thin film to the bottom of the $V[TCNE]_{x\sim2}$ thin film, Gaussian functions were again fitted to each of the L_3 peaks in these core-loss edge signals in order to definitively prove that this peak energy value was constant. Of the 16 sequential spectra that were used in the tracking of the oxidation state, the value of the peak energy was determined to be 517.3 eV for three of the spectra and 517.4 eV for the other thirteen, which conclusively proves that the oxidation state of the vanadium ions in the $V[TCNE]_{x\sim2}$ is not changing throughout this thin film.

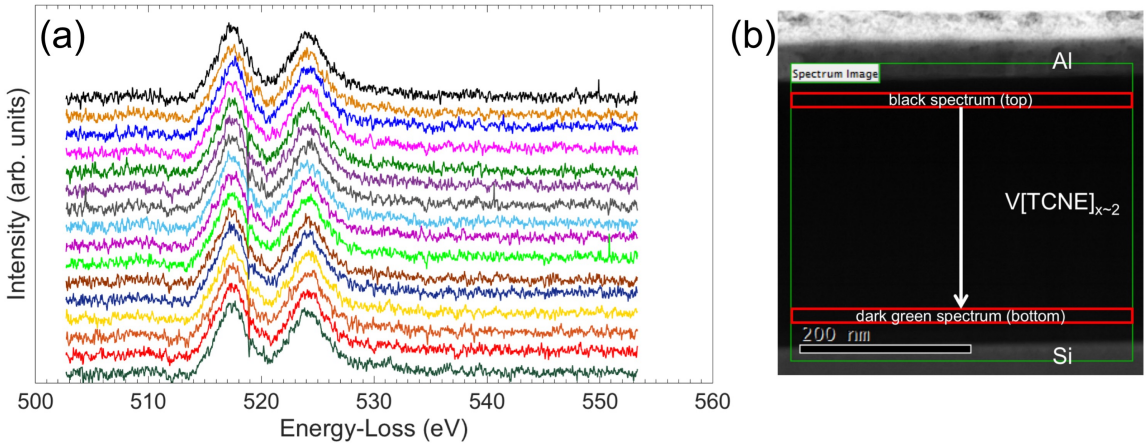

Figure 5.8: (a) V-$L_{2,3}$ edge signals obtained from areas of 17.5 nm by 410 nm of the $V[TCNE]_{x\sim2}$ thin film, as shown in (b). The topmost spectrum, shown in black, correlates to the topmost area of the thin film. As these stacked spectra show, there is no variance in the energies of the L_3 peak, which suggests that the oxidation state of the vanadium ions is constant throughout the $V[TCNE]_{x\sim2}$ film.

This is an extremely important determination, as it was not known previously whether or not the oxidation state of the vanadium ions varied throughout the $V[TCNE]_{x\sim2}$ thin film. However, as this analysis shows, the oxidation state is constant throughout the thin film, suggesting that the chemical composition of this $V[TCNE]_{x\sim2}$ thin film is fairly homogenous.

5.4. Probing the Optoelectronic Properties of $V[TCNE]_{x\sim2}$

For these EELS measurements, a FEI Titan^3 60-300 Image-Corrected S/TEM with a 300 keV monochromated electron beam was utilized to collect low-loss and core-loss EELS spectrum images. These low-loss and core-loss EELS spectrum images were collected using an α (convergence angle) of 5.5 mrad, a β (collection angle) of 8.5 mrad, and an energy dispersion of 0.025 eV/channel (a larger value of β than α was used to ensure that all of the signal from the transmitted electron beam was collected). Furthermore, the low-loss spectrum images were acquired for energy-losses of -5 to 45 eV using a step size of 0.83 nm and an exposure time of 0.1 ms per pixel. Additionally, the CCD was set to 1x130 binning (rather than 1x1 binning) to increase the readout speed to ~570 pixels/second, as this reduced the time necessary for the acquisition of these large data sets (see Section 4.1.1). The core-loss spectrum image was collected for energy-losses of 505 to 555 eV using a step size of 1.1 nm and an exposure time of 5 ms. Again, the CCD was set to use 1x130 binning during the readout process in order to increase the readout speed. As these low-loss and core-loss spectra were not acquired in dual-EELS mode, the low-loss spectrum image was collected first to ensure that any beam-damage that could affect the measured optoelectronic properties was minimized. The energy resolution of a single pixel (spectrum) was determined to be 0.225 eV.

To first determine whether or not the $V[TCNE]_{x\sim2}$ had oxidized during the sample preparation process, a representative core-loss spectrum was extracted from the core-loss spectrum image by summing pixels in the $V[TCNE]_{x\sim2}$ layer (dimensions of ~220 nm by ~300 nm in height), as shown in Figure 5.9. As no strong peak is observed at the oxygen-

K edge (532 eV [115]), this proves that the V[TCNE]$_{x\sim2}$ layer had not oxidized. Thus, any low-loss spectra extracted should be representative of the bulk V[TCNE]$_{x\sim2}$ material.

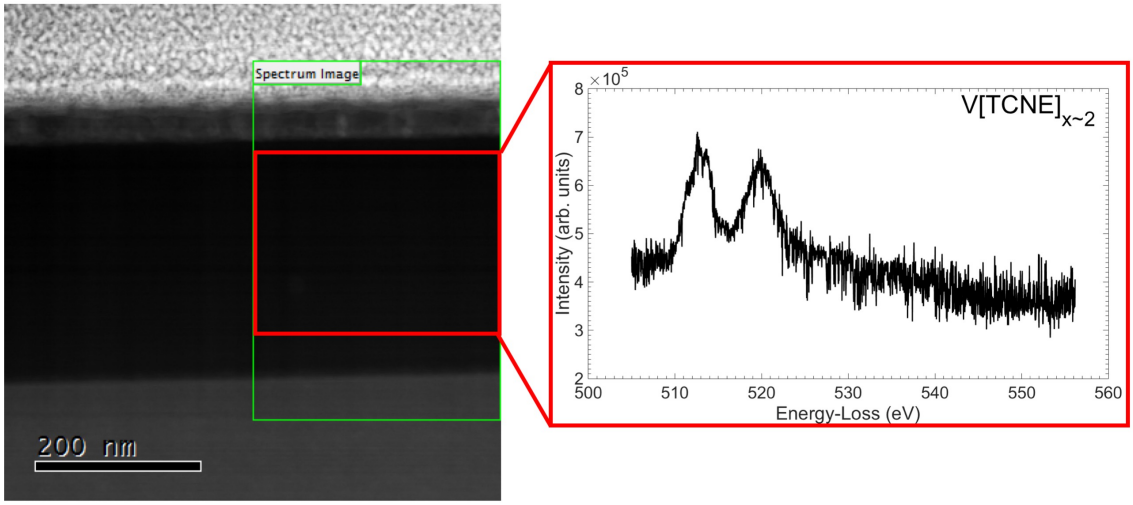

Figure 5.9: By summing all of the pixels included in the red box (left), the V[TCNE]$_{x\sim2}$ core-loss EELS spectrum encompassing the V-$L_{2,3}$ edge, as well as the O-K edge, was determined. As there is not strong peak at the O-K edge (~532 eV), it can be assumed that the V[TCNE]$_{x\sim2}$ layer has not oxidized.

Having proven that the low-loss EELS data collected for the V[TCNE]$_{x\sim2}$ sample prepared via FIB had not oxidized, the next step was to process the low-loss EELS data in order to extract the complex dielectric function. First, each pixel (spectrum) of the low-loss spectrum image was calibrated so that the maxima of the zero-loss peak (ZLP, see Section 2.2.1.1) was set to 0 eV. A bulk V[TCNE]$_{x\sim2}$ low-loss EELS spectrum was then extracted from the low-loss spectrum image by summing most of the pixels that

corresponded to the $V[TCNE]_{x\sim2}$ layer. Figure 5.10 shows the area over which these pixels were summed (dimensions of ~135 nm by ~295 nm) and demonstrates how the area summed was positioned far enough away from both the Al and Si layers such that interfacial signals would not affect the data analyzed. Unlike the low-loss EELS spectrum shown in Figure 5.2, this low-loss EELS spectrum no longer has contributions from the aluminum capping layer or the substrate. Thus, since its signal is entirely attributable to $V[TCNE]_{x\sim2}$, the processing of the data should be fairly straightforward. Furthermore, there are observable features in the 0 – 10 eV energy-loss range of this low-loss spectrum, which should, hopefully, correlate to features in the complex dielectric function spectra. The energy resolution of this summed spectrum was determined to be 0.225 eV.

As with all low-loss spectrum analyses, the first step in analyzing this extracted low-loss spectrum (Figure 5.10) was to remove the ZLP from the spectrum. This was accomplished by using the reflected-tail method (see Section 2.2.1.1). Similar to the other EELS analyses discussed in the previous two chapters, it was necessary to determine what value of reflected-tail cutoff (given in multiples of the half-width at quarter-maximum, HWQM) was most appropriate. As discussed in Section 2.2.1.1, this value controls how much of the ZLP tail from the energy-gain (left) side of the ZLP is reflected to the energy-loss (right) side of the ZLP [74]. Various multiples of HWQM were tried, as shown in Figure 5.11a, and, based on this analysis, a value of 2.5 HWQM resulted in the most symmetric reflected tail, as values larger than this caused a kink at the splicing

point between the experimental ZLP and the reflected tail on the energy-loss side, as denoted by the circles.

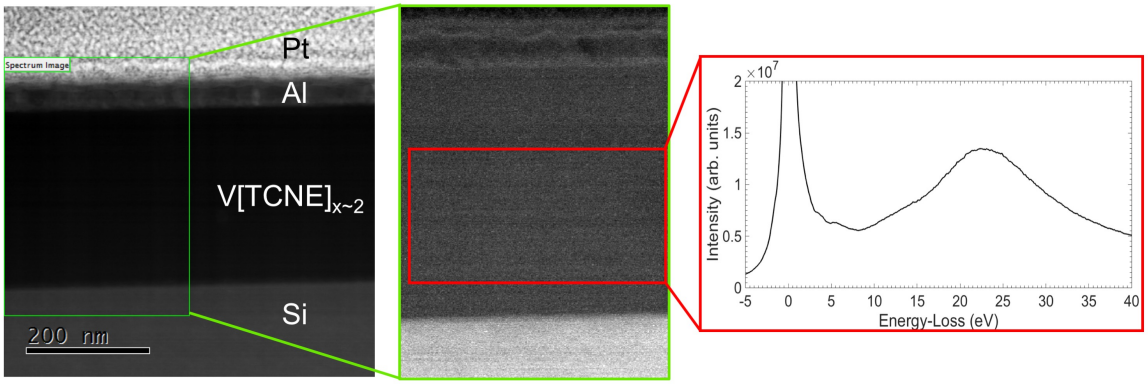

Figure 5.10: Extraction of the bulk low-loss spectrum for the $V[TCNE]_{x\sim2}$ layer of the sample shown in Figure 5.3a. Outlined in green is the area over which the entire spectrum image was collected, whereas outlined in red is the area for which pixels were summed to obtain the low-loss spectrum for the $V[TCNE]_{x\sim2}$ layer. This area was ~153 nm by ~295 nm.

Using this value of reflected-tail cutoff (2.5 HWQM), the ZLP was subtracted from the low-loss spectrum using the reflected-tail subtraction routine in DigitalMicrograph, as shown in green in Figure 5.11b. Also shown in this figure are the extracted experimental spectrum (black) and resultant inelastic spectrum (pink). The rationale in choosing 2.5 HWQM as the value for the reflected-tail cutoff was explained here (as opposed to previous analyses in which it has been glossed over) because, upon noticing that the onset of the inelastic spectrum is at ~0.5 eV and that the feature associated with this onset is fairly sharp, one may think that that feature is due to an incorrect subtraction of the ZLP (i.e. an artifact due to not subtracting enough ZLP signal in the 0.5 – 1.0 eV range).

However, as shown here, that is not the case and the onset at ~0.5 eV is real. What might vary is the precise value of this onset, as depending on the ZLP subtraction, it could be closer to 0.4 or 0.6 eV.

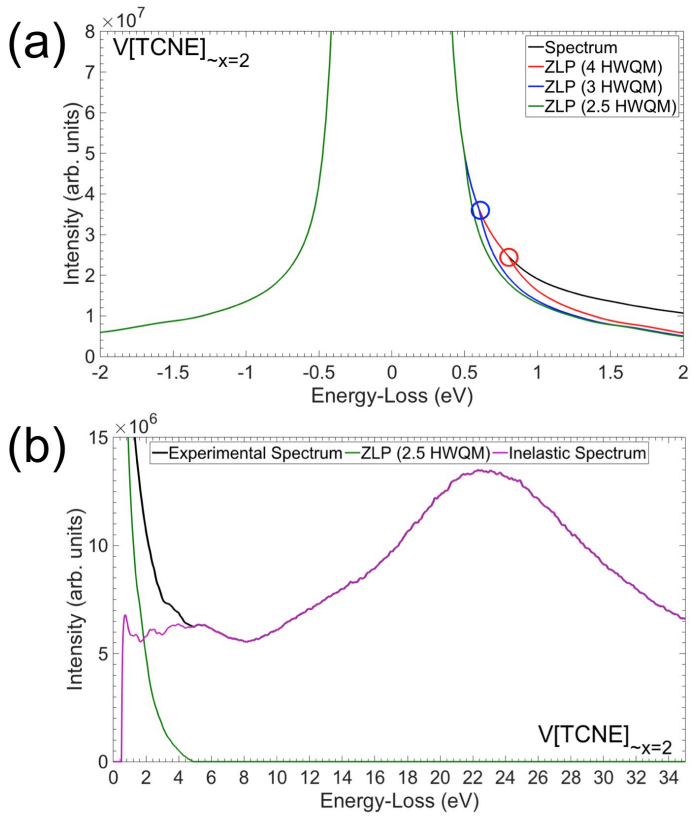

Figure 5.11: (a) Overlay of ZLPs with different multiples of HWQM used in setting the reflected-tail cutoff. For values larger than 2.5, the reflected-tail ZLP subtraction routine used resulted in a kink at the splicing point between the experimental ZLP and the reflected tail, as denoted by the two circles on the plot. (b) Results of the ZLP subtraction process via the reflected-tail method. A reflected-tail cutoff value of 2.5 HWQM was used. The onset of the inelastic spectrum is at ~0.5 eV.

After subtracting the ZLP from the extracted low-loss spectrum, the Fourier-Log deconvolution (see Section 2.2.1.2) routine in DigitalMicrograph was used to obtain the

single scattering distribution (SSD) for this spectrum. This extracted SSD is shown in Figure 5.12 (black line) along with the SSD obtained for the Al/V[TCNE]$_{x\sim2}$/SiN plan-view sample (which has additional contributions besides V[TCNE]$_{x\sim2}$, see Section 5.1). The SSD extracted from the plan-view data (red line) was multiplied by a factor of 60 so that it was on the same intensity scale as the cross-sectional data (the intensity of the plan-view sample was likely lower due to that sample being thicker (1.47 t/λ) than the cross-sectional sample (0.45 t/λ) was). Comparing these two SSDs suggests that the low-loss features observed below 10 eV in the low-loss spectrum for Al/V[TCNE]$_{x\sim2}$/SiN plan-view sample were most likely due to the V[TCNE]$_{x\sim2}$ layer. However, all uncertainty has been eliminated by preparing a cross-sectional sample from which a low-loss spectrum was extracted for only the V[TCNE]$_{x\sim2}$ layer.

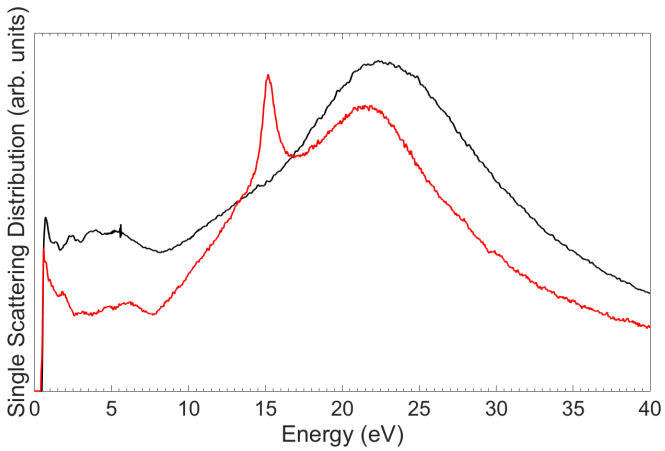

Figure 5.12: Comparisons of the SSD obtained for the cross-sectional sample (shown in black) and the plan-view sample (shown in red). Both the onset of the spectra and the low-loss features in these two spectra agree well.

To extract the real (ε_1) and imaginary (ε_2) parts of the complex dielectric function, Kramers-Kronig Analysis (see Section 2.2.1.3) was performed on the SSD obtained for the $V[TCNE]_{x\sim2}$ layer of the cross-sectional sample. As mentioned in Section 2.2.1.3, one of the inputs necessary to perform this analysis in DigitalMicrograph is the refractive index. However, at the writing of this text, the refractive index has not been reported for $V[TCNE]_{x\sim2}$, and it was not possible to experimentally measure it (for example, using variable angle spectroscopic ellipsometry) due to the air-sensitive nature of the $V[TCNE]_{x\sim2}$ films. Thus, an approximation of the refractive index, *n*, was obtained by searching the literature for the refractive indices of other organic semiconductors. Based on this search, a value of *n* between 1.6 and 2.0 was deemed appropriate for $V[TCNE]_{x\sim2}$ [123,124]. Unfortunately, these values were higher than what was originally anticipated, which meant that Cherenkov radiation could not be ignored.

Cherenkov radiation occurs when the velocity, *v*, of the electrons traveling through a sample is greater than the speed of light in that same sample [125]. This relationship can be expressed as:

$$v > c/n \qquad \text{Equation 22}$$

where *c* is the speed of light and *n* is the refractive index of the sample [125]. When electrons are moving through the sample faster than light is moving through the sample, they will excite the atoms in the sample [125]. These excited atoms will then release excess energy in the form of Cherenkov radiation, which can result in the observation of

radiation losses in low-loss EELS spectra [125]. If a low-loss spectrum with Cherenkov losses is analyzed, inaccurate ε_1 and ε_2 spectra will be extracted. Thus, whenever possible, Cherenkov radiation should be avoided during the acquisition of low-loss EELS spectra.

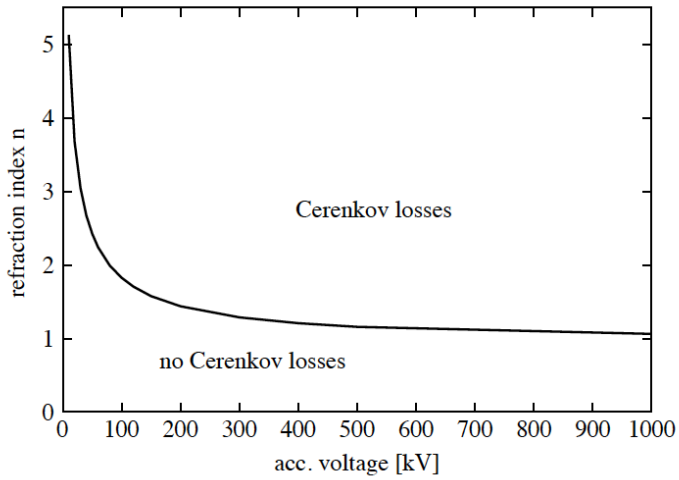

Figure 5.13: Depending on the refractive index of the sample and the accelerating voltage used during EELS measurements, Cherenkov radiation can be avoided. As shown in this plot, if an appropriate accelerating voltage is selected such that the intersection between the accelerating voltage and the sample's refractive index falls under the solid line, Cherenkov losses will not be observed in low-loss EELS spectra. This plot was originally published in reference [125].

It is possible to avoid the emission of Cherenkov radiation if the condition in Equation 22 is not satisfied; in other words, as long as the velocity of the electrons is less than the ratio of the speed of light to the sample's refractive index, Cherenkov radiation will not be emitted by the sample and Cherenkov losses will not be observed in the low-loss EELS spectrum. From this relationship, since the speed of light is constant, it is possible to determine the maximum accelerating voltage (which is related to the velocity

of the electrons) that will not result in the emission of Cherenkov radiation for specific values of refractive index, as shown in Figure 5.13 [125]. Thus, to avoid Cherenkov radiation for refractive indices in the range of 1.6 – 2.0, accelerating voltage less than 75 keV should be used (assuming $n = 2.0$, the upper limit). Even assuming that the refractive index is closer to $n = 1.6$, an accelerating voltage no greater than 150 keV should be used in collecting low-loss EELS spectra. Thus, by collecting data at 300 keV previously, it is extremely likely that Cherenkov losses were acquired in the spectra shown in Figure 5.12.

Since it was highly probable that Cherenkov losses were acquired in the $V[TCNE]_{x\sim2}$ low-loss spectra previously discussed, new EELS low-loss and core-loss spectrum images were collected using an FEI Titan^3 60-300 Image-Corrected S/TEM with a 60 keV monochromated electron beam (as opposed to the 300 keV monochromated electron beam used before). Since 60 keV falls below the Cherenkov radiation threshold for refractive indices between 1.6 and 2.0 (see Figure 5.13), Cherenkov losses should not be observed in the low-loss EELS spectra extracted from these spectrum images. Both the low-loss and core-loss EELS spectrum images were collected using an α (convergence angle) of 9.3 mrad, a β (collection angle) of 13.08 mrad, and an energy dispersion of 0.025 eV/channel. Furthermore, the low-loss spectrum images were acquired for energy-losses of -15 to 35 eV using a step size of 1.5 nm and an exposure time of 0.1 ms per pixel. Again, the CCD was set to 1x130 binning to increase the readout speed of the CCD. The core-loss spectrum image was collected for energy-losses of 500 to 550 eV using a step size of 5.9 nm and an exposure time of 20 ms. Since these low-loss and core-

loss spectra were also not acquired in dual-EELS mode, the low-loss spectrum image was collected first to ensure that any beam-damage that could affect the measured optoelectronic properties was minimized.

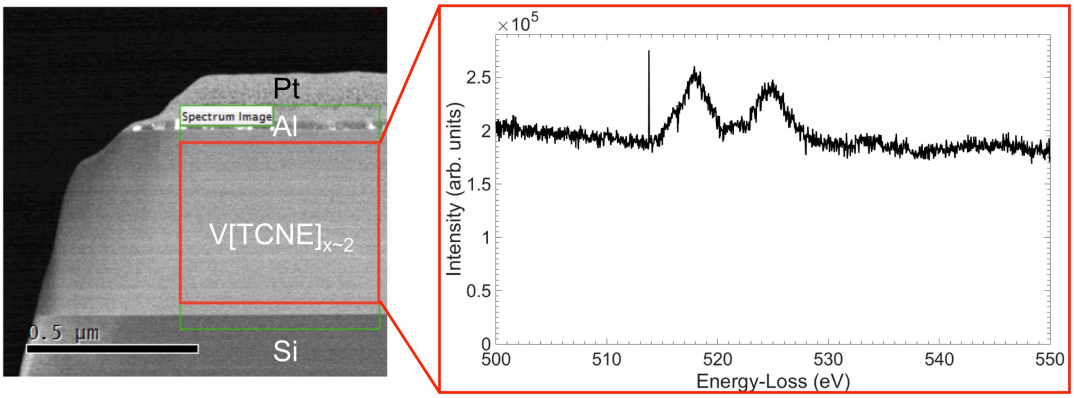

Figure 5.14: By summing all of the pixels included in the red box (left), the $V[TCNE]_{x\sim2}$ core-loss EELS spectrum was extracted (right). In this spectrum, there is a small bump at the oxygen-K edge (~532 eV).

From the core-loss spectrum image, 80 rows of 100 pixels (area of 472 nm by 590 nm) were summed together, resulting in the extracted core-loss EELS spectrum shown in Figure 5.14. Unfortunately, it does appear that there is a trace amount of oxygen present in the $V[TCNE]_{x\sim2}$ layer, as indicated by the small bump in the core-loss spectrum at ~532 eV (which corresponds to the oxygen-K edge [115]). This suggests that the $V[TCNE]_{x\sim2}$ was slightly oxidized during the sample preparation process; in other words, this sample spent too long out in the air during the sample preparation process. Although

the exact same process that was used to acquire the data shown in Figures 5.6 and 5.9 was used here, only this sample oxidized. It is entirely possible that the TEM sample loading process took slightly longer during the acquisition of the 60 keV data, which may explain why this sample oxidized. However, this proves that, while it is possible to prepare cross-sectional samples of $V[TCNE]_{x\sim2}$ thin films using the FIB sample preparation methods described in Section 5.1 without the samples oxidizing, the process is not entirely foolproof.

As this is the only 60 keV EELS data that has been collected thus far for $V[TCNE]_{x\sim2}$ thin films, the collected low-loss spectrum image was processed in order to obtain a representative low-loss spectrum and to extract the complex dielectric function. Nevertheless, in the future, 60 keV low-loss EELS spectrum images need to be reacquired for a cross-sectional $V[TCNE]_{x\sim2}$ sample that exhibits no signs of oxidation in order determine whether the low-loss spectra extracted from this oxidized sample are affected by the small amount of oxidation observed in Figure 5.14.

From the 60 keV low-loss spectrum image measured, a representative low-loss EELS spectrum was extracted. First, each pixel (spectrum) was calibrated by aligning the maximum of the zero-loss peak (ZLP, see Section 2.2.1.1) of each pixel to 0 eV. Then, pixels corresponding to an area of ~370 nm by ~560 nm were summed together to obtain the low-loss EELS spectrum shown in Figure 5.15. The ZLP was then subtracted from the low-loss spectrum via the reflected-tail method (Section 2.2.1.1), resulting in the inelastic spectrum shown.

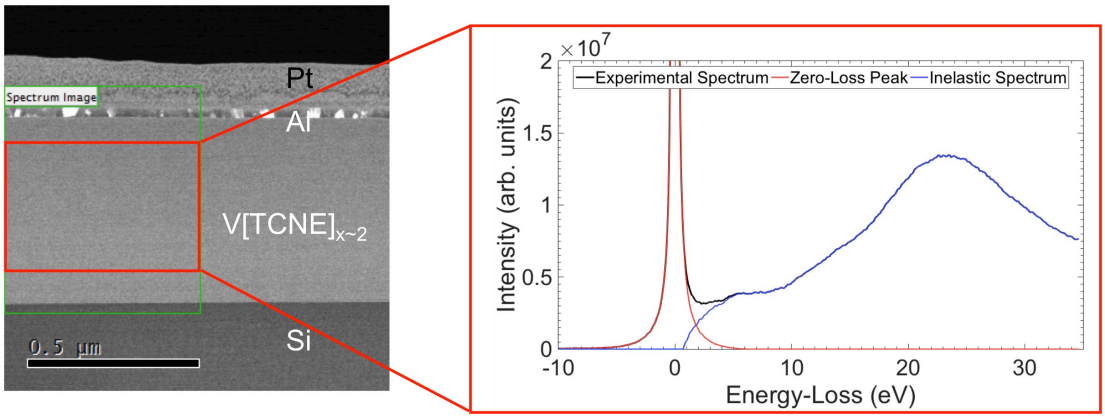

Figure 5.15: Low-loss EELS spectrum (right) obtained by summing pixels enclosed by the red box (left). This data was collected using a 60 keV monochromated electron beam. This acceleration voltage should prevent Cherenkov radiation from occurring. For the low-loss spectrum (right), the ZLP was subtracted from the experimental spectrum (black line) by using the reflected-tail method (red line). This resulted in the inelastic spectrum (blue line).

In comparing this inelastic spectrum to the ones previously obtained at 300 keV (Figure 5.12), it is obvious that there are numerous differences between the data sets collected using different accelerating voltages. For the inelastic spectra collected at 300 keV, there are multiple sharp peaks for energy-losses less than 6 eV. However, these are not observed at 60 keV. Since the two data sets were acquired using similar step sizes (300 keV = 0.83 nm, 60 keV = 1.5 nm) and identical exposure times (0.1 ms), it seems unlikely that this difference is entirely due to electron beam damage. It is possible that these differences in the inelastic spectra (60 keV vs. 300 keV) were caused by the slight oxidation of the 60 keV $V[TCNE]_{x\sim2}$ sample. However, since it is known that Cherenkov radiation will occur at 300 keV for materials with refractive indices in the range of 1.6 –

2.0, it seems much more likely that the sharp peaks observed in the 300 keV inelastic spectra were due to Cherenkov radiation. Moving forward, new data needs to be acquired at 60 keV from a sample that was not oxidized during the sample preparation, as only then will it be possible to attribute the lack of these peaks in the 60 keV to the avoidance of Cherenkov radiation rather than the oxidation of the sample. Furthermore, assuming that subsequent 60 keV low-loss EELS data sets of unoxidized $V[TCNE]_{x\sim2}$ samples are identical to the spectrum shown in Figure 5.15, this confirms that the refractive index of $V[TCNE]_{x\sim2}$ must be between 1.3 and 2.25 as these refractive indices would result in Cherenkov radiation at 300 keV but not at 60 keV (see Figure 5.13).

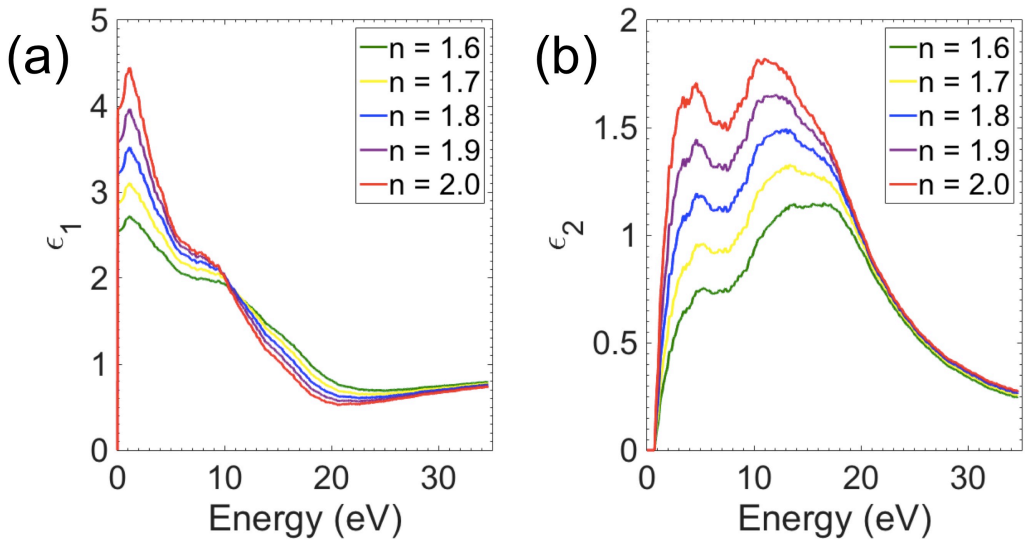

Figure 5.16: Comparisons of (a) ε_1 and (b) ε_2 spectra extracted from Kramers-Kronig analysis for different inputs of the refractive index (n = 1.6 to 2.0).

Preliminary spectra for the real (ε_1) and imaginary (ε_2) parts of the complex dielectric function were extracted for this 60 keV V[TCNE]$_{x\sim2}$ low-loss EELS spectrum. Since the ZLP had already been subtracted from the low-loss spectrum, Fourier-Log deconvolution was used to acquire the single scattering distribution (see Section 2.2.1.2). Next, Kramers-Kronig analysis was used to ε_1 and ε_2. As discussed both in Section 2.2.1.3 and previously in this section, the refractive index, *n*, is a required input for Kramers-Kronig analysis using the automated routine in DigitalMicrograph. Since comparisons to other organic semiconductors suggested that the refractive index of V[TCNE]$_{x\sim2}$ likely falls between 1.6 and 2.0, ε_1 and ε_2 spectra were collected using each of these values of refractive index in order to see if there was a significant difference in the extracted ε_1 and ε_2 spectra based on the refractive index used (Figure 5.16). These comparisons show that the features below 10 eV do not shift in energy as the refractive index varies; only the intensity changes, which makes sense as both ε_1 and ε_2 depend on the refractive index (see Equations 3 and 4). However, this demonstrates how, until a more precise value of the refractive index has been determined from V[TCNE]$_{x\sim2}$, it will be impossible to determine the absolute values of ε_1 and ε_2 via low-loss EELS measurements.

Figure 5.17a shows the ε_2 spectrum obtained for a refractive index of 2.0 for which. the energies of various features have been determined. As discussed in Section 2.2.1.3, the energies of these features should correspond to specific single electron transitions from the valence band to the conduction band. Fortunately, the energies of many of these transitions between electronic states have been identified for V[TCNE]$_{x\sim2}$, as shown in Figure 5.17b (adapted from references [49,52], and discussed in Section 1.2.1.1). Thus, it

should be possible to identify which single electron transitions are observed in this experimental ε_2 spectrum.

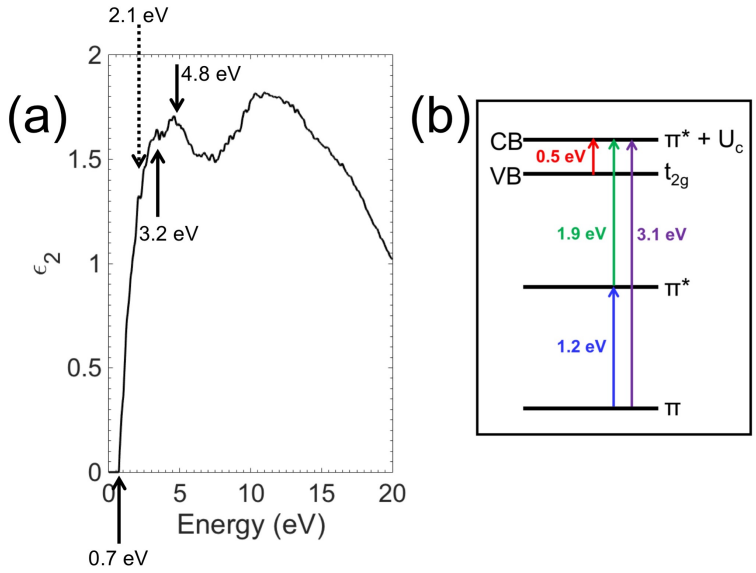

Figure 5.17: (a) Experimental ε_2 spectrum obtained from the 60 keV measurements for $V[TCNE]_{x\sim2}$. A refractive index of 2.0 was used to extract this spectrum via Kramers-Kronig analysis. (b) Known electron transitions as identified in the literature [49,52]. The π and π^* states are attributed to the $[TCNE]^-$ molecule, and the t_{2g} state is attributed to the V^{2+} ions.

For instance, there is a peak in the experimental ε_2 spectrum ~3.2 eV, which likely corresponds to a single electron transition from the π molecular orbital of the $[TCNE]^-$ molecule to the π^*+U_c molecular orbital of the $[TCNE]^-$ molecule [52]. There may also be another peak at ~2.1 eV, which is similar to the expected value of 1.9 eV [52] or 2.0 eV [49] that is expected for the Coulombic repulsion energy, U_c, that separates the split π^* orbitals of the $[TCNE]^-$ molecule. However, it is not entirely clear from this

experimental ε_2 spectrum if this small peak is indicative of a single electron transition or if it is actually due to noise in the spectrum, and the acquisition of new 60 keV data should help clarify whether this feature is an actual peak or not. Additionally, there is a transition at ~4.8 eV in the experimental ε_2 spectrum that has not yet been identified in the literature.

Lastly, the onset of the ε_2 spectrum, which should correspond to the bandgap of the material as this onset represents the energy at which the extinction coefficient, *k(E)*, is first nonzero, is at ~0.7 eV. This value is similar to the expected bandgap of ~0.5 eV for $V[TCNE]_{x\sim2}$ [49,50,52]. However, because of the subjectivity introduced during the removal of the zero-loss peak (Section 2.2.1.1), it is difficult to precisely measure the bandgap of low bandgap materials, and this value of 0.7 eV should not be taken as an absolute measure of the bandgap of $V[TCNE]_{x\sim2}$. Nevertheless, this onset does support previous statements claiming that the bandgap of $V[TCNE]_{x\sim2}$ is less than 1 eV.

5.5. Summary

EELS data was collected and analyzed for $V[TCNE]_{x\sim2}$, an organic-based ferrimagnetic semiconductor. While the sample preparation methods for these measurements were non-trivial, it was proven that, with enough care, oxidation of this highly air-sensitive $V[TCNE]_{x\sim2}$ film could be avoided. These EELS measurements were the first in which data about $V[TCNE]_{x\sim2}$ thin films have been measured with high spatial

resolution, as historically only bulk techniques have been used due to the air-sensitivity of $V[TCNE]_{x\sim2}$.

First, core-loss EELS data was analyzed to determine the oxidation state of the vanadium ions in the $V[TCNE]_{x\sim2}$ compound and to determine if this oxidation state varied throughout the $V[TCNE]_{x\sim2}$ thin film. From this analysis, the oxidation state was determined to be closest to V^{2+}, which was consistent with previous measurements available in the literature. However, by spatially tracking the vanadium oxidation state in ~18 nm steps from the top to the bottom of the $V[TCNE]_{x\sim2}$ thin film, it was proven, for the first time, that the oxidation state of the vanadium ions does not vary throughout the thin film.

Comparisons of this core-loss EELS data to previously reported XANES data revealed differences in the shape of the V-L_2 peak. In the EELS data, only a single V-L_2 peak was observed whereas a doublet structure was detected in the XANES measurements. Computer simulations prove that the energy resolution of the EELS data should not prevent the detection of this doublet structure, and future measurements are necessary in order to try and determine why exactly this discrepancy between the EELS and XANES $V[TCNE]_{x\sim2}$ data is observed.

Low-loss EELS data was also collected and analyzed using both a 300 keV and 60 keV electron beam. Since the refractive index of $V[TCNE]_{x\sim2}$ is suspected to be between 1.6 and 2.0, the 300 keV data was dismissed due to the high likelihood that Cherenkov losses were acquired. However, the sample used in the acquisition of the 60 keV data (for which Cherenkov radiation was avoided) showed signs of oxidation. Since this was the

only sample for which 60 keV low-loss EELS data has been collected, currently, the complex dielectric function was extracted, and peaks in the extracted ε_2 spectrum were correlated to known single electron transitions. Moving forward, new 60 keV low-loss EELS data needs to be acquired and analyzed in order to unequivocally prove that the extracted complex dielectric function showed here is actually representative of pure $V[TCNE]_{x\sim2}$.

Overall, these experiments demonstrate how, if proper care is taken, it is possible to collect reliable EELS data for air-sensitive samples.

Chapter 6. EELS of Lead-Free Halide Double Perovskites

As discussed in Section 1.2.2, lead-free halide double perovskites have emerged as a promising replacement for organometal trihalide perovskites for the use in solar cells. These lead-free halide double perovskites exhibit similar percent reflectances and bandgaps as their organometal trihalide perovskite counterparts, and the elimination of lead from the chemical compound eliminates some of the environmental concerns currently associated with perovskite solar cells [64]. However, the optoelectronic properties, such as the complex dielectric function (Equation 1) and complex refractive index (Equation 2), of these lead-free halide double perovskites have not yet been determined, thus limiting the complete understanding of these materials.

Researchers at The Ohio State University have developed various lead-free halide double perovskites, two of which – $Cs_2AgBiBr_6$ and $Cs_2AgBiCl_6$ – were studied using STEM-EELS in an effort to extract these optoelectronic properties. By utilizing STEM-EELS (see Section 2.1) for these preliminary measurements, the energy range of the entire solar spectrum could be studied. Furthermore, as spatially-resolved measurements of the optoelectronic properties can be obtained via STEM-EELS, these measurements lay the groundwork for the future study of solar cells in which these materials are utilized.

6.1. Obtaining the Complex Dielectric Function via VASE

Before collecting EELS data for $Cs_2AgBiBr_6$ and $Cs_2AgBiCl_6$, variable angle spectroscopic ellipsometry (VASE) was used to determine the energy-dependent refractive indices and extinction coefficients for these two materials. A brief overview of spectroscopic ellipsometry is given in Section 2.3.

As mentioned before, the optoelectronic properties, including the complex refractive index, have not been determined for $Cs_2AgBiBr_6$ and $Cs_2AgBiCl_6$. However, to extract the optoelectronic properties from EELS data, the refractive index is needed to perform Kramers-Kronig analysis (as discussed in Section 2.2.1.3). Thus, by first conducting VASE measurements on these samples, an approximation of the refractive index could be determined.

The $Cs_2AgBiBr_6$ and $Cs_2AgBiCl_6$ samples studied were bulk crystals on the order of approximately 1 - 5 mm^3, and the growth of these crystals has been described in reference [64]. The crystals were used as-grown for these VASE measurements. A J.A. Woolam Variable Angle Spectroscopic Ellipsometer was used to collect the VASE data, and values of psi, Ψ, and delta, Δ, were collected for incident angles of 55°, 60°, and 65°, over the energy range of 0.6-4.3 eV (acquired in 0.01 eV steps). Due to the small size of some of these crystals, a focusing probe attachment was utilized during these measurements.

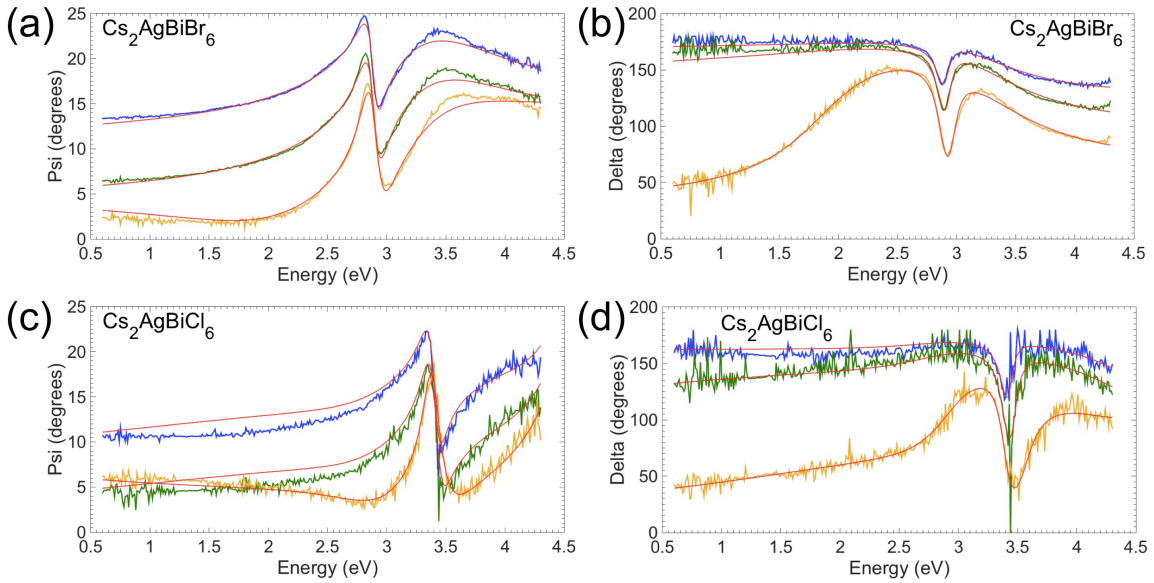

Figure 6.1: Collected VASE data for (a) – (b) $Cs_2AgBiBr_6$ and (c) – (d) $Cs_2AgBiCl_6$. The red lines denote the models built using critical points, and the data was collected for 55° (blue lines), 60° (green lines), and 65° (yellow lines). The models built closely match the experimental Ψ and Δ data, suggesting that the extracted values of *n* and *k* should be accurate.

The collected VASE data, along with the built models, are shown in Figure 6.1 for $Cs_2AgBiBr_6$ and $Cs_2AgBiCl_6$. Originally, these data were modeled using harmonic oscillators, similar to the approach used in Section 3.2.2 for organic photovoltaic materials (CuPc, C_{60}, P3HT, and PCBM). However, previous reports of spectroscopic ellipsometry measurements made for organometal trihalide perovskites ($MAPbBr_3$ and $MAPbCl_3$, MA = methylammonium) utilized standard critical point (SCP) oscillators instead [126]. The rationale given for using SCP oscillators instead of using the harmonic oscillator approach (HOA) was that SCP oscillators allow for asymmetric electronic transitions to be described uniquely by only one oscillator, whereas the HOA requires an

oscillator with a negative amplitude to offset any asymmetry in the transition [126]. Thus, using the HOA for these materials could result in extra oscillators that are not defining real transitions in the data [126]. Since it was expected that the lead-free halide double perovskites should behave similarly to these organometal trihalide perovskites, the VASE data were remodeled using multiple critical point parabolic band (CPPB) oscillators, resulting in the models shown by the red lines in Figure 6.1. These oscillators were each of the form:

$$Ae^{(i\varphi)}\left(\frac{\Gamma}{2E_n-2E-i\Gamma}\right)^{\mu} \qquad \text{Equation 23}$$

where A was the amplitude of the oscillator, φ was the phase of the oscillator, **Γ** was the broadening of the oscillator, E_n was the energy center of the oscillator [126]. Similar to the modeling conducted for the organometal trihalide perovskites, the value of dimensionality, μ, was set to be a constant value of 1 (correlating to critical points of zero-dimensionality) [126]. After building the models, a mean-squared error minimization was used to adjust the parameters of the models to best fit the experimental tan(Ψ) and cos(Δ) data, resulting in the parameters listed in Tables 6.1 and 6.2 for $Cs_2AgBiBr_6$ and $Cs_2AgBiCl_6$, respectively.

Table 6.1: Values of the critical point parabolic band (CPPB) oscillators used in modeling the $Cs_2AgBiBr_6$ VASE data.

CPPB	Amplitude (no units)	Energy Center (eV)	Broadening (eV)	Phase (no units)
1	657.08	9.9429	0.088573	174.48
2	4.9684	2.836	0.16999	34.912
3	60.253	15.683	2.7722	1.1904
4	4.1531	3.2283	0.89679	-54.457

Table 6.2: Values of the critical point parabolic band (CPPB) oscillators used in modeling the $Cs_2AgBiCl_6$ VASE data.

CPPB	Amplitude (no units)	Energy Center (eV)	Broadening (eV)	Phase (no units)
1	6745.5	4.8087	0.000827	150.96
2	1.1936	3.1595	1.5111	174.48
3	4.0516	3.348	0.15672	34.912
4	35.451	7.3358	1.2715	1.1904

As these SCP models compare favorably with the collected VASE data (red lines in Figure 6.1), values of *n(E)* and *k(E)* were extracted (Figure 6.2). From these spectra, approximations of the refractive index were made for both $Cs_2AgBiBr_6$ and $Cs_2AgBiCl_6$, resulting in a refractive index of $n = 2.0$ for $Cs_2AgBiBr_6$ and $n = 1.8$ for $Cs_2AgBiCl_6$. Based on these estimates of the refractive indices, an accelerating voltage of 60 keV should be used in the acquisition of the experimental EELS data in order to avoid Cherenkov radiation (see Section 5.4 for the discussion of Cherenkov radiation).

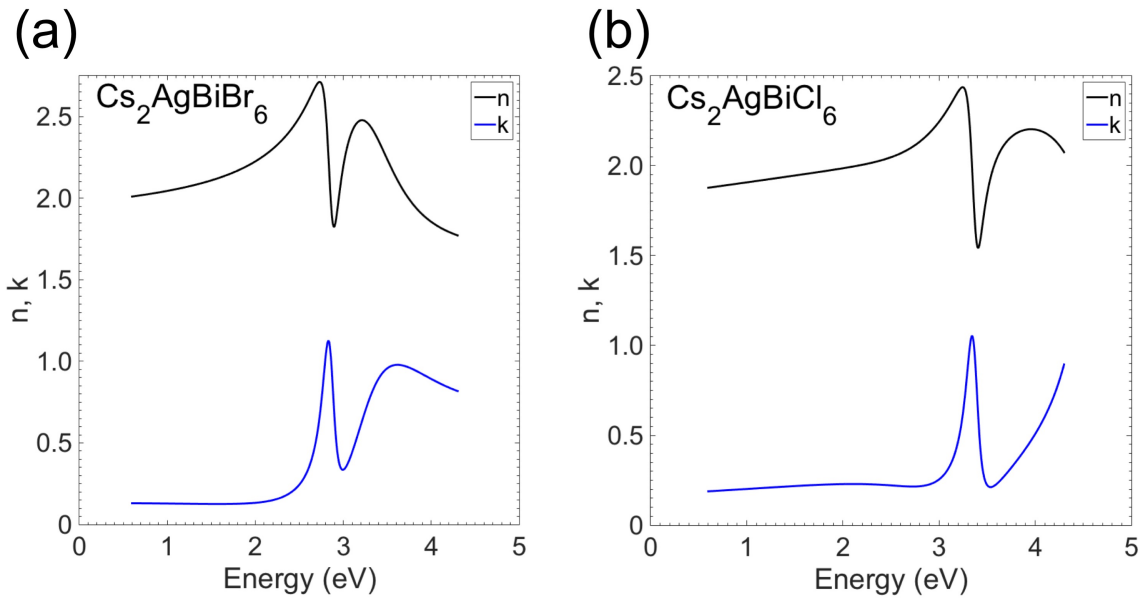

Figure 6.2: *n(E)* (shown in black) and *k(E)* (shown in blue) spectra obtained for (a) $Cs_2AgBiBr_6$ and (b) $Cs_2AgBiCl_6$ as obtained via VASE measurements on bulk crystals of these materials.

6.2. Obtaining the Complex Dielectric Function via EELS

Having determined approximations of the refractive indices of $Cs_2AgBiBr_6$ and $Cs_2AgBiCl_6$, electronic energy-loss spectroscopy (EELS) measurements via a scanning transmission electron microscope (STEM) were made in order to extract the optoelectronic properties. First, TEM samples of the $Cs_2AgBiBr_6$ and $Cs_2AgBiCl_6$ crystals were prepared by grinding the crystals with a mortar and pestle and then dipping a lacey-carbon TEM copper grid into the resulting powder. This transferred small crystallites from the powder onto to the lacey-carbon TEM copper grids. Lacey-carbon TEM copper grids were used in the hopes that some of the crystallites from the powders

would protrude over holes in the lacey-carbon film, thus eliminating any carbon signal from the EELS acquisitions. Since solar perovskites are known to degrade, and previous diffuse reflectance measurements proved that $Cs_2AgBiBr_6$ will degrade when exposed to light and air [64], the $Cs_2AgBiBr_6$ and $Cs_2AgBiCl_6$ crystals samples were stored in a glovebox until they were removed to prepare EELS samples (as described previously), immediately after which the EELS measurements were made.

Low-loss EELS data was collected for these powders by using a monochromated 60 keV electron beam in an FEI Titan^3 60-300 Image-Corrected S/TEM outfitted with a Gatan Quantum spectrometer. Since the refractive index of $Cs_2AgBiBr_6$ was determined to be ~2.0 and the refractive index of $Cs_2AgBiCl_6$ was determined to be ~1.8 from the variable-angle spectroscopic ellipsometry measurements (Section 6.1), an accelerating voltage of 60 keV was selected in order to avoid Cherenkov radiation (see Section 5.4 for the discussion of Cherenkov radiation).

These low-loss EELS spectra were acquired using the method of spectrum imaging (see Section 4.1.1). By using spectrum imaging, spatially-resolvable EELS data could be collected since three-dimensional data sets in which both the low-loss EELS spectrum and the area from which it came are saved [65,66,73]. The low-loss spectrum images were collected for energy-losses less than 40 eV. Because there were indications that the $Cs_2AgBiBr_6$ and $Cs_2AgBiCl_6$ low-loss spectra changed (loss of fine structure) if the samples were exposed to a high electron dose, samples were minimally exposed to the electron beam before the EELS acquisitions (similar to the methods described in Section 4.1.1). Unfortunately, since these samples were not continuous films (as in the case of

the organic photovoltaics studied in Chapters 3 and 4 or the organic-based ferrimagnetic semiconductor studied in Chapter 5), it was necessary to expose these samples to the electron beam prior to the EELS acquisitions in order to find suitable areas from which to collect the EELS spectrum images. The areas selected were relatively thin areas of the samples in order to (1) to reduce plural scattering effects (Section 2.2.1.2), and (2) prevent diffraction artifacts from appearing in the data sets. If the area from which EELS data was collected was too thick, diffraction artifacts, such as sharp peaks on the energy-gain (left) side of the ZLP were observed, which were due to Bragg reflections entering the spectrometer [66]. The specific steps sizes, exposure times, convergence angles, and collection angles used during the acquisitions of the $Cs_2AgBiBr_6$ and $Cs_2AgBiCl_6$ low-loss spectrum images collected will be outlined in the following paragraphs.

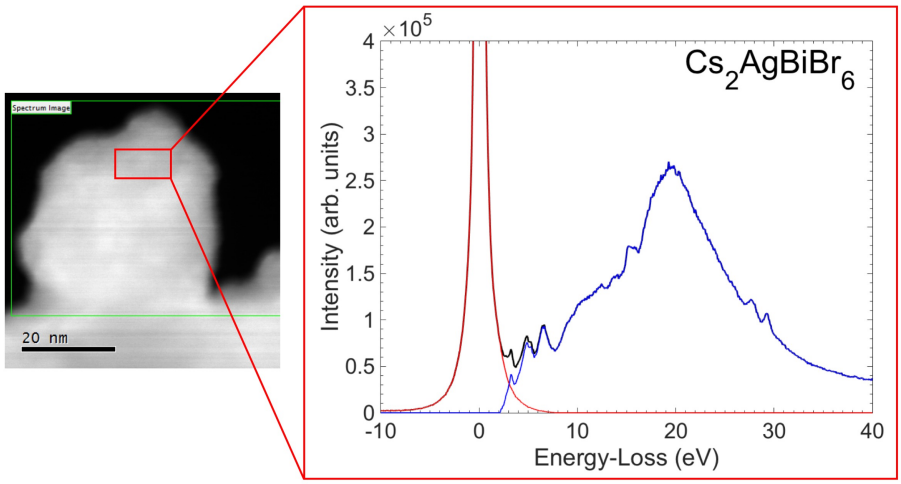

Figure 6.3: Low-loss spectrum (right) collected for $Cs_2AgBiBr_6$ by summing the pixels shown in the red box for the HAADF image shown (left). From the low-loss spectrum (black line), the ZLP (red line) has been modeled using the reflected-tail method. When the ZLP has been subtracted from the spectrum, all that remains is the inelastic spectrum (blue line), which consists of both plural and single scattering events.

Low-loss EELS data was collected for $Cs_2AgBiBr_6$ using an α (convergence angle) of 9.3 mrad and a β (collection angle) of 13.08 mrad. A larger value of β than α was used to ensure that all of the signal from the transmitted electron beam was collected. The low-loss spectrum image was collected for energy-losses of -10 to 40 eV (energy dispersion = 0.025 eV/channel) with a step size of 0.29 nm and an exposure time of 5 ms.

In order to extract a representative low-loss spectrum from the spectrum image, each pixel (spectrum) was first calibrated so that the maxima of the zero-loss peaks (ZLPs, see Section 2.2.1.1) were set at 0 eV for every pixel (spectrum). Then pixels corresponding to the area of 6.1 nm by 11.9 nm were summed together to extract the spectrum shown in Figure 6.3 (energy resolution = 0.25 eV). Data was extracted from this region of the sample because the thickness of the sample was relatively constant throughout this area of the sample. This is important because many of the calculations used in processing EELS data assume that the sample's thickness is constant, such as deconvolution of the inelastic spectrum (see Section 2.2.1.2). The ZLP was then removed from this extracted low-loss spectrum using the reflected-tail method (see Section 2.2.1.1).

The data collected for $Cs_2AgBiCl_6$ was analyzed in a similar manner to remove the ZLP from the low-loss spectrum. This data was also acquired with a convergence angle (α) of 9.3 mrad and a collection angle (β) of 13.08 mrad. The low-loss spectrum image was collected for energy-losses of -10 to 40 eV (energy dispersion = 0.025 eV/channel) with a step size of 0.32 nm and an exposure time of 5 ms. Again, each pixel (spectrum) was calibrated so that the ZLP maxima was set to 0 eV for every pixel. Pixels corresponding to the area of 8.96 nm by 6.08 nm were then summed together to extract

the spectrum shown in Figure 6.4 (energy resolution = 0.28 eV), and the ZLP was removed using the reflected-tail method. Although excess signal was observed for energy-losses less than the first primary low-loss peak (at ~3 eV), suggesting that the ZLP subtraction process was inaccurate, when larger values of the reflected-tail cutoff value were used to subtract the ZLP from this low-loss spectrum, kinks at the splicing point of the experimental ZLP and the reflected tail were observed (similar to the effect observed in the $V[TCNE]_{x\sim2}$ data - see Figure 5.11a). Thus, this signal is most likely attributable to sub-bandgap defect states, but more measurements are necessary to prove this.

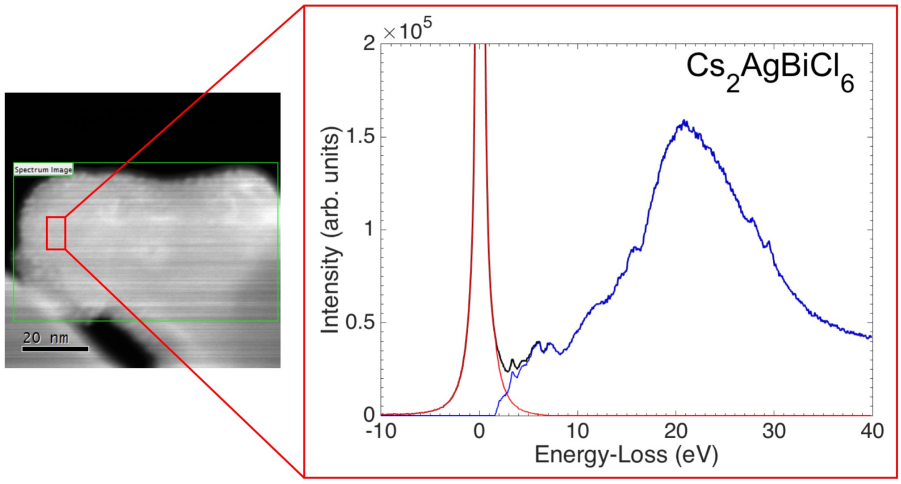

Figure 6.4: Low-loss spectrum (right) collected for $Cs_2AgBiCl_6$ by summing the pixels shown in the red box for the HAADF image shown (left). From the low-loss spectrum (black line), the ZLP (red line) has been modeled using the reflected-tail method. When the ZLP has been subtracted from the spectrum, all that remains is the inelastic spectrum (blue line), which consists of both plural and single scattering events.

In examining both low-loss spectra (Figures 6.3 and 6.4), it is encouraging to see multiple features for energy-losses less than 10 eV, as these features likely correspond to single electron transitions for these materials. Additionally, the features observed beyond the plasmon peak at ~28 and ~30 eV are identifiable as the $O_{4,5}$-edge for bismuth [127].

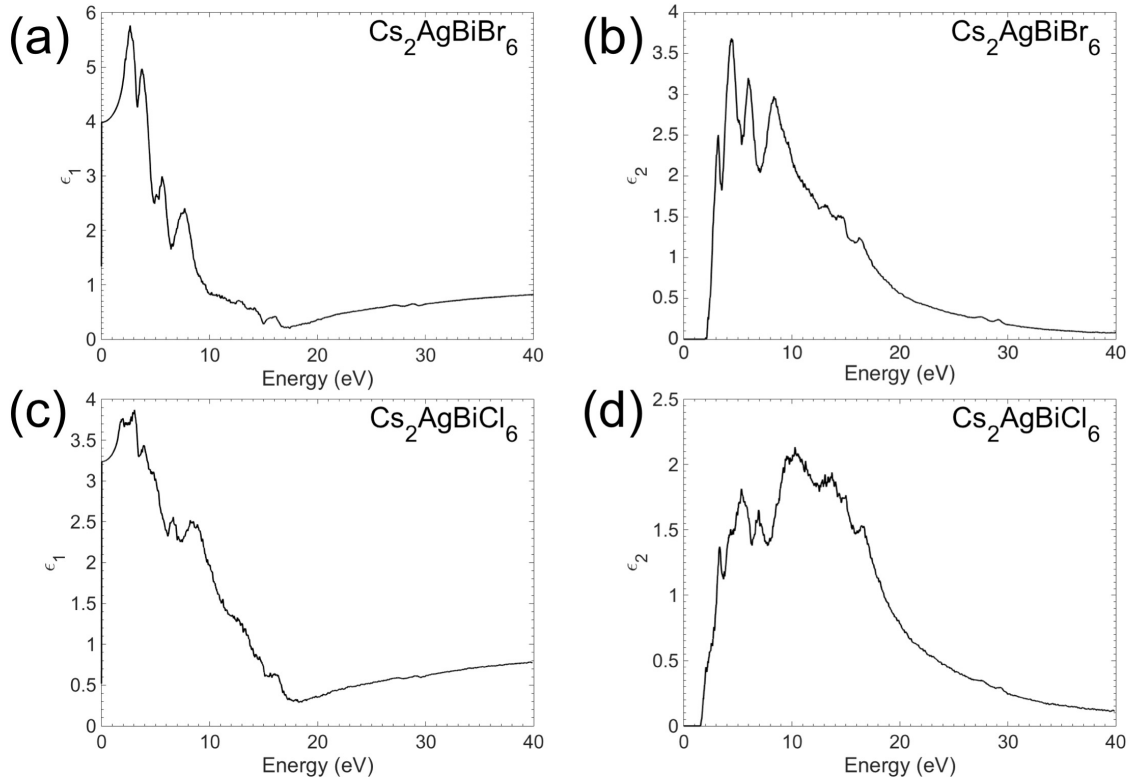

Figure 6.5: ε_1 and ε_2 spectra calculated from low-loss EELS measurements for (a and b) $Cs_2AgBiBr_6$ and (c and d) $Cs_2AgBiCl_6$.

To extract the optoelectronic properties for each of these materials, Kramers-Kronig analysis (see Section 2.2.1.3) was used via the automated routine available in

DigitalMicrograph. Values of n = 2.0 ($Cs_2AgBiBr_6$) and n = 1.8 ($Cs_2AgBiCl_6$) were used for these refractive indices of these materials, as determined from the VASE measurements (see Section 6.1), and the resulting ε_1 and ε_2 spectra are shown in Figure 6.5.

In both ε_2 spectra shown in Figure 6.5, many peaks are observed, especially for energies corresponding to the solar spectrum (less than ~7 eV). These peaks should correlate to single electron transitions from the valence band to the conduction band (as discussed in Section 2.2.1.3). Unfortunately, at the writing of this dissertation, the single electron transitions for these materials have not been identified in the literature, and it was beyond the scope of this work to determine them. Thus, it is currently not possible to correlate these peaks in ε_2 to specific single electron transitions. However, once the possible single electron transitions have been identified for $Cs_2AgBiBr_6$ and $Cs_2AgBiCl_6$, it should be relatively simple to correlate the peaks in these ε_2 spectra to the known single electron transitions.

Although the single electron transitions for $Cs_2AgBiBr_6$ and $Cs_2AgBiCl_6$ have not been identified in the literature, it was possible to compare the ε_2 spectra obtained for $Cs_2AgBiBr_6$ and $Cs_2AgBiCl_6$ from EELS to ε_2 data calculated using density functional theory (DFT) computations completed by collaborators at The Ohio State University. These computations do not take into account any possible excitonic effects, which could be significant because low-loss peaks due to excitons have been well-documented for alkali halides [66], although it is unclear at this point how much of an affect excitonic transitions are having on these data.

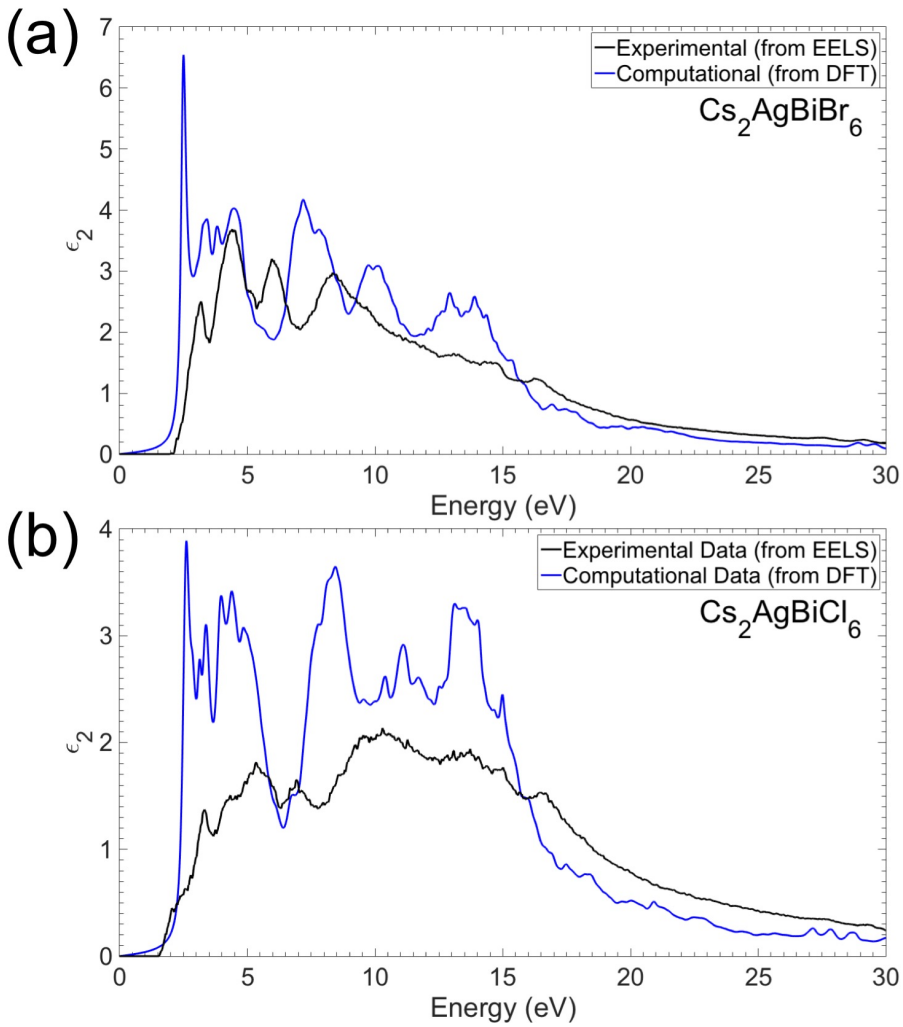

Figure 6.6: Comparisons of the ε_2 spectra collected via EELS (black lines) and calculated via DFT (blue lines) for (a) $Cs_2AgBiBr_6$ and (b) $Cs_2AgBiCl_6$. The EELS and DFT spectra share similar features, but the energies of those features in the DFT ε_2 spectra are shifted to lower energies for both materials.

Comparisons of these ε_2 spectra are shown in Figure 6.6, in which the EELS ε_2 spectra are shown in black and the DFT ε_2 spectra are shown in blue. In comparing these

ε_2 spectra for both materials, it appears that the number of features and relative shapes of those features are quite similar between the EELS and the DFT ε_2 spectra. However, these features seem to be shifted to lower energies in the DFT ε_2 spectra, as compared to the EELS ε_2 spectra. For instance, in the $Cs_2AgBiBr_6$ ε_2 spectra (shown in Figure 6.6a), there are four peaks in the EELS ε_2 spectrum prior to the double peak at ~8.5 – 9.5 eV. Similarly, in the DFT ε_2 spectrum there are also four peaks prior to a double peak of similar shape. The only difference is that the double peak in the DFT ε_2 spectrum is at ~7 – 8 eV. Similar observations can be made for the $Cs_2AgBiCl_6$ ε_2 spectra.

Generally, for the Perdew-Burke-Ernzerhof (PBE) functional theory used in the DFT-calculations performed by collaborators, the calculated energies of unoccupied states are considered to be unreliable, especially for energies further away from the Fermi level. Thus, an attempt to correlate the DFT ε_2 data with the EELS ε_2 data was made by adjusting the DFT ε_2 data to match the EELS ε_2 data. Based on the relative shapes of the features in the DFT ε_2 spectra as compared to the EELS ε_2 spectra, peaks from each method were correlated to each other (i.e. peaks in the $Cs_2AgBiCl_6$ and $Cs_2AgBiBr_6$ DFT ε_2 spectra were correlated to peaks in the $Cs_2AgBiCl_6$ and $Cs_2AgBiBr_6$ EELS ε_2 spectra). For instance, in the example given above, the third peak in the DFT ε_2 spectrum for $Cs_2AgBiBr_6$ at ~3.8 eV was correlated to the third peak in the EELS ε_2 spectrum at ~5.2 eV. These correlations are detailed in Tables 6.3 and 6.4 for $Cs_2AgBiBr_6$ and $Cs_2AgBiCl_6$, respectively.

Table 6.3: Correlations made between the energies of peaks in the EELS ε_2 spectra and the DFT ε_2 spectra for $Cs_2AgBiBr_6$.

$Cs_2AgBiBr_6$		
Peak Number	Energy in EELS ε_2 Spectrum	Energy in DFT ε_2 Spectrum
1	3.2	2.5
2	4.6	3.4
3	5.3	3.9
4	6.1	4.5
5	8.5	7.8
6	13.4	9.8
7	14.8	10.1
8	27.5	17.5
9	29.4	20.0

Table 6.4: Correlations made between the energies of peaks in the EELS ε_2 spectra and the DFT ε_2 spectra for $Cs_2AgBiCl_6$.

$Cs_2AgBiCl_6$		
Peak Number	Energy in EELS ε_2 Spectrum	Energy in DFT ε_2 Spectrum
1	3.4	2.6
2	4.1	3.1
3	4.5	3.4
4	5.5	4.0
5	6.0	4.4
6	7.1	4.8
7	8.6	6.75
8	9.8	7.75
9	10.6	8.3
10	13.5	11.0
11	15.0	13.5
12	16.5	15.0
13	27.75	18.5

Using these values, functions of various types were fitted to each data set in an effort to extract an equation relating the energies of the peaks in the DFT ε_2 spectra to the

energies of peaks in the EELS ε_2 spectra for both $Cs_2AgBiBr_6$ and $Cs_2AgBiCl_6$. A simple linear function was deemed inappropriate because, as mentioned before, the unreliability in the DFT-calculated energies of unoccupied states increases the further away the energies are from the Fermi level. Ultimately, it was determined that a power law was most suited to fitting these data sets, which resulted in functions of the forms:

$$f(E_{DFT}) = 1.1964(E_{DFT})^{1.0665} \quad \text{Equation 24}$$

$$f(E_{DFT}) = 1.4305(E_{DFT})^{0.9479} \quad \text{Equation 25}$$

for $Cs_2AgBiBr_6$ (Equation 24) and $Cs_2AgBiCl_6$ (Equation 25), where E_{DFT} is the original energy from the DFT-calculated ε_2 spectrum.

Having related the DFT-calculated energies to the EELS energies for the peaks in the ε_2 spectra, Equations 24 and 25 were used to adjust the DFT-calculated ε_2 spectra. Comparisons of the EELS ε_2 spectra and the DFT-adjusted ε_2 spectra are shown in Figure 6.7 for energies less than 8 eV, as it is this energy range that is of most interest as it corresponds to the solar spectrum (comparisons covering the entire EELS energy range can be found in Appendix B).

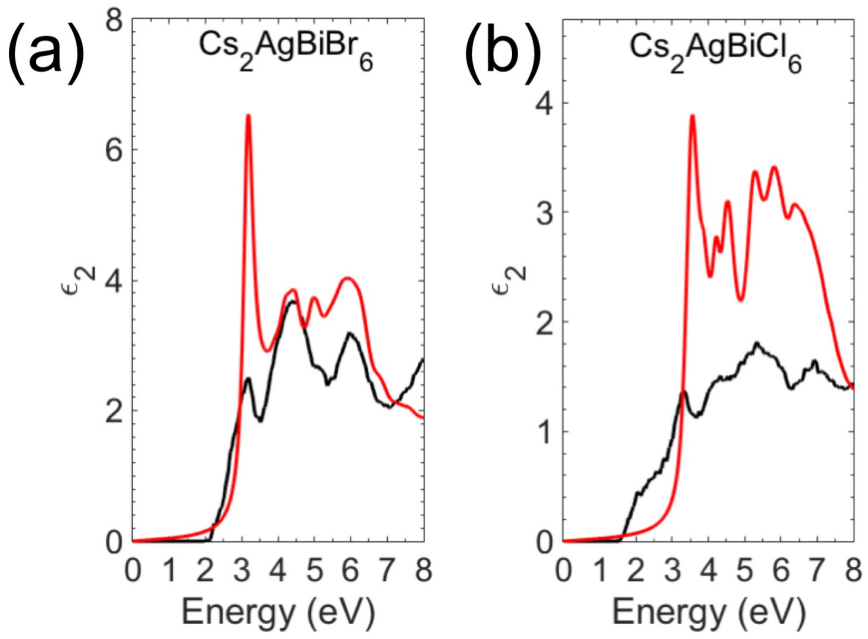

Figure 6.7: Comparisons of the ε_2 spectra from EELS (black lines) and from the DFT-adjusted calculations (red lines) for (a) $Cs_2AgBiBr_6$ and (b) $Cs_2AgBiCl_6$. Energies less than 8 eV are shown here, as this energy range encompasses the solar spectrum. Correlations for the entire EELS energy range can be found in Appendix B.

For the $Cs_2AgBiBr_6$ ε_2 spectra (Figure 6.7a), the first four peaks in the EELS ε_2 spectrum correlate well with the first four peaks in the DFT-adjusted ε_2 spectrum, which suggests that all of the single electron transitions for this energy range have been detected via these EELS measurements. However, in the $Cs_2AgBiCl_6$ ε2 spectra (Figure 6.7b), certain features observed in the DFT-adjusted ε_2 spectrum are not observed in the EELS ε_2 spectrum. For instance, based on the DFT-adjusted ε_2 spectrum, there should be two distinct peaks at ~4.4 and ~4.6 eV, but only one broad peak is observed in the EELS ε_2 spectrum. Since these peaks are separated by approximately 0.2 eV, the energy resolution of the EELS data set would need to better than 0.2 eV in order to resolve these two peaks.

However, the energy resolution of the spectrum obtained by summing pixels in the $Cs_2AgBiCl_6$ low-loss EELS spectrum image was only 0.28 eV. Thus, low-loss EELS data should be recollected with an energy resolution better than 0.2 eV for $Cs_2AgBiCl_6$ in order to conclude whether or not these two features (single electron transitions) in the DFT-adjusted ε_2 spectrum can be determined from low-loss EELS measurements. Collecting EELS data at a higher energy resolution should also have the added benefit of resulting in more distinction in the features at ~5.4 eV and ~5.9 eV in the $Cs_2AgBiCl_6$ EELS ε_2 spectrum (currently, the second feature appears as a shoulder of the first feature). Higher resolution EELS data would also lead to a better correlation between the DFT and EELS $Cs_2AgBiCl_6$ ε_2 spectra, as it would be easier to associate peaks in the EELS ε_2 spectrum to peaks in the DFT ε_2 spectrum.

6.3. Comparing Absorption Coefficient Spectra

Since the optoelectronic properties of each of $Cs_2AgBiBr_6$ and $Cs_2AgBiCl_6$ were determined via both VASE (Section 6.1) and EELS (Section 6.2), it was possible to extract the absorption coefficient spectra for each technique. For the VASE data, the absorption coefficient spectra were obtained using $\alpha(E) = 4\pi k/\lambda$, since values of the energy-dependent extinction coefficient were determined (Figure 6.2). For the EELS data, the absorption coefficient spectra were obtained using Equation 21. Comparisons of these extracted absorption coefficient spectra are shown in Figure 6.8a for $Cs_2AgBiCl_6$.

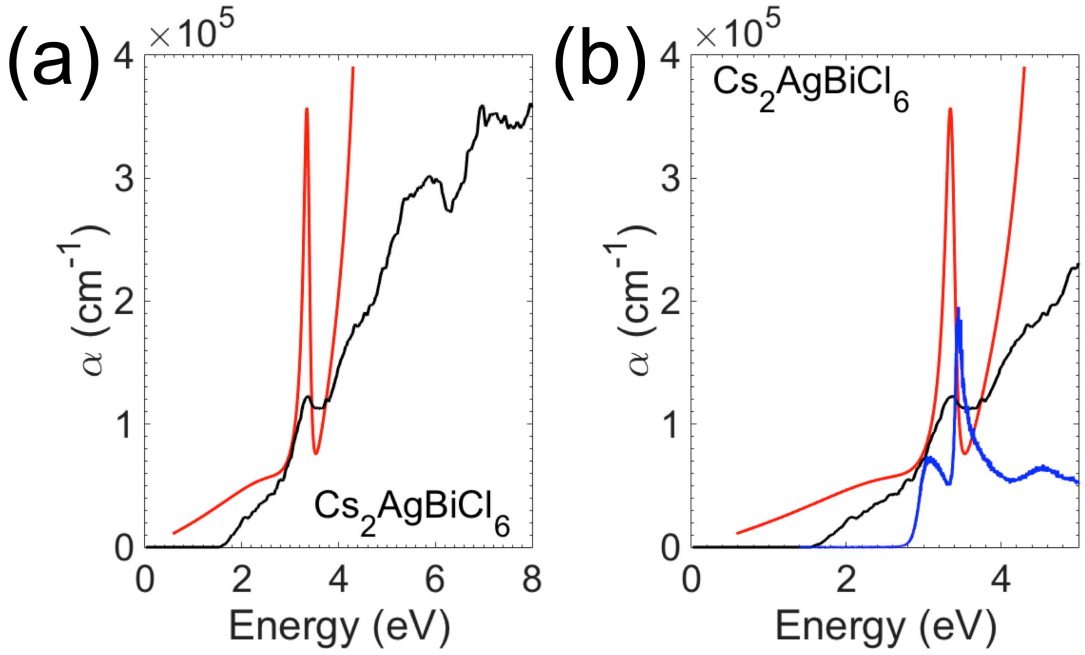

Figure 6.8: (a) Comparison of the absorption coefficient spectra obtained from EELS (black) and VASE (red) for $Cs_2AgBiCl_6$. (b) Comparison of the absorption coefficient spectra obtained from EELS (black), VASE (red), and diffuse reflectance via the Kubelka-Munk calculations (blue) for $Cs_2AgBiCl_6$. The diffuse reflectance-derived data is from reference [64]. This data was of arbitrary units and was scaled by 10,000 to be on the same scale as the VASE and EELS data.

Because of the limited energy range of the VASE data, only one peak is observed in the VASE-derived absorption coefficient spectrum. However, this peak agrees well in energy with a peak in the EELS-derived absorption coefficient spectrum. Furthermore, these two absorption coefficient spectra were compared to data obtained from diffuse reflectance (DR) measurements as reported in reference [64]. The Kubelka-Munk relationship was used to transform the raw DR data into a pseudo-absorbance spectrum [64], which is shown in Figure 6.8b, along with the VASE- and EELS-derived absorption coefficient spectra. Because the DR-derived data is of the pseudo-absorbance and not the

absorption coefficient spectrum, it was given in arbitrary units, and the values required a scalar of 10,000 to be on the same intensity scale as the VASE- and EELS-derived data.

In comparing the DR-derived data to the VASE- and EELS-derived data, it is interesting that the first two peaks in the DR-derived data appear to overlap with the first peak of the VASE- and EELS-derived data (in other words, the energy breadth of the first peak of the VASE- and EELS-derived data contains the first two peaks of the DR-derived data). While this could be attributed to a difference in energy resolution, as the energy resolution of the DR data (0.008 eV) was better than both the VASE (0.01 eV) and EELS (0.28 eV) data, it seems unlikely that an energy resolution improvement of 0.002 eV (as compared to VASE) would result in the peak separation of these two features, especially since these two features in the DR-derived data are separated by ~0.3 eV, as this implies that these two features should be resolvable in both the VASE- and EELS-derived absorption coefficient spectra.

It was considered that the lead-free halide double perovskite crystals had oxidized prior to the VASE and EELS measurements, since these samples were exposed to both light and air during sample storage, which may have affected the VASE and low-loss EELS data acquired. However, the EELS data shown thus far were collected from fresh samples that had been stored in a glovebox prior to the EELS measurements. As core-loss EELS (Section 2.2.2) measurements of the oxygen-K edge proved that these samples had not oxidized before the low-loss EELS data was acquired (see Figure 6.9), oxidation of the sample does not explain this difference in the absorption spectra. (This core-loss spectrum was extracted from a core-loss spectrum image that had been collected using

the same collection and convergence angles as the low-loss spectrum image. However, the step size used was 1.2 nm and the exposure time was 50 ms).

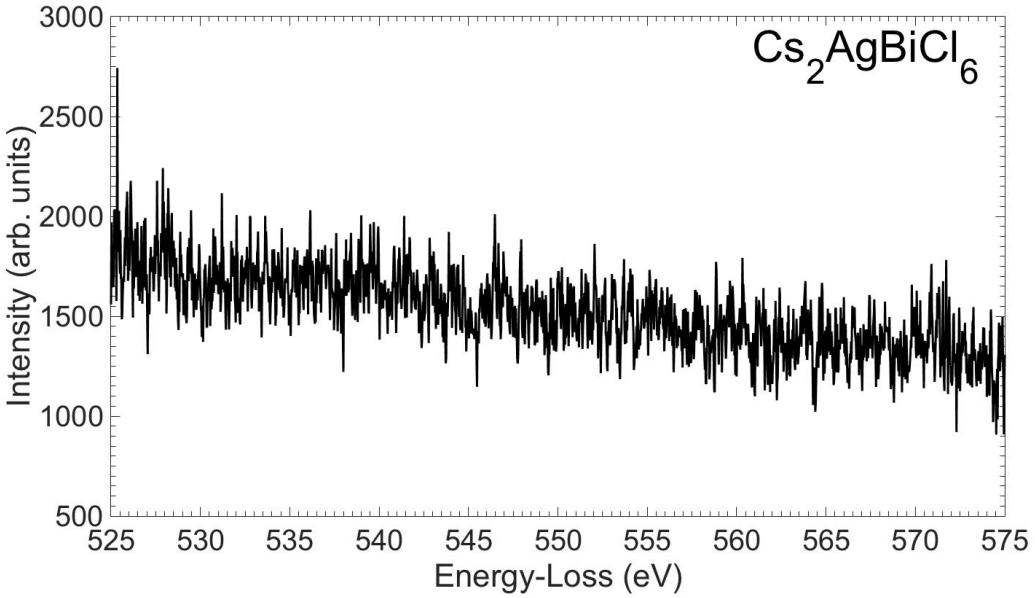

Figure 6.9: Core-loss EELS spectrum acquired for $Cs_2AgBiCl_6$ after the collection of low-loss EELS spectra. Since there is no appreciable intensity at the oxygen-K edge (532 eV [115], this sample has not been oxidized.

Furthermore, a similar discrepancy is observed in the comparisons of the absorption coefficient spectra for $Cs_2AgBiBr_6$ (Figure 6.10b). Ignoring the discrepancies between the VASE- and EELS-derived absorption coefficient spectra for the moment, it is clear that the DR-derived pseudo-absorbance (arbitrary units, scaled by 10,000 to be on same scale) also consists of two peaks that sit beneath the first peak in the VASE-derived data. The models built for the VASE data (Figure 6.1) fit the experimental data well,

suggesting that the extracted *n(E)* and *k(E)* (and therefore α) should be trustworthy, and the Kubelka-Munk calculations were double-checked. Thus, there is no obvious reason why the data obtained via DR and via VASE should differ in this manner.

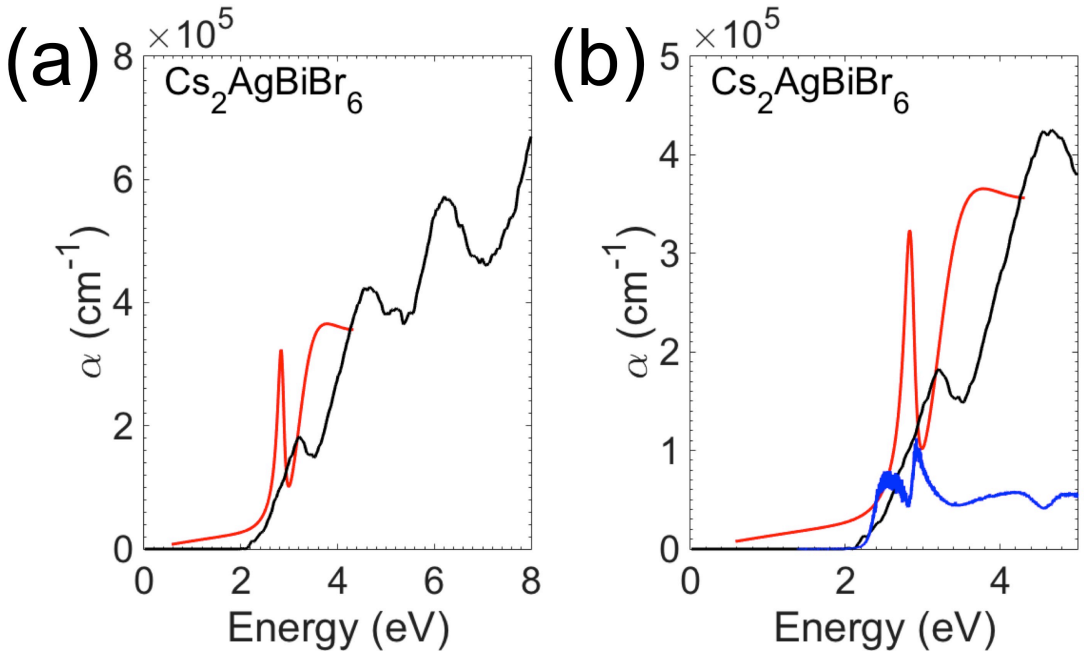

Figure 6.10: (a) Comparison of the absorption coefficient spectra obtained from EELS (black) and VASE (red) for $Cs_2AgBiBr_6$. (b) Comparison of the absorption coefficient spectra obtained from EELS (black) and VASE (red), and the pseudo-absorbance spectrum obtained from diffuse reflectance via the Kubelka-Munk calculations (blue) for $Cs_2AgBiBr_6$. The diffuse reflectance-derived data is from reference [64]. This data was of arbitrary units and was scaled by 10,000 to be on the same scale as the VASE and EELS data.

Unlike the VASE- and EELS-derived absorption coefficient spectra extracted for $Cs_2AgBiCl_6$ (Figure 6.8a), the VASE- and EELS-derived absorption coefficient spectra

extracted for $Cs_2AgBiBr_6$ (Figure 6.10a) do not agree. Although the second peak of the VASE-derived absorption coefficient spectrum seems to correlate to a peak in the EELS-derived absorption coefficient spectrum, the first peak in the VASE-derived data seemingly corresponds to no feature in the EELS-derived absorption coefficient. This may be a consequence of the poor energy resolution of low-loss EELS spectrum used to calculate the absorption coefficient spectrum. As discussed in Section 6.2, the energy resolution of this low-loss spectrum (Figure 6.3) was 0.25 eV.

However, when early low-loss EELS spectrum images were collected of $Cs_2AgBiBr_6$ (α = 9.3 mrad, β = 25.5 mrad, step size = 0.19 nm, exposure time = 20 ms), a low-loss spectrum with an energy resolution of 0.2 eV was extracted from the low-loss EELS spectrum image (Figure 6.11a). (This data was not presented/discussed earlier, as it was collected from a sample that had been left sitting out in air for numerous days before the EELS acquisition. Thus, there were concerns that the sample may have oxidized, which could have affected the EELS data collected, which is why newer measurements were conducted for a sample fresh from the glovebox).

This data was collected prior to concerns about oxidation necessitated new measurements of fresh samples, which is why this data was not the data presented throughout this section). This improvement in energy resolution made it possible to distinctly resolve two peaks at 3-3.5 eV, whereas these two peaks were not as clearly resolved in Figure 6.3. When the absorption coefficient spectrum was extracted for the low-loss spectrum shown in Figure 6.11a, a strong peak in the absorption coefficient spectrum was observed at ~2.7 eV (Figure 6.11b). This feature agrees well in energy with

the first peak of the VASE-derived absorption coefficient. Thus, it seems that this absorption coefficient peak depends strongly on the intensity of the first peak of the doublet at ~3 eV. This analysis highlights the importance of collecting low-loss EELS data with the highest energy resolution achievable. Thus, new low-loss EELS data should be collected with an energy resolution of 0.2 eV or better to ensure that all of the optoelectronic information has been obtained via EELS measurements of this material.

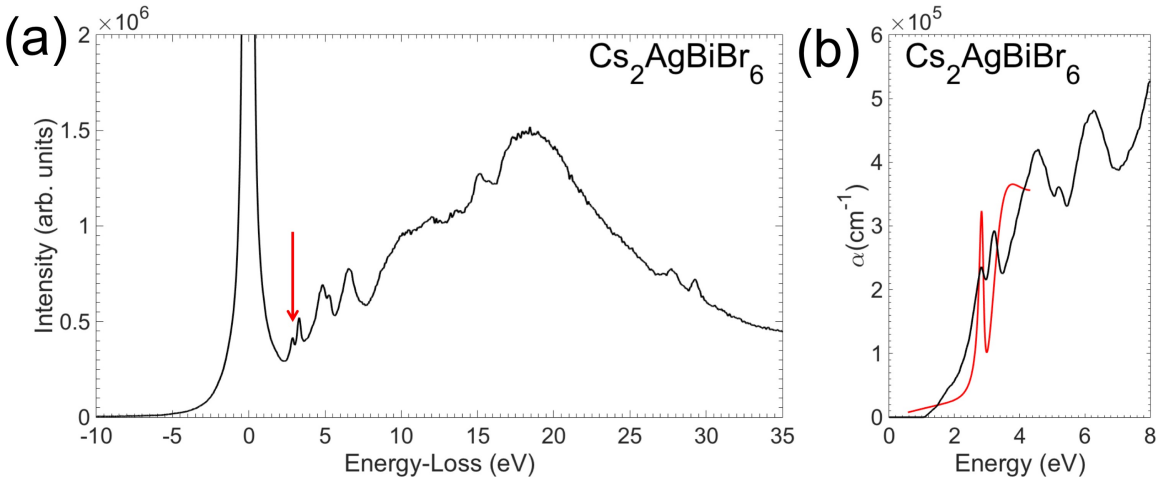

Figure 6.11: (a) Early low-loss EELS spectrum collected for $Cs_2AgBiBr_6$, displaying a distinct peak at ~3 eV (shown by the red arrow). (b) Comparisons of the absorption coefficient spectra collected from VASE (red) and from the EELS data (black) shown in part (a) of this figure. This data was collected with an energy resolution of 0.2 eV, but before special care was taken to reduce the samples' exposure to air prior to the EELS measurements.

6.4. Summary

Low-loss electron energy-loss spectroscopy (EELS) measurements were conducted on two lead-free halide double perovskites - $Cs_2AgBiBr_6$ and $Cs_2AgBiCl_6$ – in order to extract the optoelectronics properties of these materials for energies corresponding to the solar spectrum. Using variable-angle spectroscopic ellipsometry (VASE), approximations of the refractive indices for these materials were obtained. Based on these approximations, low-loss EELS data was collected using a 60 keV electron beam in order to avoid Cherenkov radiation, and this data was processed via Kramers-Kronig analysis to extract the complex dielectric function. By comparing the imaginary part of the complex dielectric function, ε_2, obtained via EELS to that computed using density functional theory (DFT), it was possible to show that most of the features for energies less than 7 eV were observed in the EELS data.

However, discrepancies were observed in the absorption spectra extracted from the VASE data, the EELS data, and previously reported diffuse reflectance (DR) data. For $Cs_2AgBiCl_6$, the VASE-derived and EELS-derived absorption coefficient spectra agreed well. However, for both the $Cs_2AgBiCl_6$ and $Cs_2AgBiBr_6$ data, the DR-derived absorption spectrum differed from the VASE-derived and EELS-derived data, although it is currently not understood why these data sets differed. Until this is resolved, it is not possible to state unequivocally that the optoelectronic properties have been accurately collected via STEM-EELS. Furthermore, comparisons of the EELS-derived $Cs_2AgBiBr_6$ absorption coefficient spectrum with that of the VASE-derived spectrum suggests that low-loss EELS measurements need to be repeated with a higher energy resolution than

0.25 eV. Preferably, these measurements should be collected with an energy resolution better than 0.2 eV.

Chapter 7. Summary, Conclusions, and Future Work

In the following sections, the major results and conclusions from the work presented in Chapters 3 – 6 will be summarized by materials system. Furthermore, suggestions of possible next steps in continuing the study of these materials will be discussed.

7.1. Organic Photovoltaics

The ability to obtain the optoelectronic properties (and therefore, the electronic structure) with high spatial resolution is critical for determining how more efficient organic photovoltaic devices can be engineered. By measuring how these properties vary at the interface between the acceptor and donor materials within the bulk-heterojunction layer of an organic photovoltaic, it should be possible to relate how changes in device processing affect the electronic structure at this interface (and, therefore, exciton dissociation and charge transport). This is especially true for P3HT:PCBM bulk-heterojunction organic photovoltaics for which the morphology has been extensively studied, whereas the electronic structure has not.

Using electron energy-loss spectroscopy (EELS) in a scanning transmission electron microscope (STEM), the optoelectronic properties of materials can be determined with nanometer spatial resolution. Historically, such measurements have not been conducted

for organic photovoltaics due to the difficulty in collecting reliable EELS data for the electron beam-sensitive materials that compose the bulk-heterojunction. In this work, an EELS acquisition method in which the beam-damage can be minimized has been demonstrated, and reliable EELS data was collected for bulk films of P3HT, PCBM, CuPc, and C_{60}. These EELS data sets were analyzed, and the real (ε_1) and imaginary (ε_2) parts of the complex dielectric function were extracted. Furthermore, single electron transitions were identified in the CuPc and C_{60} experimental ε_2 spectra.

As these spectra were collected with minimal observed beam-damage, they can now serve as standard spectra by which future EELS measurements of these materials can be compared. This will be especially useful in the study of P3HT/PCBM interfaces, as it should be possible to observe any changes in the low-loss spectra and the real (ε_1) and imaginary (ε_2) parts of the complex dielectric function that may be attributable to the interaction of these two materials.

Furthermore, it was proven that the improved energy resolution of a Nion UltraSTEM 100 MC 'HERMES' S/TEM (35 meV) did not provide any more electronic information for P3HT, PCBM, CuPc, or C_{60}, as compared to measurements collected on an FEI Titan^3 60-300 Image-Corrected S/TEM with a lower energy resolution (175 meV). Thus, it can be concluded that using an FEI Titan^3 60-300 Image-Corrected S/TEM should be sufficient for obtaining the EELS signal at the interface between P3HT and PCBM domains in a P3HT:PCBM bulk-heterojunction layer.

As the standard EELS spectra were not collected with high spatial resolution, the beam-damage minimization acquisition method was extended for the collection of

spatially-resolved EELS data. By first using a simple CuPc/C_{60} bilayer structure, it was shown that reliable EELS data could be collected for these electron beam-sensitive materials with high spatial resolution. Following this, an actual P3HT:PCBM organic photovoltaic was then studied, for which spatially-resolvable EELS data was acquired. Unfortunately, due to the small sizes of the P3HT and PCBM domains within the bulk-heterojunction layer (~10 nm in diameter), the sample prepared was too thick to distinguish between pure P3HT and pure PCBM domains, and the spectra obtained appeared to be convolutions of the P3HT and PCBM signals (as well as the interfaces between). Thus, it was not possible, on this first attempt, to obtain a low-loss EELS spectrum of only a P3HT and PCBM interface.

Currently, the EELS acquisition methods should be sophisticated enough such that low-loss EELS data can be measured at the interface between the P3HT and PCBM domains of a P3HT:PCBM bulk-heterojunction. However, before these measurements can be realized, it will be necessary to determine a method in which to reliably prepare cross-sectional samples of these devices that are less than ~10 nm in thickness. The development of such a method is non-trivial and may require the combination of multiple approaches (i.e. focused ion beam milling and nano-milling).

Assuming such a method can be developed, low-loss EELS data could be collected at the P3HT/PCBM interface, and the complex dielectric function could be extracted and compared to the standard spectra obtained for pure P3HT and pure PCBM. From these comparisons, it will be possible to determine how the P3HT/PCBM interfacial signal differs (for instance, is the interfacial signal a simple linear combination of the P3HT and

PCBM signals or are there new peaks in the imaginary part of the complex dielectric function that can be attributed to the interface). Such measurements and analysis could then be repeated for multiple P3HT:PCBM bulk-heterojunction organic photovoltaics with varying efficiencies in order to correlate the observed interfacial signals to the performance of the device, and, hopefully, determine what affect the processing steps used in preparing the photovoltaic devices are having on the electronic structure of the P3HT/PCBM interface.

7.2. Vanadium Tetracyanoethylene, $V[TCNE]_{x\sim2}$

Although $V[TCNE]_{x\sim2}$ is an exciting organic-based ferrimagnetic semiconductor that shows promise for various applications, the types of measurements performed on this material have been limited due to its air-sensitivity. For instance, at the writing of this dissertation, there have been no reports of electron energy-loss spectroscopy (EELS) measurements of $V[TCNE]_{x\sim2}$ in the literature, which is likely due to the fact that it is extremely difficult to collect such measurements without exposing the sample to air. This is unfortunate because EELS is an extremely powerful technique that, when combined with the scanning transmission electron microscope (STEM), can probe various material's properties with nanometer spatial resolution.

In this work, a sample preparation technique in which the $V[TCNE]_{x\sim2}$ thin films are minimally exposed to air has been proven to be successful in preparing cross-sections of an Al/$V[TCNE]_{x\sim2}$/Si sample while avoiding oxidation of the $V[TCNE]_{x\sim2}$ films. From

these samples, core-loss EELS data was collected at the V-$L_{2,3}$ edge in order to determine and spatially track the oxidation states of the vanadium ions in V[TCNE]$_{x\sim2}$. Based on the analysis of the peak energy of the V-L_3 peak, an oxidation state close to V^{2+} was obtained, which is consistent with previous measurements in the literature. Furthermore, it was shown that the oxidation states of the vanadium ions are constant throughout the V[TCNE]$_{x\sim2}$ thin film. As all of the previous measurements of the vanadium oxidation state utilized bulk characterization techniques, this is the first time that such consistency in the vanadium oxidation state has been measured.

Through the course of analyzing this core-loss EELS data, a discrepancy in the shape of the V-L_2 peak as compared to previous X-ray absorption near edge structure (XANES) measurements of V[TCNE]$_{x\sim2}$ was observed. It is not immediately clear why the shape of the V-L_2 peak in the EELS data (a single peak) should vary as compared to the shape of the V-L_2 peak in the XANES data (a doublet peak). However, the first step in attempting to answer this question should be to narrow down whether this anomaly is due to the samples of V[TCNE]$_{x\sim2}$ measured or if it is due to differences in the EELS and XANES data collections. This may be possible by measuring the V-$L_{2,3}$ edge of various standard vanadium compounds via EELS. If a doublet peak is observed in the core-loss EELS data of standard vanadium compounds, this would suggest that the variance observed is likely due to differences in the V[TCNE]$_{x\sim2}$ thin films. However, if the doublet peak is not observed, then it may be that there is a fundamental difference in the acquisition of EELS and XANES data that is not immediately obvious.

In addition to measuring the vanadium oxidation state for $V[TCNE]_{x\sim2}$, low-loss EELS measurements were used to extract the real (ε_1) and imaginary (ε_2) parts of the complex dielectric function of the bulk $V[TCNE]_{x\sim2}$ thin film. These measurements were conducted using both a 300 keV and a 60 keV monochromated electron beam. Based on comparisons of the low-loss spectra collected at both 300 keV and 60 keV, combined with the knowledge that the refractive index of $V[TCNE]_{x\sim2}$ is likely in the range of 1.6 to 2.0, the 300 keV data was rejected due to the high probability that Cherenkov losses had been measured. By analyzing the 60 keV data, for which Cherenkov radiation should have been avoided, the complex dielectric function was extracted, and peaks in this imaginary part (ε_2) of the complex dielectric function were correlated to known single electron transitions. Unfortunately, core-loss EELS data collected for the sample used during the acquisition of the 60 keV low-loss data revealed that the sample had oxidized slightly. Thus, until new 60 keV data is collected for a sample in which no oxygen is detected in the $V[TCNE]_{x\sim2}$ thin film, it is impossible to state whether the acquired real (ε_1) and imaginary (ε_2) parts of the complex dielectric function are representative of pure $V[TCNE]_{x\sim2}$ or if they have been altered by this slight oxygen contamination.

Moving forward, the first step in the acquisition of the optoelectronic properties of $V[TCNE]_{x\sim2}$ should be to repeat the 60 keV measurements for a sample that has not oxidized. As discussed in Chapter 5, there is an element of luck in the sample preparation process used to make these measurements, so this may require more than one attempt. However, once data has been collected from such a sample, it will be possible to know for sure what the complex dielectric function should be for $V[TCNE]_{x\sim2}$. Additionally,

from this data, the optoelectronic properties can be tracked throughout the $V[TCNE]_{x\sim2}$ thin film, similar to the analysis used for the tracking of the oxidation state of vanadium. Furthermore, the optoelectronic properties near interfaces, such as the $Al/V[TCNE]_{x\sim2}$, can be extracted in order to determine whether or not there are signs of band bending at this interface.

Once this experiment has been completed, future EELS studies of $V[TCNE]_{x\sim2}$ could focus on studying devices in which $V[TCNE]_{x\sim2}$ is a component (similar to the organic photovoltaic studies discussed in Chapter 4). Additionally, since it has been shown that cross-sectional samples of this air-sensitive material can be prepared for the TEM without oxidizing the $V[TCNE]_{x\sim2}$ thin film, other electron microscopy techniques could be utilized to study this material. For instance, it may be interesting to use Lorentz microscopy to study how the magnetic domain structure in $V[TCNE]_{x\sim2}$ varies on the nanoscale when exposed to a magnetic field [128].

7.3. Lead-Free Halide Double Perovskites

Two lead-free halide double perovskites – $Cs_2AgBiBr_6$ and $Cs_2AgBiCl_6$ – have been proposed as possible replacements for organometal trihalide perovskites typically used in perovskite solar cells. If it is possible to use these lead-free halide double perovskites in perovskite solar cells, toxicological concerns could be alleviated, as this would eliminate the use of lead in such devices. However, while these two lead-free halide double perovskites exhibit promising bandgaps and, in the case of $Cs_2AgBiCl_6$, moisture and

light stability, the optoelectronic properties for energies corresponding to the solar spectrum have not been measured, resulting in a gap in the current knowledge of these materials.

In this work, preliminary electron energy-loss spectroscopy (EELS) measurements were made of both $Cs_2AgBiBr_6$ and $Cs_2AgBiCl_6$. From the acquired low-loss EELS spectra, the complex dielectric function was extracted, and the imaginary parts (ε_2) of the complex dielectric function were then compared to adjusted density functional theory (DFT) calculated ε_2 spectra. These comparisons showed that most of the expected ε_2 features (from DFT) were observed in the experimental ε_2 spectra obtained via EELS. However, in the case of $Cs_2AgBiCl_6$, collecting new low-loss EELS spectra with enhanced energy resolutions (at least less than 0.2 eV) should improve these comparisons, as some of the expected features are not currently resolvable in the EELS data.

Absorption coefficient spectra were also extracted from the experimental EELS data for $Cs_2AgBiBr_6$ and $Cs_2AgBiCl_6$. These spectra were compared to absorption coefficient spectra calculated from VASE experiments and to absorption spectra derived from diffuse reflectance (DR) measurements (found in reference [64]). In both the $Cs_2AgBiBr_6$ and $Cs_2AgBiCl_6$ comparisons of these three data sets, the DR-derived absorption spectra varied greatly from the EELS and VASE absorption coefficient spectra. Currently, there is no obvious explanation for this discrepancy, and, until this inconsistency is resolved, it is impossible to know for certain which spectra are most accurate.

Comparisons of the absorption coefficient spectra extracted from only the VASE and EELS measurements show favorable agreement for $Cs_2AgBiCl_6$. However, analysis of the $Cs_2AgBiBr_6$ absorption coefficient spectra suggests that low-loss EELS measurements need to be repeated with an energy resolution of 0.2 eV or better to ensure that every low-loss feature is resolved.

Moving forward, the first step should be to reacquire low-loss EELS data for both $Cs_2AgBiBr_6$ and $Cs_2AgBiCl_6$ with energy resolutions of 0.2 eV or better. This will ensure that all of the optoelectronic information contained in these samples has been obtained, which should improve the $Cs_2AgBiBr_6$ absorption coefficient spectra comparisons and the $Cs_2AgBiCl_6$ ε_2 comparisons with the DFT calculations. After these measurements have been made, it would also be interesting to measure the optoelectronic properties of these materials after they have been exposed to moisture and light for an extended period of time. Previous reflectance measurements of $Cs_2AgBiBr_6$ have shown that this sample does degrade when exposed to light [64]. If the complex dielectric function were extracted for a degraded $Cs_2AgBiBr_6$ sample, it may be possible to determine which features have changed in the ε_2 spectrum, which could be correlated to changes in the material's electronic structure.

Once a method for preparing thin films of these materials is developed, it would also be interesting to measure the optoelectronic properties of actual perovskite solar cells in which these materials are used.

7.4. Final Remarks

The ability to collect spatially-resolved electron energy-loss spectroscopy (EELS) data for electron beam-sensitive materials has been demonstrated for organic photovoltaics, an organic-based ferrimagnetic semiconductor, and lead-free halide double perovskites. However, these are not the only materials systems in which these techniques can be applied. Moving forward, the methods and analyses described throughout this dissertation can and should be applied to other beam-sensitive functional materials systems in which understanding the electronic structure and/or knowing the optoelectronic properties is critical (for example, wearable electronics, flexible electronics, or organic composite materials).

References

1. Tang CW. Two-layer organic photovoltaic cell. Appl Phys Lett. 1986;48:183–5.

2. Nelson J. Physics of Solar Cells. London: Imperial College Press; 2003.

3. Janssen RAJ, Nelson J. Factors Limiting Device Efficiency in Organic Photovoltaics. Adv Mater. 2013;25:1847–58.

4. Su Y-W, Lan S-C, Wei K-H. Organic photovoltaics. Mater Today. 2012;15:554–62.

5. Helgesen M, Søndergaard R, Krebs FC. Advanced materials and processes for polymer solar cell devices. J Mater Chem. 2010;20:36–60.

6. Cao W, Xue J. Recent progress in organic photovoltaics: device architecture and optical design. Energy Environ Sci. 2014;7:2123.

7. Nelson J. Polymer:fullerene bulk heterojunction solar cells. Mater Today. 2011;14:462–70.

8. Dou L, You J, Hong Z, Xu Z, Li G, Street RA, et al. 25th Anniversary Article: A Decade of Organic/Polymeric Photovoltaic Research. Adv Mater. 2013;25:6642–71.

9. Brabec CJ, Gowrisanker S, Halls JJM, Laird D, Jia S, Williams SP. Polymer-Fullerene Bulk-Heterojunction Solar Cells. Adv Mater. 2010;22:3839–56.

10. Yu G, Gao J, Hummelen JC, Wudl F, Heeger AJ. Polymer photovoltaic cells: Enhanced efficiencies via a network of internal donor-acceptor heterojunctions. Science. 1995;270:1789.

11. Halls JJM, Walsh CA, Greenham NC, Marsegila EA, Friend RH, Moratti SC, et al. Efficient photodiodes from interpenetrating polymer networks. Nature. 1995;376:498–500.

12. Roncali J, Leriche P, Blanchard P. Molecular Materials for Organic Photovoltaics: Small is Beautiful. Adv Mater. 2014;26:3821–38.

13. NREL Research Cell Record Efficiency Chart [Internet]. [cited 2018 Apr 6]. Available from: http://www.nrel.gov/pv/assests/images/efficiency-chart.png

14. Yang X, Loos J, Veenstra SC, Verhees WJH, Wienk MM, Kroon JM, et al. Nanoscale Morphology of High-Performance Polymer Solar Cells. Nano Lett. 2005;5:579–83.

15. Vanlaeke P, Swinnen A, Haeldermans I, Vanhoyland G, Aernouts T, Cheyns D, et al. P3HT/PCBM bulk heterojunction solar cells: Relation between morphology and electro-optical characteristics. Sol Energy Mater Sol Cells. 2006;90:2150–8.

16. Li G, Shrotriya V, Yao Y, Yang Y. Investigation of annealing effects and film thickness dependence of polymer solar cells based on poly(3-hexylthiophene). J Appl Phys. 2005;98:043704.

17. Mihailetchi VD, Xie HX, de Boer B, Koster LJA, Blom PWM. Charge Transport and Photocurrent Generation in Poly(3-hexylthiophene): Methanofullerene Bulk-Heterojunction Solar Cells. Adv Funct Mater. 2006;16:699–708.

18. Berger PR, Kim M. Polymer solar cells: P3HT:PCBM and beyond. J Renew Sustain Energy. 2018;10:013508.

19. Kim Y, Cook S, Tuladhar SM, Choulis SA, Nelson J, Durrant JR, et al. A strong regioregularity effect in self-organizing conjugated polymer films and high-efficiency polythiophene:fullerene solar cells. Nat Mater. 2006;5:197–203.

20. Chuang S-Y, Chen H-L, Lee W-H, Huang Y-C, Su W-F, Jen W-M, et al. Regioregularity effects in the chain orientation and optical anisotropy of composite polymer/fullerene films for high-efficiency, large-area organic solar cells. J Mater Chem. 2009;19:5554.

21. Schilinsky P, Asawapirom U, Scherf U, Biele M, Brabec CJ. Influence of the Molecular Weight of Poly(3-hexylthiophene) on the Performance of Bulk Heterojunction Solar Cells. Chem Mater. 2005;17:2175–80.

22. Li G, Shrotriya V, Yao Y, Huang J, Yang Y. Manipulating regioregular poly(3-hexylthiophene) : [6,6]-phenyl-C61-butyric acid methyl ester blends—route towards high efficiency polymer solar cells. J Mater Chem. 2007;17:3126.

23. Liang Y, Xu Z, Xia J, Tsai S-T, Wu Y, Li G, et al. For the Bright Future-Bulk Heterojunction Polymer Solar Cells with Power Conversion Efficiency of 7.4%. Adv Mater. 2010;22:E135–8.

24. Graham KR, Cabanetos C, Jahnke JP, Idso MN, El Labban A, Ngongang Ndjawa GO, et al. Importance of the Donor:Fullerene Intermolecular Arrangement for High-Efficiency Organic Photovoltaics. J Am Chem Soc. 2014;136:9608–18.

25. Beljonne D, Cornil J, Muccioli L, Zannoni C, Brédas J-L, Castet F. Electronic Processes at Organic−Organic Interfaces: Insight from Modeling and Implications for Opto-electronic Devices †. Chem Mater. 2011;23:591–609.

26. Chen D, Nakahara A, Wei D, Nordlund D, Russell TP. P3HT/PCBM Bulk Heterojunction Organic Photovoltaics: Correlating Efficiency and Morphology. Nano Lett. 2011;11:561–7.

27. Bavel SS van, Sourty E, With G de, Loos J. Three-Dimensional Nanoscale Organization of Bulk Heterojunction Polymer Solar Cells. Nano Lett. 2009;9:507–13.

28. Verploegen E, Mondal R, Bettinger CJ, Sok S, Toney MF, Bao Z. Effects of Thermal Annealing Upon the Morphology of Polymer-Fullerene Blends. Adv Funct Mater. 2010;20:3519–29.

29. Pfannmöller M, Flügge H, Benner G, Wacker I, Sommer C, Hanselmann M, et al. Visualizing a Homogeneous Blend in Bulk Heterojunction Polymer Solar Cells by Analytical Electron Microscopy. Nano Lett. 2011;11:3099–107.

30. Drummy LF, Davis RJ, Moore DL, Durstock M, Vaia RA, Hsu JWP. Molecular-Scale and Nanoscale Morphology of P3HT:PCBM Bulk Heterojunctions: Energy-Filtered TEM and Low-Dose HREM. Chem Mater. 2011;23:907–12.

31. Rujisamphan N, Murray RE, Deng F, Ni C, Shah SI. Study of the Nanoscale Morphology of Polythiophene Fibrils and a Fullerene Derivative. ACS Appl Mater Interfaces. 2014;6:11965–72.

32. Andersson BV, Masich S, Solin N, InganäS O. Morphology of organic electronic materials imaged via electron tomography: MORPHOLOGY OF ORGANIC ELECTRONIC MATERIALS. J Microsc. 2012;247:277–87.

33. van Bavel S, Sourty E, de With G, Frolic K, Loos J. Relation between Photoactive Layer Thickness, 3D Morphology, and Device Performance in P3HT/PCBM Bulk-Heterojunction Solar Cells. Macromolecules. 2009;42:7396–403.

34. van Bavel SS, Bärenklau M, de With G, Hoppe H, Loos J. P3HT/PCBM Bulk Heterojunction Solar Cells: Impact of Blend Composition and 3D Morphology on Device Performance. Adv Funct Mater. 2010;20:1458–63.

35. Sweetnam S, Graham KR, Ngongang Ndjawa GO, Heumüller T, Bartelt JA, Burke TM, et al. Characterization of the Polymer Energy Landscape in Polymer:Fullerene Bulk Heterojunctions with Pure and Mixed Phases. J Am Chem Soc. 2014;136:14078–88.

36. Ro HW, Akgun B, O'Connor BT, Hammond M, Kline RJ, Snyder CR, et al. Poly(3-hexylthiophene) and [6,6]-Phenyl-C $_{61}$ -butyric Acid Methyl Ester Mixing in Organic Solar Cells. Macromolecules. 2012;45:6587–99.

37. Fox M. Optical Properties of Solids. New York, NY: Oxford University Press; 2001.

38. Williams DB, Carter CB. Transmission Electron Microscopy. Second. New York, NY: Springer; 2009.

39. Ng A, Liu X, To CH, Djurišić AB, Zapien JA, Chan WK. Annealing of P3HT:PCBM Blend Film—The Effect on Its Optical Properties. ACS Appl Mater Interfaces. 2013;5:4247–59.

40. Ng AMC, Cheung KY, Fung MK, Djurišić AB, Chan WK. Spectroscopic ellipsometry characterization of polymer–fullerene blend films. Thin Solid Films. 2008;517:1047–52.

41. Ng A, Li CH, Fung MK, Djurišić AB, Zapien JA, Chan WK, et al. Accurate Determination of the Index of Refraction of Polymer Blend Films by Spectroscopic Ellipsometry. J Phys Chem C. 2010;114:15094–101.

42. Morfa AJ, Barnes TM, Ferguson AJ, Levi DH, Rumbles G, Rowlen KL, et al. Optical characterization of pristine poly(3-hexyl thiophene) films. J Polym Sci Part B Polym Phys. 2011;49:186–94.

43. Gevaerts VS, Koster LJA, Wienk MM, Janssen RAJ. Discriminating between Bilayer and Bulk Heterojunction Polymer:Fullerene Solar Cells Using the External Quantum Efficiency. ACS Appl Mater Interfaces. 2011;3:3252–5.

44. Amonoo JA, Glynos E, Chen XC, Green PF. An Alternative Processing Strategy for Organic Photovoltaic Devices Using a Supercritical Fluid. J Phys Chem C. 2012;116:20708–16.

45. Herzing AA, Richter LJ, Anderson IM. 3D Nanoscale Characterization of Thin-Film Organic Photovoltaic Device Structures via Spectroscopic Contrast in the TEM 1. J Phys Chem C. 2010;114:17501–8.

46. Pfannmöller M, Flügge H, Benner G, Wacker I, Kowalsky W, Schröder RR. Visualizing photovoltaic nanostructures with high-resolution analytical electron microscopy reveals material phases in bulk heterojunctions. Synth Met. 2012;161:2526–33.

47. Pokhodnya KI, Epstein AJ, Miller JS. Thin-Film V[TCNE]x Magnets. Adv Mater. 2000;12:410–3.

48. Tengstedt C, de Jong MP, Kanciurzewska A, Carlegrim E, Fahlman M. X-Ray Magnetic Circular Dichroism and Resonant Photomission of V (TCNE) x Hybrid Magnets. Phys Rev Lett [Internet]. 2006 [cited 2018 Apr 26];96. Available from: https://link.aps.org/doi/10.1103/PhysRevLett.96.057209

49. Yu H, Harberts M, Adur R, Lu Y, Hammel PC, Johnston-Halperin E, et al. Ultra-narrow ferromagnetic resonance in organic-based thin films grown via low temperature chemical vapor deposition. Appl Phys Lett. 2014;105:012407.

50. Zhu N, Zhang X, Froning IH, Flatté ME, Johnston-Halperin E, Tang HX. Low loss spin wave resonances in organic-based ferrimagnet vanadium tetracyanoethylene thin films. Appl Phys Lett. 2016;109:082402.

51. Froning IH, Harberts M, Lu Y, Yu H, Epstein AJ, Johnston-Halperin E. Thin-film encapsulation of the air-sensitive organic-based ferrimagnet vanadium tetracyanoethylene. Appl Phys Lett. 2015;106:122403.

52. Pokhodnya K, Bonner M, Prigodin V, Epstein AJ, Miller JS. Carrier transport in the V[TCNE]x (TCNE = tetracyanoethylene; x ~ 2) organic-based magnet. J Phys Condens Matter. 2013;25:196001.

53. Yoo J-W, Edelstein RS, Lincoln DM, Raju NP, Xia C, Pokhodnya KI, et al. Multiple Photonic Responses in Films of Organic-Based Magnetic Semiconductor V (TCNE) x , x ~ 2. Phys Rev Lett [Internet]. 2006 [cited 2018 Apr 26];97. Available from: https://link.aps.org/doi/10.1103/PhysRevLett.97.247205

54. Haskel D, Islam Z, Lang J, Kmety C, Srajer G, Pokhodnya KI, et al. Local structural order in the disordered vanadium tetracyanoethylene room-temperature molecule-based magnet. Phys Rev B [Internet]. 2004 [cited 2018 Apr 26];70. Available from: https://link.aps.org/doi/10.1103/PhysRevB.70.054422

55. Prigodin VN, Raju NP, Pokhodnya KI, Miller JS, Epstein AJ. Spin-Driven Resistance in Organic-Based Magnetic Semiconductor V[TCNE]x. Adv Mater. 2002;14:1230–3.

56. Raju NP, Savrin T, Prigodin VN, Pokhodnya KI, Miller JS, Epstein AJ. Anomalous magnetoresistance in high-temperature organic-based magnetic semiconducting V(TCNE)x films. J Appl Phys. 2003;93:6799–801.

57. Green MA, Ho-Baillie A, Snaith HJ. The emergence of perovskite soalr cells. Nat Photonics. 2014;8:506–14.

58. Zhao Y, Zhu K. Organic-inorganic hybrid lead halide perovskites for optoelectronic and electronic applications. Chem Soc Rev. 2016;45:655–89.

59. Kojima A, Teshima K, Shirai Y, Miyasaka T. Organometal Halide Perovskites as Visible-Light Sensitizers for Photovoltaic Cells. J Am Chem Soc. 2009;131:6050–1.

60. Lee MM, Teuscher J, Miyasaka T, Murakami TN, Snaith HJ. Efficient Hybrid Solar Cells Based on Meso-Superstructured Organometal Halide Perovskites Author(s): Michael M. Lee, Joël Teuscher, Tsutomu Miyasaka, Takurou N. Murakami and Henry J. Snaith. Sci New Ser. 2012;338:643–7.

61. Liu M, Johnston MB, Snaith HJ. Efficient planar heterojunction perovskite solar cells by vapour deposition. Nature. 2013;501:395–8.

62. Park N-G. Perovskite solar cells: an emerging photovoltiac technology. Mater Today. 2015;18:65–72.

63. Hao F, Stoumpos CC, Chang RPH, Kanatzidis MG. Anomalous Band Gap Behavior in Mixed Sn and Pb Perovskites Enables Broadening of Absorption Spectrum in Solar Cells. J Am Chem Soc. 2014;136:8094–9.

64. McClure ET, Ball MR, Windl W, Woodward PM. Cs2AgBiX6 (X = Br, Cl): New Visible Light Absorbing, Lead-Free Halide Perovskite Semiconductors. Chem Mater. 2016;28:1348–54.

65. Pennycook SJ, Nellist PD, editors. Scanning transmission electron microscopy: imaging and analysis. New York, NY: Springer; 2011.

66. Egerton RF. Electron Energy-Loss Spectroscopy in the Electron Microscope. Third. New York, NY: Springer; 2011.

67. Tiemeijer PC. Operation modes of a TEM monochromator. Proc EMAG 99 Sheff. Bristol, UK: Institute of Physics; 1999. p. 191–4.

68. Tiemeijer PC. Measurement of Coulomb interactions in an electron beam monochromator. Ultramicroscopy. 1999;78:53–62.

69. Krivanek OL, Ursin JP, Bacon NJ, Corbin GJ, Dellby N, Hrncirik P, et al. High-energy-resolution monochromator for aberration-corrected scanning transmission electron microscopy/electron energy-loss spectroscopy. Philos Trans R Soc Math Phys Eng Sci. 2009;367:3683–97.

70. Kimoto K. Practical aspects of monochromators developed for transmission electron microscopy. Microscopy. 2014;63:337–44.

71. Krivanek OL, Lovejoy TC, Dellby N, Aoki T, Carpenter RW, Rez P, et al. Vibrational spectroscopy in the electron microscope. Nature. 2014;514:209–12.

72. Krivanek OL, Lovejoy TC, Dellby N, Carpenter RW. Monochromated STEM with a 30 meV-wide, atom-sized electron probe. Microscopy. 2013;62:3–21.

73. Keast VJ. Application of EELS in Materials Science. Mater Charact. 2012;73:1–7.

74. DigitalMicrograph EELS Analysis User's Guide. 2003.

75. Deitz JI, Karki S, Marsillac SX, Grassman TJ, McComb DW. Bandgap profiling in CIGS solar cells via valence electron energy-loss spectroscopy. J Appl Phys. 2018;123:115703.

76. Johnson DW. A Fourier series method for numerical Kramers-Kronig analysis. J Phys Math Gen. 1975;8:490.

77. Brydson R. Electron Energy Loss Spectroscopy. Oxford, UK: BIOS Scientific Publishers Ltd; 2001.

78. Greenaway DL, Harbeke G. Optical Properties and Band Structure of Semiconductors. Oxford, UK: Pergamon Press; 1968.

79. Egerton RF. New techniques in electron energy-loss spectroscopy and energy-filtered imaging. Micron. 2003;34:127–39.

80. Keast VJ, Scott AJ, Brydson R, Williams DB, Bruley J. Electron energy-loss near-edge structure - a tool for the investigation of electronic structure on the nanometre scale. J Microsc. 2001;203:135–75.

81. Tompkins HG. A User's Guide to Ellipsometry. San Diego, CA: Academic Press, Inc.; 1993.

82. Tompkins HG, Irene EA, editors. Handbook of Ellipsometry. Norwich, NY: William Andrew, Inc.; 2005.

83. Tompkins HG, McGahan WA. Spectroscopic Ellipsometry and Reflectometry. New York, NY: John Wiley & Sons, Inc.; 1999.

84. G.E. Jellison, Jr. Data analysis for spectroscopic ellipsometry. Thin Film Solids. 1993;234:416–22.

85. Bu-Abbud GH, Bashara NM, Woollam JA. Variable Wavelength, Variable Angle Ellipsometry Including a Sensitivities Correlation Test. Thin Film Solids. 1986;138:27–41.

86. Alexander JA, Scheltens FJ, Drummy LF, Durstock MF, Gilchrist JB, Heutz S, et al. Measurement of optical properties in organic photovoltaic materials using monochromated electron energy-loss spectroscopy. J Mater Chem A. 2016;4:13636–45.

87. Alexander JA, Scheltens FJ, Drummy LF, Durstock MF, Hage FS, Ramasse QM, et al. High-resolution monochromated electron energy-loss spectroscopy of organic photovoltaic materials. Ultramicroscopy. 2017;180:125–32.

88. Egerton RF. Mechanisms of radiation damage in beam-sensitive specimens, for TEM accelerating voltages between 10 and 300 kV. Microsc Res Tech. 2012;75:1550–6.

89. Egerton RF, Li P, Malac M. Radiation damage in the TEM and SEM. Micron. 2004;35:399–409.

90. Egerton RF. Control of radiation damage in the TEM. Ultramicroscopy. 2013;127:100–8.

91. Egerton RF, Lazar S, Libera M. Delocalized radiation damage in polymers. Micron. 2012;43:2–7.

92. Gilchrist JB, Basey-Fisher TH, Chang SC, Scheltens F, McComb DW, Heutz S. Uncovering Buried Structure and Interfaces in Molecular Photovoltaics. Adv Funct Mater. 2014;24:6473–83.

93. Kroto HW, Allaf AW, Balm SP. C60: Buckminsterfullerene. Chem Rev. 1991;91:1213–35.

94. Richter A, Ries R, Szulzewsky K, Pietzak B, Smith R. The growth mechanisms and morphology of C60 films on different substrates. Surf Sci. 1997;394:201–20.

95. Ichihashi T, Tanigaki K, Ebbesen TW, Kuroshima S, Iijima S. Structures of C60 thin films fabricated on alkali halide substrates by organic MBE. Chem Phys Lett. 1992;190:179–183.

96. Takahashi Y, Hayashi K. Epitaxial Growth of C60/C70 Film on NaCl. J Electron Microsc (Tokyo). 1994;43:378–85.

97. Fryer JR. Electron crystallography of phthalocyanines. J Porphyr Phthalocyanines. 1999;3:672–678.

98. Kovacik P, Sforazzini G, Cook AG, Willis SM, Grant PS, Assender HE, et al. Vacuum-Deposited Planar Heterojunction Polymer Solar Cells. ACS Appl Mater Interfaces. 2011;3:11–5.

99. Wei H, Scudiero L, Eilers H. Infrared and photoelectron spectroscopy study of vapor phase deposited poly (3-hexylthiophene). Appl Surf Sci. 2009;255:8593–7.

100. Farag AAM. Optical absorption studies of copper phthalocyanine thin films. Opt Laser Technol. 2007;39:728–32.

101. Effing J, Jonas U, Jullien L, Plesnivy T, Ringsdorf H, Diederich F, et al. C60 and C70 in a Basket?– Investigations of Mono- and Multilayers from Azacrown Compounds and Fullerenes. Angew Chem Int Ed Engl. 1992;31:1599–602.

102. Barrau S, Heiser T, Richard F, Brochon C, Ngov C, van de Wetering K, et al. Self-Assembling of Novel Fullerene-Grafted Donor–Acceptor Rod−Coil Block Copolymers. Macromolecules. 2008;41:2701–10.

103. Datta D, Tripathi V, Gogoi P, Banerjee S, Kumar S. Ellipsometric studies on thin film CuPC: C60 blends for solar cell applications. Thin Solid Films. 2008;516:7237–40.

104. Capozzi V, Casamassima G, Lorusso GF, Miniafra A, Piccolo R, Trovato T, et al. Optical Spectra and Photoluminescence of C60 Thin Films. Solid State Commun. 1996;98:853–8.

105. Orlandi G, Negri F. Electronic states and transitions in C60 and C70 fullerenes. Photochem Photobiol Sci. 2002;1:289–308.

106. Rosa A, Baerends EJ. Metal-Macrocycle Interaction in Phthalocyanines: Density Functional Calculations of Ground and Excited States. Inorg Chem. 1994;33:584–95.

107. Edwards L, Gouterman M. Porphyrins: XV. Vapor absorption spectra and stability: Phthalocyanines. J Mol Spectrosc. 1970;33:292–310.

108. Saito S, Oshiyama A. Cohesive mechanism and energy bands of solid C 60. Phys Rev Lett. 1991;66:2637.

109. Kelly MK, Etchegoin P, Fuchs D, Kratschmer W, Fostiropoulos K. Optical Transitions of C60 Films in the Visible and Ultraviolet from Spectroscopic Ellipsometry. Phys Rev B. 46:4963–8.

110. Tiemeijer PC, Bischoff M, Freitag B, Kisielowski C. Using a monochromator to improve the resolution in TEM to below 0.5Å. Part I: Creating highly coherent monochromated illumination. Ultramicroscopy. 2012;114:72–81.

111. Krivanek OL, Lovejoy TC, Murfitt MF, Skone G, Batson PE, Dellby N. Towards sub-10 meV energy resolution STEM-EELS. J Phys Conf Ser. 2014;522:012023.

112. Hornback JM. Organic Chemistry. Second. China: Brooks/Cole; 2006.

113. Harberts M, Lu Y, Yu H, Epstein AJ, Johnston-Halperin E. Chemical Vapor Deposition of an Organic Magnet, Vanadium Tetracyanoethylene. J Vis Exp [Internet]. 2015 [cited 2018 Mar 27]; Available from: http://www.jove.com/video/52891/chemical-vapor-deposition-an-organic-magnet-vanadium

114. Bolton JPR, Chen M. Electron energy loss in multilayered slabs. I. Normal incidence. J Phys Condens Matter. 1995;7:3373–87.

115. EELS Atlas - Oxygen [Internet]. EELS.info. [cited 2018 May 31]. Available from: www.eels.info/atlas/oxygen

116. EELS Atlas - Vanadium [Internet]. EELS.info. [cited 2018 May 31]. Available from: www.eels.info/atlas/vanadium

117. Chen JG, Kirn CM, Frühberger B, DeVries BD, Touvelle MS. A NEXAFS determination of the oxidation state of vanadium carbide on V(110): observation of charge transfer from vanadium to carbon. Surf Sci. 1994;321:145–55.

118. Kortright JB, Lincoln DM, Edelstein RS, Epstein AJ. Bonding, Backbonding, and Spin-Polarized Molecular Orbitals: Basis for Magnetism and Semiconducting Transport in V [TCNE] x ~ 2. Phys Rev Lett [Internet]. 2008 [cited 2018 Apr 26];100. Available from: https://link.aps.org/doi/10.1103/PhysRevLett.100.257204

119. Laffont L, Wu MY, Chevallier F, Poizot P, Morcrette M, Tarascon JM. High resolution EELS of Cu–V oxides: Application to batteries materials. Micron. 2006;37:459–64.

120. Mitterbauer C, Kothleitner G, Grogger W, Zandbergen H, Freitag B, Tiemeijer P, et al. Electron energy-loss near-edge structures of 3d transition metal oxides recorded at high-energy resolution. Ultramicroscopy. 2003;96:469–80.

121. Stavitski E, de Groot FMF. The CTM4XAS program for EELS and XAS spectral shape analysis of transition metal L edges. Micron. 2010;41:687–94.

122. de Groot FMF, Fuggle JC, Thole BT, Sawatzky GA. 2p x-ray absorption of 3d transition-metal compounds: An atomic multiplet description including the crystal field. Phys Rev B. 1990;42:5459–68.

123. Baris B, Ozdemir HG, Tugluoglu N, Karadeniz S, Yuksel OF, Kisnisci Z. Optical dispersion and dielectric properties of rubrene organic semiconductor thin film. J Mater Sci Mater Electron. 2014;25:3586–93.

124. Yahia IS, Rammah YS, AlFaify S, Yakuphanoglu F. Optical characterization of nano-pentacene thin films. Supperlattices Microstruct. 2013;64:58–69.

125. Stöger-Pollach M, Franco H, Schattschneider P, Lazar S, Schaffer B, Grogger W, et al. Čerenkov losses: A limit for bandgap determination and Kramers–Kronig analysis. Micron. 2006;37:396–402.

126. Leguy AMA, Azarhoosh P, Alonso MI, Campoy-Quiles M, Weber OJ, Yao J, et al. Experimental and theoretical optical properties of methylammonium lead halide perovskites. Nanoscale. 2016;8:6317–27.

127. EELS Atlas - Bismuth [Internet]. EELS.info. [cited 2018 Jun 6]. Available from: www.eels.info/atlas/bismuth

128. Chapman J., Scheinfein M. Transmission electron microscopies of magnetic microstructures. J Magn Magn Mater. 1999;200:729–40.

Appendix A: Derivation of Equation 21 (Relating ε_1 and ε_2 to α)

Following are the algebraic steps taken to obtain Equation 21:

1. We know that $\varepsilon_1 = n^2 - k^2$ and $\varepsilon_2 = 2nk$.
2. We can rewrite the ε_2 relationship as $k = \varepsilon_2/2n$ and substitute this into the ε_1 relationship to get $\varepsilon_1 = n^2 - (\varepsilon_2/2n)^2 = n^2 - (\varepsilon_2)^2/4n^2$.
3. By multiplying both sides of this equation $4n^2$ to clear the fraction, we get $4n^2\varepsilon_1 = 4n^4 - (\varepsilon_2)^2$, which can be rewritten in the quadratic form as $0 = 4(n^2)^2 - 4\varepsilon_1(n^2) - (\varepsilon_2)^2$.
4. The quadratic equation can now be used to determine the value of n^2. This results in $n^2 = \frac{\varepsilon_1 + \sqrt{(\varepsilon_1)^2 + (\varepsilon_2)^2}}{2}$, where the positive root has been taken as $n > 0$.
5. The absorption coefficient is given by $\alpha = 4\pi k/\lambda$. Since $k = \varepsilon_2/2n$ (see Step 2), then $\alpha = 4\pi\varepsilon_2/2n\lambda$. Plugging in the result from Step 4, we get Equation 21:

$$\alpha = \frac{2\pi\varepsilon_2}{\lambda}\left(\sqrt{\frac{\varepsilon_1 + \sqrt{(\varepsilon_1)^2 + (\varepsilon_2)^2}}{2}}\right)^{-1}$$

Appendix B: 0 to 30 eV Comparisons of EELS and DFT-Adjusted ε_2 Spectra (Lead-Free Halide Double Perovskites)

The following figure compares the imaginary part of the complex dielectric function (ε_2) obtained via EELS to that obtained from the adjusted density functional theory calculations for (a) $Cs_2AgBiBr_6$ and (b) $Cs_2AgBiCl_6$. These comparisons are shown for the entire energy range of the EELS data. Previously, these comparisons were only shown for energies of 0 to 8 eV (Figure 6.7).